

**Advanced CFD model of multiphase photobioreactors for microalgal derived  
biomass production**

by

**Xi Gao**

A dissertation submitted to the graduate faculty  
in partial fulfillment of the requirements for the degree of

DOCTOR OF PHILOSOPHY

Major: Chemical Engineering

Program of Study Committee:  
R. Dennis Vigil, Major Professor  
Rodney O. Fox  
Michael G. Olsen  
Alberto Passalacqua  
Zengyi Shao

Iowa State University

Ames, Iowa

2016

Copyright © Xi Gao, 2016. All rights reserved.

## TABLE OF CONTENTS

LIST OF FIGURES .....	viii
LIST OF TABLES .....	xv
ACKNOWLEDGMENTS .....	xvi
ABSTRACTS .....	xvii
CHAPTER 1. INTRODUCTION .....	1
CHAPTER 2. LITERATURE REVIEW .....	4
2.1. Hydrodynamics and mass transfer simulation of PBRs.....	4
2.1.1. Liquid (and gas) flow simulation.....	5
2.1.2. Algae cell trajectory simulation.....	7
2.1.3. Turbulence simulation .....	8
2.1.4. Mass transfer simulation.....	12
2.2. Light transport simulation.....	13
2.2.1. Beer-Lambert law and its variant.....	14
2.2.2. Two-flux approximation .....	15
2.2.3. Solving radiation transport equation (RTE).....	16
2.2.4. RTE considering bubbles effect.....	18
2.3. PSU-based algae growth rate model .....	19
2.3.1. Eilers-Peeters model .....	22
2.3.2. Han model.....	23
2.3.3. Nikolaou et al. model.....	24
2.3.4. Camacho Rubio et al. model.....	25

2.3.5. Bernardi et al. model.....	26
2.3.6. Garcia-Camacho et al. model.....	27
2.3.7. Papadakis et al. model.....	28
2.4. Comprehensive coupling and simulation.....	29
2.4.1. Circulation time approach.....	30
2.4.2. Lagrangian approach.....	30
2.4.3. Compartment approach.....	31
2.4.4. Eulerian approach.....	32
2.5. Summary.....	35
<b>CHAPTER 3. CFD INVESTIGATION OF BUBBLE EFFECTS ON</b>	
<b>TAYLOR-COUPETTE FLOW PATTERNS IN THE WEAKLY TURBULENT</b>	
<b>REGIME.....</b>	<b>38</b>
3.1. Introduction.....	39
3.2. Two-fluid model for Taylor-Couette flow.....	45
3.2.1. Governing equation and interphase forces.....	45
3.2.2. Turbulence modeling.....	47
3.2.3. Simulation conditions and strategy.....	48
3.3. Results and discussion.....	50
3.3.1. Bubble distribution patterns and mechanism.....	50
3.3.2. Transition of Taylor vortex structure.....	56
3.3.3. Liquid hydrodynamics.....	59
3.4. Conclusion.....	61

CHAPTER 4. AN ADAPTIVE MODEL FOR GAS-LIQUID MASS TRANSFER IN A MULTIPHASE TAYLOR-COUETTE REACTOR .....	63
4.1. Introduction.....	64
4.2. Model equations.....	69
4.2.1. CFD model for bubbly Taylor–Couette flow.....	69
4.2.2. Turbulence modeling .....	73
4.2.3. Mass transfer models .....	74
4.3. Simulation approach and computational details .....	77
4.3.1. Overview of computational approach.....	77
4.3.2. Computational domain and boundary conditions .....	78
4.4. Results and discussion .....	81
4.4.1. Selection of mass transfer model parameters.....	81
4.4.2. Validation of adaptive mass transfer model.....	82
4.4.3. Factors influencing mass transfer rate .....	87
4.4.4. Mass transfer coefficients and interfacial area.....	93
4.5. Conclusions.....	97
CHAPTER 5. CHARACTERISTIC TIME SCALES OF MIXING, MASS TRANSFER AND BIOMASS GROWTH IN A TAYLOR VORTEX ALGAL PHOTOBIOREACTOR .....	100
5.1. Introduction.....	101
5.2. Method .....	103
5.2.1. Organism, media, and subculture.....	103
5.2.2. Photobioreactor .....	104

5.2.3. Experimental measurements .....	106
5.3. Calculation of characteristic time scales .....	107
5.3.1. Rate controlling step .....	107
5.3.2. Characteristic mixing time .....	108
5.3.3. Characteristic gas–liquid mass transfer time .....	109
5.3.4. Characteristic biomass growth time .....	112
5.4. Results and discussion .....	113
5.4.1. Mixing time.....	113
5.4.2. Interphase mass transfer time.....	114
5.4.3. Biomass growth experiments .....	117
5.4.4. Comparison of characteristic time scales.....	121
5.5. Conclusion .....	123
 CHAPTER 6. COMPREHENSIVE COMPUTATIONAL MODEL FOR COMBINING FLUID HYDRODYNAMICS, LIGHT TRANSPORT AND BIOMASS GROWTH IN A TAYLOR VORTEX ALGAL PHOTOBIOREACTOR: LAGRANGIAN APPROACH .....	
6.1. Introduction.....	125
6.2. Comprehensive Reactor Model.....	127
6.2.1. Gas-Liquid Two-Phase Flow CFD Model.....	127
6.2.2. Lagrangian Particle Tracking Simulations.....	128
6.2.3. Algal Biomass Growth Model .....	130
6.2.4. Radiative Transport Simulation .....	131
6.2.5. Model Component Coupling Method .....	132

6.3. Computational Details.....	133
6.3.1. Growth rate model parameters.....	133
6.3.2 Algebraic Representation of Light Distribution .....	134
6.3.3. Taylor Vortex Photobioreactor .....	134
6.4. Results and Discussion.....	137
6.4.1. Flow Hydrodynamics.....	137
6.4.2. Particle Trajectory and Light Exposure History .....	138
6.4.3. Biomass Growth Curves .....	140
6.5. Summary and Conclusions.....	145
 CHAPTER 7. COMPREHENSIVE COMPUTATIONAL MODEL FOR COMBINING FLUID HYDRODYNAMICS, LIGHT TRANSPORT AND BIOMASS GROWTH IN A TAYLOR VORTEX ALGAL PHOTOBIOREACTOR: EULERIAN APPROACH .....	
APPROACH .....	147
7.1. Introduction.....	148
7.2. Model Equations and Methods .....	150
7.2.1. Three-phase Fluid Flow Model.....	150
7.2.2. Algal Biomass Growth Model .....	152
7.2.3. Radiation Transport Model.....	154
7.2.4. Coupling of Model Components.....	155
7.2.5. Computational Details .....	156
7.3. Results and Discussion.....	157
7.3.1 Flow Hydrodynamics.....	157
7.3.2. Light Distribution.....	159

7.3.3 Biomass Growth Curves .....	160
7.3.4 Comparison of Eulerian and Lagrangian Simulations .....	162
7.4. Conclusion .....	165
CHAPTER 8. SUMMARY AND FUTURE WORK .....	167
8.1. Summary .....	167
8.2. Opportunities.....	169
NOTATION .....	172
REFERENCES .....	174

## LIST OF FIGURES

Figure 1.1	The interplay between fluid mechanics, radiation, and algae growth kinetics. ....	2
Figure 2.1	(a) Scheme of Eilers-Peeters model. $x_1$ , $x_2$ and $x_3$ represent the fractions of PSUs in resting, active and inhibited states, respectively. (b) Scheme of Han model. (c) Scheme of Camacho Rubio et al. model. $a_1$ , $a_2$ and $a_3$ represent the numbers of PSUs in resting, active and inhibited states, respectively. (d) Scheme of Garcia Camacho et al. model. (e) Scheme of Papadakis et al. model. When the excitation energy is allocated to the linear electron flow, the PSU in active state is denoted as $x_2^L$ , and when it is allocated to the cyclic electron flow, the PSU in active state is denoted as $x_2^C$ . ....	21
Figure 2.2	The schematic diagram of multi-timescale coupling method for (a) Lagrangian approach and (b) Eulerian approach.....	35
Figure 3.1	General schematic view of the Taylor–Couette flow system. ....	40
Figure 3.2	Computed bubble phase volume fraction contour plot in the annulus. The inner cylinder wall is shown on the bottom. The gas entrance is on the left side of the plot adjacent to the inner cylinder wall and the gas exits on the right side of the plot.....	51
Figure 3.3	Computed bubble volume fraction contour plot on the inner wall by 3D. ....	52
Figure 3.4	Comparison between numerical and experimental data of radial gas concentration profiles at different Reynolds number.....	53
Figure 3.5	Simulated radial gas concentration at different gas flow rate. ....	54

Figure 3.6	Radial profiles of interphase forces acting on the bubble phase at different Reynolds numbers. ....	55
Figure 3.7	Stream function of the liquid phase in single-phase cases and effect of Reynolds number on the wavelength of Taylor vortices (kg/s). ....	56
Figure 3.8	Stream function of the liquid phase in two-phase cases and effect of Reynolds number on the wavelength of Taylor vortices (kg/s). ....	57
Figure 3.9	Stream function of the liquid phase in two-phase cases and effect of bubble...	58
Figure 3.10	Flow regime map for bubble–liquid two phase Taylor–Couette flow. ....	58
Figure 3.11	Comparison between simulated axial, radial and azimuthal liquid velocity in the annulus. The inner cylinder wall is shown on the bottom. The gas entrance is on the left side of the plot adjacent to the inner cylinder wall and the gas exits on the right side of the plot. ( $Q_g = 0.33$ ml/s, $Re = 2900$ ). ...	60
Figure 3.12	Simulated three components of the liquid velocity (a) and simulated three components of the normal Reynolds stress tensor for both single-phase case and two-phase case (b). ....	61
Figure 4.1	Illustration of the relationships between volumetric mass transfer coefficient and various geometric, operational, and hydrodynamic parameters. ....	65
Figure 4.2	Configuration of a Taylor vortex reactor. ....	67
Figure 4.3	Schematic of Taylor–Couette bioreactor used for mass transfer experiments. ...	80
Figure 4.4	Axially averaged radial distributions of (a) volumetric mass transfer coefficient (1/s), (b) gas volume fraction, (c) slip velocity (m/s), and (d)	

	turbulence dissipation rate ( $\text{m}^2/\text{s}^3$ ) for rotation speed and gas flow rate of 300 rpm and 0.235 vvm, respectively.....	82
Figure 4.5	Comparison of predicted average volumetric mass transfer rate by different mass transfer models with experimental data under different rotational speeds.....	84
Figure 4.6	Comparison of predicted average volumetric mass transfer rate by different mass transfer models with experimental data under different inlet gas flow rates.....	85
Figure 4.7	Comparison of simulated instantaneous liquid phase oxygen concentration with experimental data of a specific case (0.235 vvm, 300 rpm) at an axial location of 12.7 cm from the bottom of the reactor and near the outer cylinder wall.....	86
Figure 4.8	Global slip velocity as a function of inlet gas flow rate and cylinder rotation speed.....	89
Figure 4.9	Global turbulent dissipation rate as a function of inlet gas flow rate and cylinder rotation speed.....	90
Figure 4.10	Comparison of simulated volume averaged gas holdup with experimental data for the case of no cylinder rotation.....	91
Figure 4.11	Predicted global volume averaged gas fraction as a function of inlet gas flow rate and rotational speed.....	93
Figure 4.12	Contour plots of (a) mass transfer coefficient $k_L$ (m/s) predicted by the adaptive mode and (b) specific interfacial area $a$ ( $\text{m}^2/\text{m}^3$ ) for a gas flow rate of 0.235 vvm and cylinder rotation speed of 300 rpm. In each plot,	

	the inner cylinder wall is represented by the bottom boundary and the outer cylinder wall is represented by the top boundary. ....	94
Figure 4.13	Predicted average mass transfer coefficients by the adaptive mass transfer model under different rotational speeds and inlet gas flow rates.....	95
Figure 4.14	Predicted specific interfacial area as a function of cylinder gas flow rate and cylinder rotation speed. ....	96
Figure 5.1	Schematic diagram of the batch culture and data acquisition system. ....	105
Figure 5.2	Mixing time, $t_{\text{mix}}$ , as functions of (a) cylinder rotation speed and (b) gas flow rate. The same trends are observed independent of the choice of constant gas volumetric flow rate in (a) or constant cylinder speed in (b). ....	114
Figure 5.3	CO <sub>2</sub> volumetric mass transfer coefficient, $k_L a$ , as functions of (a) cylinder rotation speed and (b) gas flow rate. The same trends are observed independent of the choice of constant gas volumetric flow rate in (a) or constant cylinder speed in (b). ....	115
Figure 5.4	Experimental measurement of dissolved oxygen concentration in the Taylor vortex reactor as a percentage of water saturated with air at 20 °C. Inner cylinder rotation speed in both experiments was 400 rpm. ....	117
Figure 5.5	Dry biomass growth curves and yield plots showing the effect of gas composition (plots (a and b)), cylinder rotation speed (plots (c and d)), and gas flow rate (plots (e and f)). ....	118
Figure 5.6	Characteristic time scales for mixing ( $t_{\text{mix}}$ ), mass transfer ( $t_{\text{MT}}$ ), and biomass growth ( $t_g$ ) plotted as a function of time for two typical <i>C.</i> <i>vulgaris</i> growth experiments. Two curves are shown for $t_g$ ,	

	corresponding to calculations using Eqs. (5.13) and (5.18), respectively. ....	122
Figure 6.1	Coupling of fluid dynamics, radiation transport and algal growth kinetics. ...	125
Figure 6.2	(a) Structure of the three state PSU model first proposed by Eilers and Peeters (1993). (b) Comparison of fitted specific growth rate with experimental data of Dauta et al. (1990).....	131
Figure 6.3	Schematic diagram of multi-timescale coupling method for Lagrangian simulation approach. ....	133
Figure 6. S1	(a) Taylor vortex bioreactor used for biomass cultivation. (b) Cross-section of the Taylor vortex bioreactor.....	135
Figure 6.4	Contour plot of (a) stream function of the liquid phase (kg/s) and (b) bubble volume fraction distribution at rotational speed of 400 rpm. In each plot, the inner cylinder wall is represented by the bottom boundary and the outer cylinder wall is represented by the top boundary. In order to better show the results, the reactor length was scaled to half of the original length. ....	137
Figure 6.5	(a)-(c): Example radial position tracks for an algal cell at various reactor rotational speeds. (d)-(f): Light/dark cycle frequency at various reactor rotational speeds and for the specific condition when the light/dark boundary is located at normalized radial position $(r - r_i) / (r_o - r_i) = 0.5$ .....	139
Figure 6.6	Light history of a typical algal cell at various biomass concentrations and for a fixed reactor rotational speed of 400 rpm. (a) 0.25g/L (b) 1 g/L (d) 4 g/L. ....	140
Figure 6.7	Comparison of simulated biomass growth curves (lines) with experimental	

	data (symbols) for different reactor inner cylinder rotational speeds. ....	141
Figure 6.8	Fraction of photosynthetic units in the (a) resting, (b) active, and (c) inhibited states as a function of time. The radial position of the light/dark boundary, based upon the photocompensation point, is shown in (d) as a function of time. ....	144
Figure 6.S2	Algal cell radial distribution function (based upon 1000 particle tracks) in the annular chamber at different inner cylinder rotation speeds. ....	145
Figure 7.1	Eulerian approach for coupling hydrodynamics, radiation transport, and algal growth kinetics. ....	156
Figure 7.2	Contour plots of (a) bubble volume fraction and (b) solid volume fraction. Panel (c) depicts a solid phase (algal cells) velocity vector plot for an inner cylinder rotation speed of 400 rpm. The inner and outer cylinder walls are represented by the bottom and top boundaries, respectively. ....	159
Figure 7.3	Photon flux as a function of normalized radial position and for various biomass loadings, as obtained using the method of Kong and Vigil (2014) for solving the general radiative transport equation for <i>C. vulgaris</i> in a Taylor vortex reactor. ....	160
Figure 7.4	(a) Comparison of algal growth curve predictions with experiments in a Taylor vortex reactor for various mixing conditions and using the Eulerian modeling approach. (b) Comparison of algal growth curve predictions with experiments in a Taylor vortex reactor for various mixing conditions using the Lagrangian modeling approach. ....	162
Figure 7.5.	Fraction of photosynthetic units in the (a) resting, (b) active, and	

(c) inhibited states as a function of time. The radial position of the light/dark boundary, based upon the photocompensation point, is shown in (d)..... 163

## LIST OF TABLES

Table 2.1	List of CFD simulations of flow hydrodynamics in photobioreactors in the last decade.....	9
Table 2.2	Comprehensive coupling and simulation of PBRs. ....	33
Table 3.1	Summary of experimental and numerical work on bubbly Taylor-Couette flow in recent years. ....	42
Table 3.2	Experimental conditions of Murai et al's experiment (at 298k) .....	49
Table 4.1	Constitutive relations for bubbly Taylor-Couette two-fluid model .....	71
Table 4.2	Constants in bubbly Taylor-Couette two-fluid model (Gao et al., 2015a; 2015b).....	71
Table 7.1	Liquid and solid model parameters and constants (Gao et al., 2015a; 2015c).....	152

## ACKNOWLEDGMENTS

First, I would like to express the deepest appreciation to my advisor Professor R. Dennis Vigil. Without his patience, expertise, guidance and support, this dissertation is impossible. It was a great pleasure working with him.

I am highly grateful to my committee members, Dr. Rodney O. Fox, Dr. Michael G. Olsen, Dr. Alberto Passalacqua, Dr. Zengyi Shao, for their helpful discussion and suggestion on the research.

I want to thank my group members and colleagues for their help in research: Dr. Bo Kong, Dr. Mahdi Ramezani, Dr. Xiaofei Hu and Zhengping Liu.

Finally, I also would like to express my gratitude to my family and friends for their love and support.

## ABSTRACTS

Development of more efficient algal photobioreactors (PBRs) is driven by increasing interest in algaculture for the production of fuels, chemicals, food, animal feed, and medicine, as well as carbon capture. While at present, the cost and microalgae production capacity are one of its restrictions when competition with other biodiesel feedstock. The objective of the present work is to develop and validate better computational models to investigate the interplay between fluid hydrodynamics, radiation transport and algae growth, which is crucial to determine the performance and scalability of algae photobioreactors.

First, a detailed review of the pertinent information required for developing a comprehensive computation model for photobioreactors was conducted. The current status of the submodels, including hydrodynamics and mass transfer multiphase CFD models, radiation transport models, microalgae growth rate models, and coupling method for developing a comprehensive model for PBRs was outlined.

Second, an Eulerian two-fluid model for gas-liquid Taylor-Couette flow was proposed and validated. The CFD was based on the RANS approach with constitutive closures for interphase forces and liquid turbulence. The model was validated by comparison with previously published experimental data. The mechanism of bubble radial non-uniformity distribution was discussed and the relative importance of various interphase forces was demonstrated.

Third, the validated two fluid CFD model was employed to simulate the local values of the mass transfer coefficient based on the Higbie theory. A novel approach was proposed to

estimate the mass transfer exposure time. This approach automatically selects the appropriate expression (either the penetration model or eddy cell model) based on local flow conditions. The simulation predictions agree well with experimental findings, which demonstrates that the adaptive mass transfer model has the ability to correctly description of both local and global mass transfer of oxygen in a semi-batch gas–liquid Taylor–Couette reactor.

Forth, microalgae culture experiment was conducted to identify the limiting factor in the Taylor-Couette photobioreactor. The characteristic time scales for mixing, mass transfer and biomass growth was compared. It is found that algal growth rate in Taylor vortex reactors is not limited by fluid mixing or interphase mass transfer, and therefore the observed biomass productivity improvements are likely attributable to improved light utilization efficiency (high-frequency light/dark cycles).

Fifth, a commonly used Lagrangian strategy for coupling the various factors influencing algal growth was employed whereby results from computational fluid dynamics and radiation transport simulations were used to compute numerous microorganism light exposure histories, and this information, in turn, was used to estimate the global biomass specific growth rate. The simulation predictions were compared with experimental measurements and the origin of weaknesses of the commonly used Lagrangian approach model was traced.

Sixth, an alternative Eulerian computational approach for predicting photobioreactor performance was proposed, wherein a transport equation for algal growth kinetics is solved, thereby obviating the need to carry out thousands of particle tracking simulations. The simulation predictions were compared with experimental measurements and commonly used Lagrangian approach model.

## CHAPTER 1. INTRODUCTION

Large-scale production of phototrophic microalgae has mainly been driven by the great potential for many industrial applications, such as biofuels, biochemicals, human and animal nutritions, cosmetics, medicine and high-value molecules, as well as carbon capture and wastewater treatment (Wijffels and Barbosa, 2010; Jansen 2016). Laboratory cultivation of microalgae has a history of more than a half decade, however at present large-scale cultivation outdoor was still hampered by high production cost and low production yield. This is because the hydrodynamics, mass transfer, light availability in large-scale photobioreactor is dramatically different with that in the lab-scale reactor, also the microalgae cells are exposure to unsteady environmental conditions outdoor, such as diurnal light and temperature variations.

Mathematical modeling can be used to understand the complex phenomena inside the photobioreactor, which can be a great help to overcome the limitations related to design and scale up of photobioreactors. Comprehensive modeling of photobioreactor is more challenging than conventional reactors due multi-time and multi-scale coupling between physical, chemical and biological phenomenon. The interactions between fluid dynamics, nutrient concentration, light distribution, algae growth rate and biomass distribution in photobioreactors is depicted in Figure 1.1. It can be seen the comprehensive modeling requires at least four submodels, the multiphase CFD model, species transport model, radiation transport model and biomass growth model, as well as the coupling method between these models. However, quantitatively accurate and computational effective models as well

as coupling method are insufficient. For example, a validated multiphase model that can accurately capture the mixing and mass transfer phenomenon in photobioreactors is still lacking due to the intrinsic complexity of flow phenomena in multiphase systems. It is an urgent need to develop advanced multiphase turbulence models and validate reliable interphase force models for drag, lift, virtual mass, turbulent dissipation and so on (Buffo and Marchisio, 2014). For radiation transport simulation in photobioreactor, the commonly used empirical Beer-Lambert law only applies to specific geometry and simple illumination method, while for realistic complex geometries involving curved reactor walls and complex immunization method, a radiative transfer model which can describe the absorbing, emitting, and scattering of medium, algae cells and bubbles is still lacking (Kong and Vigil, 2014). For microalgae growth rates simulation, a mechanistic model that can consider photosynthesis, photoinhibition, and photoacclimation under rapidly changing in incident radiation are also remain to be developed. Besides of challenges for developing accurate models for hydrodynamics, mass transfer, radiation transport and biomass growth rate, a comprehensive coupling method, which can deal with multidisciplinary and multiscale interactions is required.

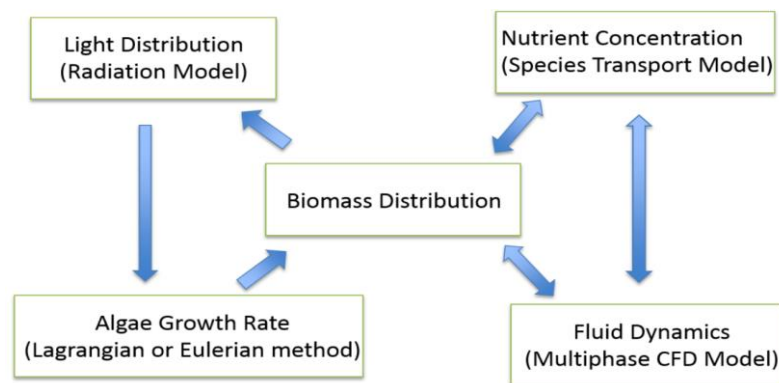


Figure 1.1. The interplay between fluid mechanics, radiation, and algae growth kinetics.

The objective of the present work is to develop and validate better computational models to investigate the interplay between fluid hydrodynamics, radiation transport and algae growth, which is crucial to determine the performance and scalability of algae photobioreactors.

It becomes clear that it is necessary to deal with the following aspects to provide useful guidance for algae photobioreactors design and scale up. First, a multiphase computational hydrodynamics model that can correctly predict the flow hydrodynamics. Second, a mass transfer model that can accurately simulate the species transport and mass transfer between gas and liquid species. Third, a dynamics algal growth rate model can predict the light history and growth rate of microorganisms considering the effect of hydrodynamics (Lagrange particle tracking model or Eulerian approach). Fourth, a comprehensible model coupling the above three aspects.

## CHAPTER 2. LITERATURE REVIEW

Large-scale production of phototrophic microalgae has led to increasing commercial interest in their great potential for many industrial application, such as biofuels, biochemicals, human and animal nutritions, cosmetics, medicine and high value molecules, as well as carbon capture and wastewater treatment. Mathematical modelling is becoming more important to understand the complex phenomena inside photobioreactors and to overcome the limitations related to design and scale up of photobioreactors. This review outlines the current status of the submodels, including hydrodynamics and mass transfer multiphase CFD models, radiation transport models, microalgae growth rate models, and coupling method for developing a comprehensive model for PBRs. In review of the merits and limitations of submodels and coupling method, a more reliable and computational efficient comprehensive model is needed.

### **2.1. Hydrodynamics and mass transfer simulation of PBRs**

Flow hydrodynamics in PBRs has a large effect on the microalgae growth. Good mixing can avoid nutrient and temperature gradients, increase gas-liquid mass transfer and decrease cells self-shading phenomenon. While high shear stress rate can damage algae cells. With the significant improvement of computational speed in recent years, CFD has been widely used for photobioreactor design and scale up. In terms of review multiphase CFD models, the review will summary the applications of CFD in simulation of mixing and mass transfer in PBRs in the last decade. It can be seen from Table 2.1 that CFD simulations have been

applied to many kinds of photobioreactors, such as raceway reactor (Xu et al., 2014; Hreiz et al., 2014; Prussi et al., 2014; Park and Li, 2015; Zhang et al., 2015; Huang et al., 2015; Zeng et al., 2016), flat plate (Shu et al., 2010; Zhang et al., 2012; Wang et al., 2014; Huang et al., 2014; 2015; Chen et al., 2016), airlift (Luo and Al-Dahhan, 2011; Li et al., 2012; Massart et al., 2014; Soman and Shastri, 2015), bubble column (Mortuza et al., 2012; Seo et al., 2012; Nauha and Alopaeus, 2013; 2015; Gerdes et al., 2014; Gerdes et al., 2014; Bitog et al., 2014; Bari et al., 2014; 2015), tubular (Moberg et al., 2012; Zhang et al., 2013; Gómez-Pérez, 2015; Cheng et al., 2016), stirred tank (Zhang, 2013; Delafosse et al., 2014; Delafosse et al., 2015; Krujatz et al., 2015), torus (Pruvost et al. 2006; 2008), virtual (Sato et al., 2010), Taylor-Couette (Gao et al., 2015a; 2015b; 2016a) and so on. CFD simulation was mainly used to design and optimize novel reactors or internals by studying the flow hydrodynamics, mass transfer and algae cell trajectory.

### **2.1.1. Liquid (and gas) flow simulation**

CFD simulations can provide the details of fluid hydrodynamics that is difficult to obtain from experiments and can also be used to minimize cost. It can be seen from Table 2.1, CFD has been used to study operating and geometry factors in PBRs that influence the flow dynamics, such as the inlet gas flow rate, bubble diameter, gas holdup, liquid properties, reactor geometry and size, internals type and movement. For liquid- gas two phases hydrodynamics simulation in PBRs, the Volume of Fluid (VOF), Eulerian-Lagrangian and Eulerian-Eulerian, were popularly used. VOF method models two immiscible fluids by solving a single set of momentum equations and tracking the volume fraction of the each of

the fluids through the domain. It has been applied to simulate the raceway ponds (Xu et al., 2014; Hreiz et al., 2014; Prussi et al., 2014). In the Eulerian-Lagrangian approach, the liquid phase is treated as a continuum by solving the Navier-Stokes equations, while the gas phase is solved by tracking a large number of bubbles. The gas phase can exchange mass, momentum and energy with the liquid phase. This approach has been used to study the liquid-gas flow by several researchers (Sato et al., 2010; Mortuza et al., 2012; Seo e al., 2012; Moberg et al., 2012; Bari et al., 2014; Bitog et al., 2014; Gerdes et al., 2014; Massart et al., 2014; Bari et al., 2015). In the Eulerian-Eulerian approach, both phases are treated as interpenetrating continuum and continuum equations are solved for both phases with an appropriate interaction. This approach is most widely used which can be seen from Table 2.1 as it requires less computational resources. The mass, momentum, and species transport equations of the general E-E model for simulating liquid-gas flow in photobioreactor can be expressed as follows,

$$\frac{\partial}{\partial t}(\alpha_k \rho_k) + \nabla \cdot (\alpha_k \rho_k \vec{u}_k) = S_{pk} \quad (2.1)$$

$$\frac{\partial}{\partial t}(\alpha_k \rho_k \vec{u}_k) + \nabla \cdot (\alpha_k \rho_k \vec{u}_k \vec{u}_k) = -\alpha_k \nabla p + \nabla \cdot (\overline{\overline{\tau}_k} + \overline{\overline{\tau}_k^{Re}}) + S_{pk} \vec{u}_{pk} + \alpha_k \rho_k \vec{g} + \vec{F}_{lk} \quad (2.2)$$

$$\frac{\partial}{\partial t}(\alpha_k \rho_k Y_k^i) + \nabla \cdot (\alpha_k \rho_k \vec{u}_k Y_k^i) = -\nabla \cdot \alpha \vec{J}_k^i + S_{pk}^i \quad (2.3)$$

Here,  $\alpha_k$  and  $\vec{u}_k$  are the phase volume fraction and the phase velocity, respectively.  $Y_k^i$  is the mass fraction of species  $i$  in phase  $k$ .  $S_{pk}$  is the rate of mass transfer from phase  $p$  to phase  $k$ . The phase stress and Reynolds stress tensors are represented by  $\overline{\overline{\tau}_k}$  and  $\overline{\overline{\tau}_k^{Re}}$ , respectively.  $\vec{J}_k^i$  and  $S_{pk}^i$  represent the diffusive flux and the net rate of appearance of species

$i$  due to interphase mass transfer.  $\vec{F}_k$  is the interphase momentum exchange term, which can be decomposed into at least five independent interphase forces,

$$\vec{F}_{ik} = \vec{F}_D + \vec{F}_L + \vec{F}_{VM} + \vec{F}_W + \vec{F}_T \quad (2.4)$$

These interphase forces represent drag, lift, virtual mass, wall lubrication, and turbulent dispersion, respectively. The development and validation of interphases forces is a hot topic in multiphase simulation, interested readers can refer to good reviews (Zhang et al., 2006; Tibit et al., 2008).

### 2.1.2. Algae cell trajectory simulation

The cell trajectory determines the light availability of algae cell, which plays a crucial role in determining the performance of algal photobioreactors. The Lagrangian particle tracking model coupled with the liquid (and gas) CFD model has been employed to describe the algae motion by integrating the force balance on it in photobioreactors (Shu et al., 2010; Luo and Al-Dahhan., 2011; Zhang et al., 2012; Zhang 2013; Zhang et al., 2013; Prussi et al., 2014; Delafosse et al., 2015). Some researchers further coupled the light field simulation to analysis the light/dark cycles (Pruvost et al., 2008; Wu et al., 2010; Sato et al., 2010; Huang et al., 2014; 2015; Zhang et al., 2015; Krujatz et al., 2015), which is a useful way to optimize the reactor geometry or internals and illumination method. The equation of motion of particles is given by the Newton equation,

$$\frac{d\vec{X}_s}{dt} = \vec{u}_s \quad (2.5)$$

$$m_s \frac{d\vec{u}_s}{dt} = \vec{F}_D + \vec{F}_{VM} + \vec{F}_p + \vec{F}_G + \vec{F}_B \quad (2.6)$$

Where  $x_s$ ,  $u_s$ ,  $m_s$  is the position, velocity and mass of particles, respectively. The right hand side represents the drag, virtual mass, pressure gradient, gravity and buoyancy forces exerted on particles. Since the density of microalgae cell is equal or slightly heavier than culture media, some authors only include the most important drag force (Krujatz et al., 2015; Gao et al., 2016b). Because most algae cell size is in the order of 10 micro, which is smaller than the Kolmogorov scale, microalgae cell can be considered as massless tracer particle that no force is exerted on it and has the same boundary conditions with fluid (Pruvost et al., 2008; Sato et al., 2010; Huang et al., 2014; 2015). When the liquid flow is in the turbulent regime, only the Reynolds averaged liquid velocity is considered in equation (2.6) and the fluctuating part of the liquid velocity is remained to be formulated. Usually, the fluctuating part of the fluid velocity is determined using a stochastic model, which is a function of the liquid turbulent kinetic energy.

### **2.1.3. Turbulence simulation**

Turbulence takes an important role in the random movement of algae cell in photobioreactor, which have an impact on its light attenuation. To address this effect, an accurate multiphase turbulence model is needed. For multiphase turbulent reacting flow simulation in photobioreactor, Reynolds-averaged Navier-Stokes (RANS) model is mainly used, which gives the mean phase velocity and averaged quantities describing the turbulence. For liquid-gas turbulence simulation, three different kinds of models are available, namely the mixture turbulence model, the dispersed turbulence model and the per-phase turbulence model. The dispersed turbulence model is commonly used, where the liquid phase turbulence

is modeled using either an eddy viscosity model or a Reynolds stress model, while the gas phase is assumed to be laminar due to low flow rates usually employed. It can be seen from Table 2.1, for bubble column (Mortuza et al., 2012; Seo et al., 2012; Nauha and Alopaeus, 2013; 2015; Gerdes et al., 2014; Gerdes et al., 2014; Bari et al., 2014; 2015), airlift (Luo and Al-Dahhan, 2011; Massart et al., 2014; Soman and Shastri, 2015), flat plate (Shu et al., 2010; Zhang et al., 2012; Huang et al., 2014; 2015a;2015b; Wang et al., 2014; Chen et al., 2016 ) and raceway reactor (Xu et al., 2014; Hreiz et al., 2014; Prussi et al., 2014; Park and Li, 2015; Zhang et al., 2015; Huang et al., 2015c; Zeng et al.,2016), the standard k- $\epsilon$  turbulence model and its variants were widely used to model the liquid turbulence because of its simplicity and lesser computational expensive. Sometimes the k- $\epsilon$  turbulence model was modified to account for the bubble induced turbulence (Luo and Al-Dahhan, 2011; Li et al., 2012). For some reactors with rotation flow, the k- $\epsilon$  turbulence model usually performs not well than the k- $\omega$  turbulence model and Reynolds stress turbulence models. For example, Pruvost et al. (2004) compared the k- $\epsilon$  model, k- $\omega$  model and a Reynolds stress model and found that the k- $\omega$  model give the most accurate prediction in a torus shape reactor. Gao et al. (2015b) found that k- $\omega$  turbulence model and Remolds stress turbulence models give better predictions than k- $\epsilon$  turbulence model in a Taylor-Couette reactor.

Table 2.1. List of CFD simulations of flow hydrodynamics in photobioreactors in the last decade.

Authors	PBR type	Phase	CFD approach	Turbulence model	CFD code	Focus of the study
Pruvost et al. (2006)	Torus	L	E	k- $\omega$	FLUENT	Mixing performance, lateral dispersion
Pruvost et al. (2008)	Torus	L-S	E-L	k- $\omega$	FLUENT	Mixing influence on light conversion, cell trajectory tracking
Wu et al., (2010)	Spiral tube	L-S	E-L	k- $\epsilon$	FLUENT	Mixing in novel reactor, cell trajectory tracking

Table 2.1. Continued

Sato et al. (2010)	virtual	L-G-S	E- L-L	LES	FLUENT	Cell trajectory tracking
Shu et al., (2010)	Flat plate	L-S	E-L	NA	FLUENT	Flow field, cell trajectory tracking
Marshall et al., (2011)	Pipe	L-S	E-L	k- $\epsilon$	NA	Effect of turbulent mixing on algae growth rate
Luo and Al-Dahhan (2011)	Airlift	L-G-S	E- E-L	k- $\epsilon$ with BIT	CFX	Multiphase CFD model development
Smith et al. (2012)	Flooded bed	L-G	E- E	k- $\epsilon$	FLUENT	Optimum design and operating conditions
Xu et al., (2012)	Draft-tube airlift	L-G	E- E	k- $\epsilon$	FLUENT	Optimize the inner structure
Zhang et al., (2012)	Flat Plate	L-S	E-L	k- $\epsilon$	FLUENT	Effect of inclined baffles on flow field and algae growth
Mortuza et al., (2012)	Bubble column	L-G	E- L	k- $\epsilon$	Star-CCM	Bubble and liquid circulation patterns
Seo e al., (2012)	Bubble column	L-G	E-E, Mixture, VoF, E-L	Laminar	FLUENT	Compare four different multiphase models
Moberg et al., (2012)	Tubular	L-G	E- L	k- $\epsilon$	FLUENT	Cell trajectory tracking
Li et al., (2012)	Oscillating airlift loop	L-G	E- E	k- $\epsilon$ with BIT	FLUENT	Flow and mass transfer in novel reactor
Zhang (2013)	Stirred tank	L-S	E- L	k- $\epsilon$	COMSO L	Flow field, cell trajectory tracking
Nauha and Alopaeus (2013)	Bubble column	L-G	E- E	k- $\epsilon$	FLUENT	Combining fluid dynamics with algal growth
Zhang et al., (2013)	Tubular	L-S	E- L	k- $\epsilon$	FLUENT	Flow field, cell trajectory tracking
Bari et al., (2014)	Bubble column	L-G	E-L	k- $\epsilon$	Star-CCM	Flow patterns and heat transfer effects
Bitog et al., (2014)	Bubble column	L-G	E-L	k- $\epsilon$	FLUENT	Optimization hydrodynamics parameters
Wang et al., (2014)	Flat plate	L-G	E- E	k- $\epsilon$	CFX	Structural optimization and cultivation performance
Delafosse et al., (2014)	Stirred tank	L	E	k- $\epsilon$	FLUENT	CFD-Compartment model
Gerdes et al., (2014)	Bubble column	L-G	E-L	k- $\epsilon$	Star-CCM	Placement of light guides arrays
Xu et al., (2014)	Raceway	L-G	VoF	k- $\omega$	FLUENT	Flow mixing features
Hreiz et al., (2014)	Raceway	L-G	VoF	k- $\epsilon$	FLUENT	Effects of the paddlewheel speed and geometry
Prussi et al., (2014)	Raceway	L-G-S	VoF-L	NA	OpenFoam	Vertical mixing, cell trajectory tracking
Massart et al., (2014)	Airlift	L- G	E- L	k- $\epsilon$	FLUENT	Mixing optimization
Huang et al., (2014)	Flat plate	L-G-S	E-E-L	k- $\epsilon$	CFX	Novel internal mixers, cell trajectory tracking
Bari et al., (2015)	Bubble column	L-G	E-L	k- $\epsilon$	Star-CCM	Flow patterns and heat transfer effects

Table 2.1. Continued

Park and Li (2015)	Raceway	L	E	k- $\epsilon$	FLUENT	Integration of Biological Kinetics with CFD
Gómez-Pérez (2015)	Tubular	L- G	E- L	k- $\epsilon$	COMSO L	Effect of wall turbulence promoters
Meng et al., (2015)	Circular ponds	L	E	k- $\epsilon$	CFX	Flow characteristics using various impellers
Delafosse et al., (2015)	Stirred tank	L-S	E- L	k- $\epsilon$	Fluent	CFD-based compartment model
Zhang et al., (2015)	RacewaY	L-S	E- L	k- $\epsilon$	CFX	Flow deflectors and wing baffles to reduce dead zone and enhance flashing light effect
Nauha and Alopaeus (2015)	Bubble columns	L- G	E- E	k- $\epsilon$	FLUENT	Compartmental modeling approach
Zhang et al., (2015)	Flat plate	L- G	E- E	k- $\epsilon$	FLUENT	Integration of light, growth kinetics, and fluid dynamics
Krujatz et al., (2015)	Stirred tank	L-S	E- L	k- $\epsilon$	COMSO L	Fluid flows pattern and cellular trajectories
Soman and Shastri (2015)	Airlift and Flat plate	L-Gas	E- E	k- $\epsilon$	FLUENT	Compare performance of novel and airlift PBR
Huang et al., (2015a)	Flat plate	L-G-S	E-E-L	k- $\epsilon$	CFX	Hydrodynamic and light regime characteristics of three types of flat-plate PBRs
Huang et al., (2015b)	Flat plate	L-G-S	E-E-L	k- $\epsilon$	CFX	Effect of novel internal mixture on biomass production
Huang et al., (2015c)	Raceway	L	E	k- $\epsilon$	CFX	Effects of sloping baffles and flow deflectors
Gao et al. (2015b; 2016a)	Taylor Couette	L-G	E- E	k- $\omega$	FLUENT	Bubble spatial distribution mechanism
Gao et al. (2015a)	Taylor Couette	L-G	E- E	k- $\omega$	FLUENT	A novel adaptive Gas-liquid mass transfer model
Gao et al. (2016b)	Taylor-Couette	L-G-S	E-E-L	k- $\omega$	FLUENT	Cell trajectory tracking, effect of mixing on biomass production
Zeng et al. (2016)	Raceway	L	E	k- $\epsilon$ , LES	CFX	Effects of different types of paddle wheels
Cheng et al., (2016)	Tubular	L	E	k- $\epsilon$	CFX	Effect of novel static mixers on mixing characteristics
Chen et al. (2016)	Flat plate airlift	L-G	E- E	k- $\epsilon$	CFX	Effects of two types of baffles on mass transfer

#### 2.1.4. Mass transfer simulation

In biological reactors, the transport of gas phase species such as oxygen and carbon dioxide to and from microorganisms can be represented by several steps and resistances, including transit from bubbles to gas-liquid interface, gas film, liquid film around bubbles, bulk liquid mixing, liquid film around microorganism and transit from liquid-cell interface to the site of biochemical reaction (Kraakman et al., 2011; Garcia-Ochoa and E. Gomez, 2009). Commonly, the liquid film resistances around bubbles control the overall transfer rate. The liquid side volumetric mass transfer is difficult to estimate as it is affected by many factors, such as gas holdup, bubble size, slip velocity and turbulent energy dissipation rate. These factors in return depend non-trivially on reactor operating conditions, geometry, and physical properties of the gas and liquid phases. Accurate prediction of interphase mass transfer coefficients is crucial for reactor design and optimization. Penetration model (Higbie, 1935) and eddy cell model (Lamont and Scott, 1970) are the most widely used models for theoretical prediction of gas-liquid mass transfer coefficient in biological reactors, such as bubble column (Kawase et al., 1987; Wang et a., 2007), airlift (Kawase et al., 1996; Huang et al., 2010; Li et al., 2012; Chen et al., 2016) and stirred tank (Linek et al., 2004). The penetration theory proposed by Higbie assumes that bubble surfaces are immobile, but it accounts for unsteady diffusion of gas into the liquid at the gas-liquid interface, which can be expressed as follows:

$$k_L = F \sqrt{\frac{4D_L u_{slip}}{\pi d_b}} \quad (2.7)$$

where F is a constant.

The eddy cell model assumes that the liquid side mass transfer is controlled by interfacial surface renewal by small scale eddies rather than by any measure of the mean flow of the liquid relative to the bubbles, such as the slip velocity, which can be expressed as

$$k_L = K \sqrt{\frac{4D_L}{\pi} \left(\frac{\varepsilon_l}{\nu_l}\right)^{1/2}} \quad (2.8)$$

where K is a constant.

The penetration theory model is known to underpredict mass transfer for highly turbulent flows, while the eddy cell model is known to underpredict mass transfer for weakly turbulent flows. Recently, Gao et al. (2015a) introduced an adaptive mass transfer model that automatically adapts to the local hydrodynamic environment by computing exposure time using either the penetration theory or eddy cell model based upon the turbulent dissipation rate. The adaptive mass transfer model can be expressed as follows,

$$k_L = \max\left(F \sqrt{\frac{4D_L}{\pi} \frac{u_{slip}}{d_b}}, K \sqrt{\frac{4D_L}{\pi} \left(\frac{\varepsilon_l}{\nu_l}\right)^{1/2}}\right) \quad (2.9)$$

By comparing the simulation predictions with data from corresponding oxygen mass transfer experiments (Ramezani et al., 2015), it is demonstrated that this adaptive mass transfer model provides an excellent description for both the local and global mass transfer of oxygen in a semi-batch gas-liquid Taylor-Couette bioreactor for a wide range of azimuthal Reynolds numbers and axial gas flow rates.

## 2.2. Light transport simulation

Microalgae cannot grow without photosynthesis. Light availability and light intensity are the main factors in controlling cell growth. When light passes through the medium in

photobioreactors, light intensity will decrease due to the absorption and scattering of microalgae cells or bubbles. The light attenuation becomes more serious when the reactors are operated at high microalgae cell concentrations and large light-path length. The main factor affecting light attenuation includes properties of reactor wall, light-path length, cell concentration, cell diameter and shape, cell pigment fraction, bubbles if presented and so on. Different methods and models proposed in literature can be used to predict the light transfer, including Beer-Lambert law, two-flux approximation, solving radiation transport equations and so on.

### 2.2.1. Beer-Lambert law and its variant

To avoid solving the complex three-dimensional radiation transport equation, light distribution at some specific conditions can be described by the commonly used Beer-Lambert law (Lee et al., 1987; Rorrer and Mullikin, 1999; Pruvost et al., 2002; Muller-Feuga et al., 2003; Bosma et al., 2007),

$$I(L) = I_0 e^{-\alpha L}, \quad \alpha = \sigma C_b \quad (2.10)$$

Where  $I(L)$  is the local light intensity,  $I_0$  is the incident light intensity,  $L$  is the light-path length,  $C_b$  is the biomass concentration,  $\alpha$  is light attenuation coefficient and  $\sigma$  is the extinction coefficient. The extinction coefficient usually was assumed to be a constant, sometimes it was assumed to be function of pigment concentration (Acién Fernández et al., 1997; 1998).

To apply the Beer-Lambert law, the following assumptions are required to fulfill: monochromatic and collimated light, well-mixed and transparent medium and no light

scattering. However, in some conditions, such as non-transparent medium or larger cell concentration, light attenuation law will deviate the Beer-Lambert law, where  $\alpha$  is assumed to be proportional to the cell concentration. Thus to overcome the limitation of Beer-Lambert law, several empirical correlations of  $\alpha$  were developed, such as linear type (Luo and Al-Dahhan, 2004; Benson and Rusch, 2006) and hyperbolic type correlations. Luo and Al-Dahhan (2004) proposed a linear type correlation of  $\alpha$  for *Porphyridium sp.* in non-transparent medium:

$$\alpha = k_b C_b + k_w \quad (2.11)$$

Where  $k_w$  and  $k_b$  are extinction coefficients accounting for water medium and self-shading effects between biomass cells, respectively. Ación Fernández et al. (1997) found that light attenuation does not change linearly with concentration above 1.3 g/L for *Phaeodactylum tricornutum* and proposed a hyperbolic type correlation of  $\alpha$ :

$$\alpha = \frac{1}{L_{av}} \frac{\alpha_{\max}}{k + C_b} \quad (2.12)$$

Where  $\alpha_{\max}$  is the maximum attenuation possible and  $k$  is a constant. Suh and Lee (2003) and Yun and Park (2003) also proposed their hyperbolic type correlations to describe the light attenuation and found the hyperbolic type models have good prediction in a wide range of cell concentration.

### 2.2.2. Two-flux approximation

Culture medium can no longer be treated as uniform when the cell concentration is relatively high, and both cell absorption and scattering contribute to light attenuation. Thus, using Beer-Lambert law to predict the light attenuation will bring large derivation as it only

considers cell absorption while neglects scattering. Cornet et al. (1994; 1995) proposed a light attenuation model by solving the RTE using the two-flux approximation to model light transfer in cyanobacterium *Spirulina platensis* culture. The model considers both cell absorption and scattering. The model is expressed as follows:

$$\alpha = \frac{1}{L} \ln \frac{4\alpha_1}{(1+\alpha_1)^2 e^{\alpha_2} - (1-\alpha_1)^2 e^{-\alpha_2}} \quad (2.13)$$

where  $\alpha_1 = \sqrt{E_a / (E_a + E_s)}$ ,  $\alpha_2 = \alpha_1 C_b L (E_a + E_s)$ .  $E_a$  and  $E_s$  are absorption and scattering coefficients, respectively. Note that, setting  $\alpha_1 = 1$  and  $E_s = 0$ , it can be changed back to Beer-Lambert law.

Cornet et al. (1998) applied this model to several kinds of photobioreactors to model light attenuation of *Spirulina platensis*, and gave the values of  $E_a$  and  $E_s$  to be  $150 \text{ m}^2/\text{kg}$  and  $200 \text{ m}^2/\text{kg}$ , respectively. Pottier et al. (2005) applied the model in torus photobioreactor to model the light attenuation of *Chlamydomonas reinhardtii*. They proposed similar expressions for  $\alpha_1$  and  $\alpha_2$  and gave the values of  $E_a$  and  $E_s$  to be  $172 \text{ m}^2/\text{kg}$  and  $868 \text{ m}^2/\text{kg}$ , respectively. Both of the research show that cell scattering cannot be neglected.

### 2.2.3. Solving radiation transport equation (RTE)

Without simplification, the radiation transport equation can be solved numerically. The radiative transfer equation (RTE) for an absorbing, emitting, and scattering medium at position  $\vec{r}$  in the direction  $\vec{s}$  is (Kong et al., 2014)

$$\frac{dI_\lambda(\vec{r}, \vec{s})}{ds} + (a_\lambda + \sigma_{s,\lambda}) I_\lambda(\vec{r}, \vec{s}) = an^2 \frac{\sigma T^4}{\pi} + \frac{\sigma_{s,\lambda}}{4\pi} \int_0^{4\pi} I_\lambda(\vec{r}, \vec{s}') \Phi_\lambda(\vec{s}, \vec{s}') d\Omega' \quad (2.14)$$

Where  $a_\lambda$  is wavelength-dependent absorption coefficient,  $\sigma_{s,\lambda}$  is wavelength-dependent scattering coefficient and  $\Phi_\lambda$  is the wavelength-dependent phase function. The phase function  $\Phi_\lambda$  describes the angular distribution of light reflected from a body when illuminated from a specific direction. It is complex to solve, the simplest way is to assume that the angular distribution is isotropic and equal to 1. If the cell concentration, pigment fraction, cell shape and size are known, accurate phase function can be obtained by Mie theory. The use of Mie's method is in principle valid for all particle sizes and wavelengths, but for particle sizes much smaller than the radiation wavelength the Rayleigh approximation is most often used. For particle sizes much larger than the radiation wavelength, the particle can be treated as a macroscopic surface and simple ray tracing methods are applicable. Also, the absorption and scattering coefficients can be obtained by Mie's method, their independence on wavelength can be obtained by light spectroscopy method as well.

Several numerical methods can be used to solve the radiation transfer equation, and are available in commercial software, such as ANSYS FLUENT (Fluent theory guide, 2011). The Monte Carlo (MC) method, discrete ordinate (DO) method and finite volume method (FV, a conservative variant DO method) are commonly used to model the radiation transfer in photobioreactors, as they can be used to model non-gray radiation and semi-transparent walls of various types (Moses, 1993). Csögör et al. (2001) studied the effect of cell absorption and scattering, reactor surface and bubbles on light attenuation using Monte Carlo method in a novel stirred draught tube reactor. Heinrich et al. (2012a; 2012b) developed a Monte Carlo program to simulate the illumination conditions in open ponds and agree well with experiments. Monte Carlo method is good for complex geometry photobioreactor, while it is

computationally expensive and it is difficult to couple with a fluid solver. Consequently, the FV method for solving the RTE in photobioreactor was widely employed (Duran et al., 2010; Huang et al., 2011; Kong et al., 2014) as the computational cost is moderate for typical angular discretization and it is easy to solve with other transport equations. Huang et al. (2011) modeled the radiation field in a cylindrical photobioreactor and showed that the validated FV method can model a wide range of optical thickness with absorption, scattering and wall reflection. While they neglected spectral dependencies. Kong and Vigil (2014) solved a multidimensional spectral radiation transport model using FV method in an asymmetrically lighted cylindrical photobioreactor and validated by experimental photon flux measurements.

#### **2.2.4. RTE considering bubbles effect**

The above models mainly consider the effect of cell on light attenuation, while the effect of bubbles was not considered. Mirón et al. (1999) found bubbles may enhance or reduce light intensity in bubble columns. Gas bubbles generally enhance internal irradiance when the Sun is low on the horizon. While near solar noon, the bubbles diminish the internal column irradiance relative to the ungassed state. Krishnamoorthy et al. (2014) numerically investigated the radiative transfer in gas-liquid bubble column by solving RTE coupling four different multiphase modeling approaches. The impacts of the multiphase hydrodynamic modeling strategy, initial bubble diameter, and operational parameters on the radiation distribution patterns within the reactor were examined. Berberoglu et al. (2007) solved a one-dimensional RTE considering absorption by both *Anabaena variabilis* and by the liquid phase

as well as for anisotropic scattering by the bubbles and the bacteria. The one-dimensional RTE can be written as

$$\begin{aligned} \vec{s} \cdot \frac{dI_\lambda(z, \vec{s})}{dz} + (a_{eff, \lambda} + \sigma_{eff, \lambda}) I_\lambda(\vec{r}, \vec{s}) &= \frac{\sigma_\lambda}{4\pi} \int_0^{4\pi} I_\lambda(z, \vec{s}') \Phi_{C, \lambda}(\vec{s}, \vec{s}') d\Omega' s \\ &+ \frac{\sigma_\lambda}{4\pi} \int_0^{4\pi} I_\lambda(z, \vec{s}') \Phi_{b, \lambda}(\vec{s}, \vec{s}') d\Omega' s \end{aligned} \quad (2.15)$$

Where  $a_{eff, \lambda}$  and  $\sigma_{eff, \lambda}$  is the effective absorption coefficient and scattering coefficient accounts for the absorption or scattering by the bubble phase and by the microorganisms at wavelength  $\lambda$ , respectively.  $\Phi_{C, \lambda}$  and  $\Phi_{b, \lambda}$  is the scattering phase functions of bacteria and bubbles at wavelength  $\lambda$ , respectively. They found that the anisotropic scattering by bubbles should be accounted as the fact that scattering becomes important as the interfacial area concentration increases.

### 2.3. PSU-based algae growth rate model

Mathematical models of photosynthesis in photobioreactors are of great importance for both basic scientific study and bioprocess industrial applications. A variety of mathematical models have been developed to express the relationship between photosynthetic rate and light intensity. The photosynthesis models can be divided into three types based on their ability to account for light gradients and short light cycles (L/D cycle) (see good review, Béchet et al., 2013). Type A models predict the rate of photosynthesis of the entire culture as a function of the incident or average light intensity reaching the culture (Lee et al., 1987; Jeon et al., 2005; Ogbonna et al., 1995). The assumption of this approach is that individual algae cells are in a well-mixed dilute system and exposed to the same averaged light intensity. Thus this model cannot account for the short light cycles experienced by microalgae in dense cultures. Type B

models consider the impact of light gradients on the local rate of photosynthesis (Yun and Park, 2003; Bosma et al., 2007; Cornet et al., 1995; Grobbelaar, 1990) without consideration of short light cycles, which may overestimate the impact of light-inhibition (Bosma et al., 2007). Type A and B models are empirical or semi-empirical models, which can fit the observed experimental data well by adjusting model parameters, while they have limitations for a wide application. Type C models can consider both the light gradients and light/dark cycles, which are called as mechanistic models. The mechanistic models can be divided into two categories: physiological models and PSU-base model (Bernardi et al., 2014). Physiological models attempt to describe the dynamic behavior of photosynthetic cells and proposed approximations for the actual mechanism involved in the cell's growth (Ross and Geider, 2009; Marshall et al., 2000; Pahlow and Oschlies, 2009; Kroon and Thoms, 2006), which is extremely complex and difficult to couple with computational models for engineering uses. Instead, most biological models that focus on the concepts of photosynthetic units (PSUs), which are called state model or photosynthetic unit model (PSU model) or photosynthetic factory model (PSF model), are friendly for simulating and optimizing industrial cultivation systems. The photosynthetic unit is a hypothetical light-harvesting unit of photosynthesis that, in green plants, comprises about 300 light-absorbing molecules with a molecule of chlorophyll acting as the reaction center. The PSUs can exist in different states. Usually, three or four states are assumed. For transitions between states, different researchers proposed different expressions according to different theories and assumptions.

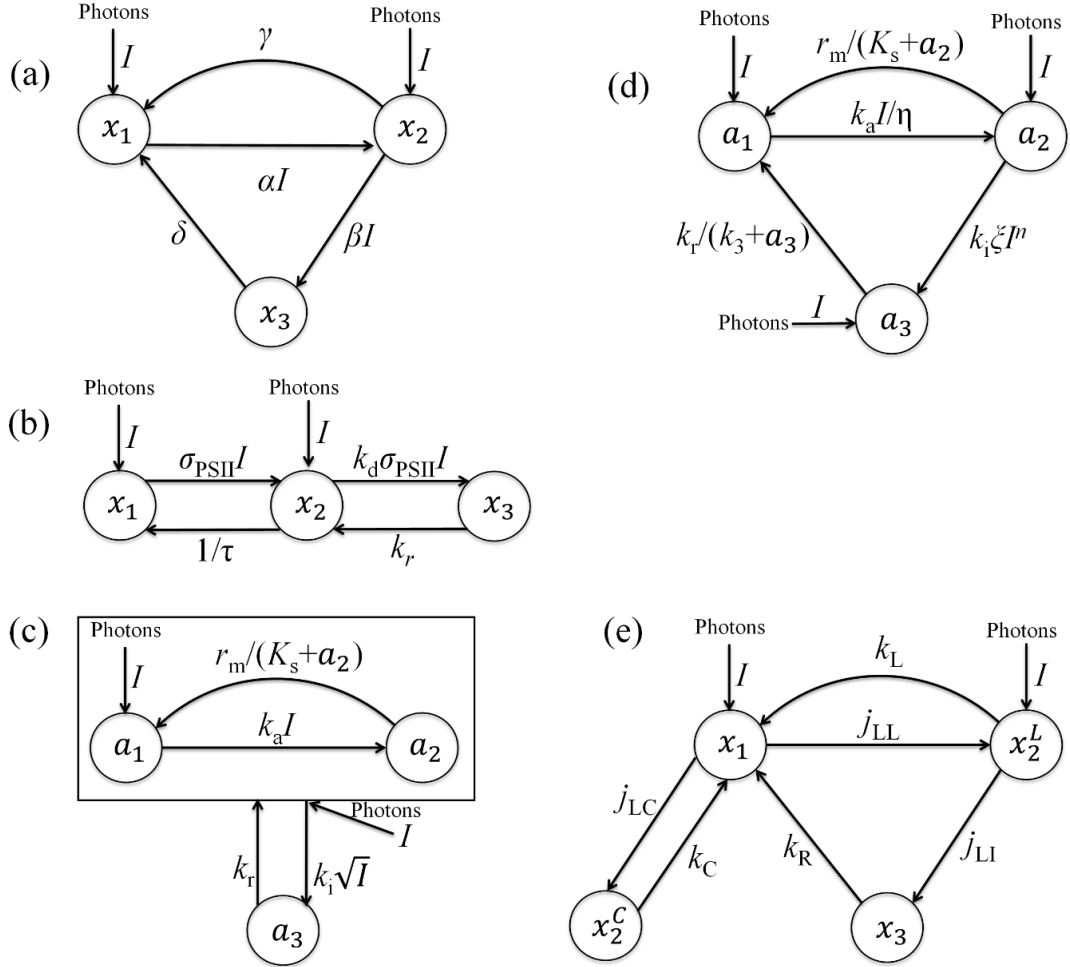


Figure 2.1. (a) Scheme of Eilers-Peeters model.  $x_1$ ,  $x_2$  and  $x_3$  represent the fractions of PSUs in resting, active and inhibited states, respectively. (b) Scheme of Han model. (c) Scheme of Camacho Rubio et al model.  $a_1$ ,  $a_2$  and  $a_3$  represent the numbers of PSUs in resting, active and inhibited states, respectively. (d) Scheme of Garcia Camacho et al model. (e) Scheme of Papadakis et al model. When the excitation energy is allocated to the linear electron flow, the PSU in active state is denoted as  $x_2^L$ , and when it is allocated to the cyclic electron flow, the PSU in active state is denoted as  $x_2^C$ .

### 2.3.1. Eilers-Peeters model

In Eilers and Peeters model (Eilers and Peeters, 1988; 1993), PSUs are assumed to exist in three states, the resting state (or open state,  $x_1$ ), the active state (or closed state,  $x_2$ ) and the inhibited state ( $x_3$ ) as shown in Figure 2.1a. The light and dark reactions are modeled by changes in the states of PSUs. The PSUs in the resting state can transfer to the active state when it captures a number of photons. The PSUs in the active state can either return to the resting state pass down the energy to start the dark phase of photosynthesis or be inhibited by capturing another number of photos to the inhibited state. The PSUs in the inhibited state can eventually recover and go back to the resting state. The transitions between states can be described by the following equations (Wu and Merchuk, 2001):

$$\frac{dx_1}{dt} = -\alpha I x_1 + \gamma x_2 + \delta x_3 \quad (2.16a)$$

$$\frac{dx_2}{dt} = \alpha I x_1 - \gamma x_2 - \beta I x_2 \quad (2.16b)$$

$$x_1 + x_2 + x_3 = 1 \quad (2.17)$$

The specific growth rate was expressed as:

$$\mu = k \gamma x_2 \quad (2.18)$$

It can be seen from the above equations, the transition involving abortion of light is assumed to be first order with respect to light intensity, the other two transitions are assumed to be zero order with respect to light intensity. The specific growth rate  $\mu$  was assumed to be proportional to the active state fraction. At very low or no light intensity, the growth rate may be negative due to aspiration. Wu and Merchuk (2001) revised the Eilers-Peeters model by adding a maintenance coefficient  $M$ , which corresponds to the energetic requirements for

internal metabolism and allows the negative growth rate in light condition below the compensation point.

The revised specific growth rate can be expressed as follows:

$$\mu = k\gamma x_2 - M \quad (2.19)$$

The set of parameters in the revised Eilers-Peeters model can be represented by vector  $P^{EP} = [\alpha, \beta, \gamma, \delta, k, M]$ .

### 2.3.2. Han model

The Han model is inspired by the EPM. PSUs are assumed to exist in three states, the resting state ( $x_1$ ), the active state ( $x_2$ ) and the inhibited state ( $x_3$ ) as shown in Figure 2.1b. The model considered that photoinhibition is due to damage to D1 protein when organisms are exposed to high radiance, corresponding to the transition from active state to inhibited state. The repair of damaged PSUs by enzymatic process in cells was modeled by transition from inhibited state to active state, which is different with EPM that was modeled by transition from inhibited state to resting state. The Han model equations are as follows:

$$\frac{dx_1}{dt} = -\sigma I x_1 + \frac{1}{\tau} x_2 \quad (2.20a)$$

$$\frac{dx_2}{dt} = \sigma I x_1 - \frac{1}{\tau} x_2 + k_r x_3 - k_d \sigma I x_2 \quad (2.20b)$$

$$\frac{dx_3}{dt} = -k_r x_3 + k_d \sigma I x_2 \quad (2.20c)$$

$$x_1 + x_2 + x_3 = 1 \quad (2.21)$$

The photosynthetic response to irradiance at steady state was as follows:

$$\mu = N \frac{\sigma I}{1 + \sigma I \tau + (k_d / k_r)(\sigma I)^2 \tau} \quad (2.22)$$

The set of parameters in Han model can be represented by vector  $P^{EP} = [\sigma, \tau, k_r, k_d]$ .

### 2.3.3. Nikolaou et al. model

Nikolaou et al. (2016) revised the Han model by considering photoacclimation. Photoacclimation is the process that microalgae adapt to a particular light intensity by adjusting chlorophyll content and the pigment composition. The photoacclimation in this mode was described by accounting for the change in the chlorophyll content over time. The parameters  $N$  and  $\sigma$  were described as functions of the chlorophyll quota  $\theta$ . The Nikolaou et al. model equations are as follows:

$$\frac{dx_1}{dt} = -\sigma(\theta)Ix_1 + \frac{1}{\tau}x_2 \quad (2.23a)$$

$$\frac{dx_2}{dt} = \sigma(\theta)Ix_1 - \frac{1}{\tau}x_2 + k_r x_3 - k_d \sigma(\theta)Ix_2 \quad (2.23b)$$

$$\frac{dx_3}{dt} = -k_r x_3 + k_d \sigma(\theta)Ix_2 \quad (2.23c)$$

$$x_1 + x_2 + x_3 = 1 \quad (2.24)$$

The photosynthetic response to irradiance at steady state was as follows:

$$\mu = N(\theta) \frac{\sigma(\theta)I}{1 + \sigma(\theta)I\tau + (k_d / k_r)(\sigma(\theta)I)^2 \tau} \quad (2.25)$$

The set of parameters in Han model can be represented by vector  $P^{EP} = [\sigma, \tau, k_r, k_d]$ .

### 2.3.4. Camacho Rubio et al. model

In the model by Camacho Rubio et al. (2003) PSUs are also assumed to exist in three states, the open state ( $a_1$ ), the closed state ( $a_2$ ) and the inhibited state ( $a_3$ ) as shown in Figure 2.1c. Not only photoinhibition but also photoacclimation were considered in this model. Also, transitions among PSU states are quite different with Eilers-Peeters model. In this model, the transition from active state to resting state was assumed to obey a Michaelis-Menten type relationship. The photoinhibition rate is assumed to be proportional to the sum of resting states and active states, while it is proportional to only active state in Eilers-Peeters model. Also, according to the experimental work of Nedbal et al. (1996), the photoinhibition reaction rate is proportional to the square root of light intensity. CRM assumes that the total PSU numbers are a function of light intensity to consider photoacclimation, while EPM does not consider photoacclimation and assumes that the number of PSUs is constant with respect to light intensity.

The CRM equations are as follows:

$$\frac{da_2}{dt} = k_a I a_1 - \frac{r_m}{K_s + a_2} a_2 \quad (2.26a)$$

$$\frac{da_3}{dt} = k_i \sqrt{I} (a_1 + a_2) - k_r a_3 \quad (2.26b)$$

$$a_1 + a_2 + a_3 = a_t \quad (2.27)$$

$$a_t = \frac{r_m}{k_c + \frac{k_a k_r}{k_i} \sqrt{I}} \quad (2.28)$$

The specific growth rate can be expressed as follows:

$$\mu = k_p \frac{r_m}{K_S + a_2} a_2 - M \quad (2.29)$$

The set of parameters in CRM can be represented by vector  $P^{CR} = [k_a, k_i, k_r, k_p, k_c, K_S, r_m, M]$ .

### 2.3.5. Bernardi et al. model

Bernardi et al. (2013) modified the CRM model and proposed an enhancing CRM. They assumed that the photoinhibition does not depend on the number of closed PSUs, but is simply related to light intensity based on the founding of some work that PSII photoinhibition occurs at all light intensities. Above a saturated light intensity for photosynthesis, a photoprotection process is activated. The light exponents in photoinhibition and photoacclimation were replaced by additional parameters  $\alpha_1$  and  $\alpha_2$  to allow for a higher flexibility. Also, the constant maintenance factor in CRM was modified as a function of light intensity to account for the metabolic cost of repairing damaged PSUs. The enhancing CRM equations are as follows:

$$\frac{da_2}{dt} = k_a I a_1 - k_d a_2 \quad (2.30a)$$

$$\frac{da_3}{dt} = \begin{cases} k_{i,0} I a_t - k_r a_3 & I \leq I_{cr} \\ k_{i,0} I_{cr} a_t + k_{i,1} (I - I_{cr})^{\alpha_1} (a_1 + a_2) - k_r a_3 & I > I_{cr} \end{cases} \quad (2.30b)$$

$$a_1 + a_2 + a_3 = a_t \quad (2.31)$$

$$a_t = \frac{1}{k_c + I^{\alpha_2}} \quad (2.32)$$

The specific growth rate can be expressed as:

$$\mu = k_p k_d a_2 - (M_o + k_M q_{\max} \frac{a_3}{a_t}) \quad (2.33)$$

The set of parameters in CRM can be represented by vector  $P^{CR} = [k_a, k_d, k_{i,0}, k_{i,1}, k_r, k_p, k_c, k_M, \alpha_1, \alpha_2, M_0]$ .

### 2.3.6. Garcia-Camacho et al. model

Garcia-Camacho et al. (2012) proposed a photosynthesis model (Figure 2.1d) based on the CRM in. In CRM, the expression of the total number for PSUs is in the steady state form, which cannot describe the kinetics of dynamic photoacclimation process. Garcia Camacho et al. (2012) aware of this limitation and proposed a new expression, in which the total numbers of PSUs is a function of both light intensity and time. The transitions between PSU states are different with CRM, while similar with EPM. Also, in this model, the respiration was divided into dark respiration and photorespiration. The GCM equations are as follows:

$$\frac{da_2}{dt} = \frac{k_a I}{\eta} a_1 - \frac{r_m}{K_S + a_2} a_2 - k_i \xi I^n a_2 \quad (2.34a)$$

$$\frac{da_3}{dt} = k_i a_2 - \frac{k_r}{k_3 + a_3} a_3 \quad (2.34b)$$

$$a_1 + a_2 + a_3 = a_t \quad (2.35)$$

$$a_t = \frac{a_{ad,f}}{1 + (a_{ad,f} - a_{ad,0}) / a_{ad,0} e^{-K_{PSU} t}} \quad (2.36)$$

The specific growth rate can be expressed as:

$$\mu = \frac{1}{1 + \gamma} \left( \frac{k_p r_m}{K_S + a_2} a_2 - M_0 - \mu_R \right) \quad (2.37)$$

The set of parameters in CRM can be represented by vector  $P^{CR} = [k_a, k_i, k_r, k_p, k_c, k_M, \alpha_1, \alpha_2, \eta, \gamma, r_m, K_{PSU}, K_S, M_0, \mu_R]$ .

### 2.3.7. Papadakis et al. model

Papadakis et al. (2012) model follows the assumption of transitions of PSUs between three states (resting, active and inhibited states) and further distinguish active PSUs that server the linear electron flow (LEF) and the cyclic electron flow (CEF) to model the photoacclimation process. It can be thought as a four states model. The partition of the excitation energy is based on the relative availability of light and dissolved inorganic carbon (DIC). The energy allocation to LEF increases as light intensity decreases and/or DIC availability increases. The Papadakis et al. model equations are as follows:

$$\frac{dx_1}{dt} = -j_{LL}x_1 - j_{LC}x_1 + k_Lx_2^L + k_Cx_2^C + k_Rx_3 \quad (2.38a)$$

$$\frac{dx_2^L}{dt} = j_{LL}x_1 - j_{LI}x_2^L - k_Lx_2^L \quad (2.38b)$$

$$\frac{dx_2^C}{dt} = j_{LC}x_1 - k_Cx_2^C \quad (2.38c)$$

$$\frac{dx_3}{dt} = j_{LI}x_2^L - k_Rx_3 \quad (2.38d)$$

$$x_1 + x_2^L + x_2^C + x_3 = 1 \quad (2.39)$$

The specific production rates of the LEF and CEF are given by

$$\mu_L = y_L k_L x_2^L \quad (2.40a)$$

$$\mu_C = y_C k_C x_2^C \quad (2.40b)$$

The set of parameters in Papadakis model can be represented by vector  $P^p = [j_{LL}, j_{LC}, j_{LI}, k_L, k_C, k_R]$ .

#### 2.4. Comprehensive coupling and simulation

It is extremely complex to develop a comprehensive model to predict the biomass production in a PBRs as transport and reaction phenomenon in photobioreactors is coupled at multi-time scales. Radiation transport is very fast and is characterized by a time scale of  $10^{-10}$  seconds. Turbulent diffusion and mass transfer is characterized by a time scale of several seconds (Gao et al., 2015b). While the characteristic time scale for biomass growth is very slow and is on the order of several hours or even days. The large difference of times scales makes the full coupling of all components impossible. However, even for photobioreactors operating at relatively high algal concentrations, the mass fraction of biomass in the reactor is very low (<1%), and the Stokes number of algal cells is less than 1, which means that it can be assumed that algal cells follow streamlines without affecting the flow field. Consequently, flow hydrodynamics and algal growth rate models only require one-way coupling. Furthermore, light distribution in the reactor reaches steady-state nearly instantaneously, and therefore the radiative transport equations can be solved independently from flow hydrodynamics or algal growth models for any given biomass concentration.

During the past decades, several comprehensive models have been proposed. According to the coupling method of flow hydrodynamics model and algae growth rate model, comprehensive model can be divided into four categories, circulation cell approach, compartment approach, Lagrangian approach and Eulerian approach.

### 2.4.1. Circulation time approach

To estimate the algae cell trajectory in a bubble column, Wu and Merchuk, (2002) assumed that the cell radial position is a cosine function of time using the circulation cell model by Joshi and Sharma (1979):

$$r = \frac{R}{2} \left(1 - \cos \frac{2\pi}{T} t\right) \quad (2.41)$$

Where  $R$  is the column radius.  $T$  is the circulation time, which can be obtained from the surface renewal model proposed by Danckwerts (1951). This equation was coupled with the Beer-Lambert law to obtain the cell light history. Later, Wu and Merchuk, (2004) applied the circulation time approach to simulate the algae growth in an internal loop airlift reactor. The resistant time and algae growth rate in the each region, the riser, the downcomer and the separator was calculated separately. Although satisfactory results were obtained for most of the conditions when compared the results with experiments, the definition of circulation time or resistant time is physically unrealistic and difficult to estimate in a reactor with complex flow dynamics.

### 2.4.2. Lagrangian approach

Obtaining light history by experiment or Lagrangian method of tracking cells is more straightforward than the circulation time method and can incorporate into photosynthetic model directly. Luo and Al-Dahhan (2004) developed a model integrating radiation distribution, growth kinetics and cell trajectories in an airlift photobioreactor. The microalgae particle trajectory for a long time (24h) was obtained by the computer automated radioactive particle tracking (CARPT) technology. The limitation of this technology is that only one

particle trajectory can be tracked and the tracking time should be sufficiently long in order to get a statically independent trajectory. Also, at present, this method is not used by other groups. Lagrangian particle tracking method is now widely used to obtain the particle trajectory (Pruvost et al., 2002a; 2002b; Marshall and Sala, 2011; Huang et al., 2015; Olivieri et al., 2015). Gao et al. (2016b) proposed a comprehensive model coupling hydrodynamics, light transport and algae growth rate model in a Taylor-Couette photobioreactor using Lagrangian approach. The schematic diagram of multi-timescale coupling method for Lagrangian approach is shown in Figure 2.3a. The overall strategy is (1) performing three-phase Eulerian-Eulerian-Lagrangian simulations in order to obtain particle trajectory, (2) computing light distribution using and fit light distribution as a function of biomass concentration and position, (3) solve the PSU model and compute the biomass concentration.

### 2.4.3. Compartment approach

The compartment approach can be seen as a trade-off between ideal mixing and full CFD models. Papáček et al., (2007) proposed a multicompartment/CFD approach to model the transport and reaction processes in a Taylor-Couette reactor. The reactor was divided into a network of well mixed compartments. The flow rates between adjacent compartments are derived from several thousand predicted trajectories (Lagrangian particle tracking). The mathematical description of the compartment approach is as follows:

$$V^j \frac{dx_i^j}{dt} = \left[ \sum_{k=1}^{n^j} (x_i^k f^{kj} - x_i^j f^{jk}) S^{jk} \right] + V^j R_{x_i^j}^j, \quad i=1, 2 \text{ or } 3, \quad j=1, 2, \dots, n_{x_i} \quad (2.42)$$

Where  $x_i^j$  is the state fraction  $i$  in  $j$ -th compartment,  $V^j$  is the volume of  $j$ -th compartment,  $s^{jk}$  is the common surface between  $j$ -th and the  $k$ -th compartment,  $f^{jk}$  is the flow rates per unit area from  $j$ -th and the  $k$ -th compartment,  $n^j$  is the total number of neighbor compartments to the  $j$ -th compartment,  $n_{x_i}$  is the total number of compartments,  $R_{x_i}^j$  is the reaction rate of state  $i$  corresponding to  $j$ -th compartment. While this model was not validated by coupling real growth kinetics and comparing with experimental data.

Nauha and Alopaeus (2013) also proposed a compartmental modeling method to integrate fluid dynamics and algae growth in a bubble column reactor. The liquid flow rates between two compartments are used to calculate the  $f^{jk}$  in Eq. (2.42). The compartment method can be seen as coarse-grid simulation, the effect of compartment size on the algae growth rate is not reported in their work. Actually, grid for fluid dynamics should be refined when coupling the growth rate model as light radial distribution has greater gradient than fluid dynamics distribution (such as velocity and gas volume fraction).

#### **2.4.4. Eulerian approach**

Papáček et al., (2011; 2014) proposed an Eulerian method to include the effect of fluid dynamics directly in photosynthetic model. They revised the PSU-based photosynthetic model into the form of transport equations by adding convective and diffusion term to the original model. They qualitatively studied the effect of mixing on algae growth rate in a Taylor-Couette reactor with a 1D model. While this model was not validated by coupling real growth kinetics and comparing with experimental data. However, the Eulerian method

provides a way for full coupling of growth rate model with fluid hydrodynamics and light. Gao et al., (2016) proposed a comprehensive model coupling hydrodynamics, light transport and algae growth rate model in a Taylor-Couette photobioreactor using Eulerian approach. The PSU model by Eilers and Peters model (1988) was rewritten in the form of transport equations by adding the convective and diffusion terms, and shows as follows:

$$\frac{\partial}{\partial t}(\alpha_s \rho_s x_i) + \nabla \cdot (\alpha_s \rho_s \vec{u}_s x_i) = -\nabla \cdot (\alpha_s \rho_s D_{s,e} \nabla x_i) + \alpha_s \rho_s R_{x_i}, \quad i=1,2,3 \quad (2.43)$$

Where  $R_{x_i}$  is the reaction rate of state  $i$ ,  $D_{s,eff}$  is the effective turbulent diffusivity of solid phase, and it can be expressed as

$$D_{s,eff} = D_{s,L} + \frac{\mu_t}{\rho_s Sc_t} \quad (2.44)$$

Where  $D_{s,L}$  is the laminar diffusivity of solid,  $Sc_t$  is the turbulent Schmitt number. The schematic diagram of multi-timescale coupling method for Eulerian approach is shown in Figure 2.3b. The overall strategy is (1) performing three-phase CFD simulations in order to compute velocity fields and turbulent diffusion coefficient distribution, (2) computing light distribution and fit light distribution as a function of biomass concentration and radial position, (3) computing the solve the PSU model and compute the biomass concentration

Table 2.2. Comprehensive coupling and simulation of PBRs.

Authors	Reactor type	Algae species	Phase s	Fluid dynamics	Light	Growth model	Coupling approach
Wu and Merchuk, 2002	Bubble column	Porphyridium sp.	NA	Multi-circulation cell model	B-L	Wu and Merchuk (2001)	Circulation time approach
Pruvost et al., 2002	Annular column	Porphyridium purpureum	L-S	Eulerian-Lagrangian	B-L	PI curve (Muller-Feuga, 1998)	Lagrangian approach

Table 2.2. Continued

Luo et al., 2004	Bubble column, Split column, Airlift	Porphyridium sp.	NA	CARPT	B-L	Wu and Merchuk (2001)	Lagrangian approach
Wu and Merchuk, 2004	Internal loop airlift	Porphyridium sp.	NA	Circulation cell model	B-L	Wu and Merchuk (2001)	Circulation time approach
Papáček et al., 2007	Taylor-Couette	Porphyridium sp.	L	Eulerian	B-L	Wu and Merchuk (2001)	Compartment approach
Sato et al., 2010	Virtual	Chaetoceros calcitrans	L-G-S	Eulerian-Eulerian-Lagrangian	B-L	Yoshimoto et al.	Lagrangian approach
Luo et al., 2012	Airlift column	Porphyridium sp.	L-G-S	Eulerian-Eulerian-Lagrangian	B-L	Wu and Merchuk (2001)	Lagrangian approach
Nauha and Alopaeus, 2013	Bubble column	Porphyridium sp.	L-G	Eulerian-Eulerian	B-L	Wu and Merchuk (2001)	Compartment approach
Nauha and Alopaeus, 2015	Bubble column	<i>P. tricornutum</i>	L-G	Eulerian-Eulerian	B-L	Wu and Merchuk (2001)	Compartment approach
Papáček et al., 2015	Taylor-Couette	Porphyridium sp.	L	Eulerian	B-L	Wu and Merchuk (2001)	Eulerian approach
Olivieri et al., 2015	Flat, tubular, bubble column, airlift	Porphyridium sp.	L-S	Eulerian-Lagrangian	B-L	Wu and Merchuk (2001)	Lagrangian approach
Gao et al., 2016	Taylor-Couette	<i>Chlorella vulgaris</i>	L-G-S	Eulerian-Eulerian-Lagrangian	RTE	Wu and Merchuk (2001)	Lagrangian approach
Gao et al., 2016	Taylor-Couette	<i>Chlorella vulgaris</i>	L-G-S	Eulerian-Eulerian-Eulerian	RTE	Wu and Merchuk (2001)	Eulerian approach

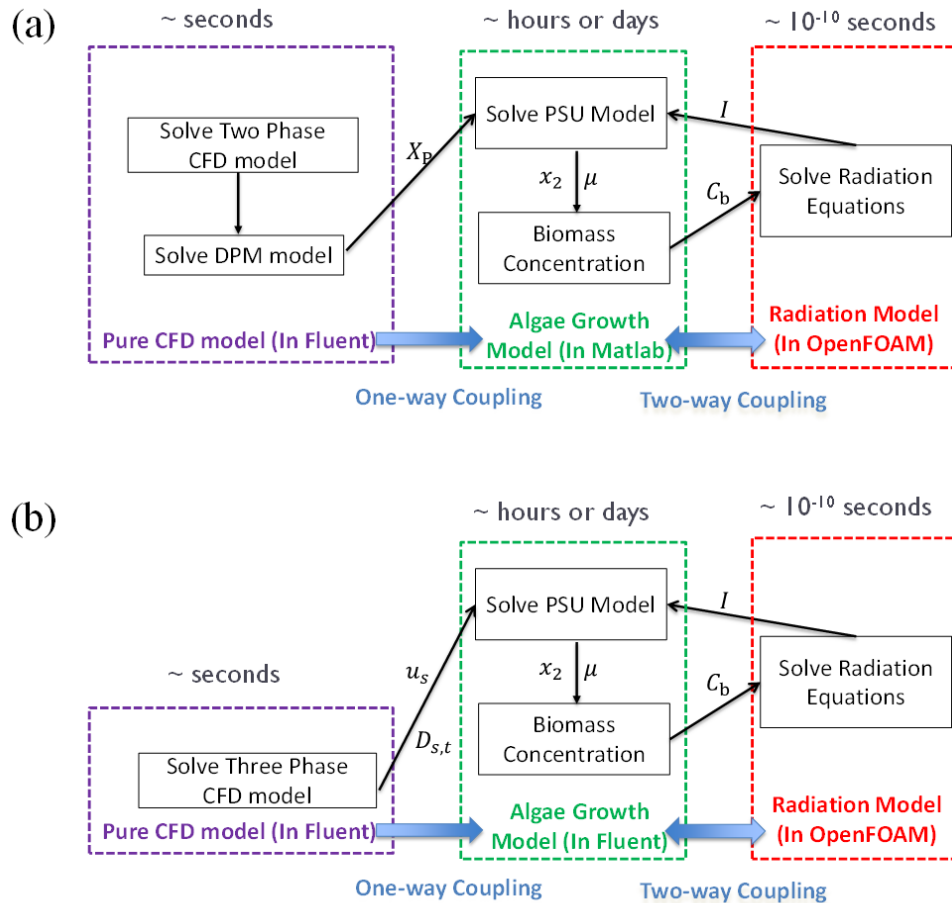


Figure 2.2. The schematic diagram of multi-timescale coupling method for (a) Lagrangian approach and (b) Eulerian approach.

## 2.5. Summary

This article reviews the state-of-the-art comprehensive modeling of the photobioreactor for microalgae biomass production. Although great progress has been made over the past decade, there is still a need for significant contributions in algae biotechnology development using computational techniques, such as to reduce cost and increase efficiency in large-scale biomass production. This requires the use of mathematical models to quantitatively understand the hydrodynamics, mass transfer, radiation transport, microalgae growth model

and their coupling within the photobioreactors. Below we provide a summary of recommendations as evident from the literature review of individual modeling parts.

Multiphase CFD simulation has been widely used to design and optimize reactors by studying the flow hydrodynamics, mass transfer, and algae cell trajectory or movement. The Eulerian-Eulerian RANS model with eddy viscosity turbulence model (such as  $k-\epsilon$  and  $k-\omega$ ) is most suitable for the gas-liquid flow and mass transfer studying in photobioreactor because it requires relatively less computational resource and it is suitable for large-scale systems simulation. To describe the algae cell motion, the Lagrangian particle tracking model coupled with the liquid (and gas) CFD model has been employed by integrating the force balance on it.

Beer-Lambert law is commonly used to describe the light distribution in photobioreactor when the biomass concentration is not high since it only considers cell absorption while neglects scattering. At high biomass concentration, two-flux approximation can be used. However, for realistic geometries involving curved reactor walls or complex illumination strategy, solving radiation transport equation is needed.

For microalgae growth simulation, most biological models that focus on the concepts of photosynthetic units (PSUs), which are called PSU models and are friendly for simulating and optimizing industrial cultivation systems due to their ability to incorporate the effects of light gradients and light/dark exposure cycles. These models assume the PSUs exist in various states and transits between each other to model photosynthesis, photoinhibition, and photoacclimation.

The comprehensive models can be divided into four categories, circulation cell approach, compartment approach, Lagrangian approach and Eulerian approach. In the widely used Lagrangian approach, the light history of algal cells obtained from Lagrangian particle tracking methods was embedded into the algae growth model to predict biomass growth rate. In the Eulerian approach, the convective and diffusive terms were added into the original algal growth model, in order to include the effect of fluid hydrodynamics directly. It is found that the Eulerian approach has better predictive capability while also requiring significantly less computational resource than the commonly used Lagrangian approach.

### **CHAPTER 3. CFD INVESTIGATION OF BUBBLE EFFECTS ON TAYLOR-COUPETTE FLOW PATTERNS IN THE WEAKLY TURBULENT REGIME**

Modified from the paper “Gao X, Kong B, Vigil RD. 2015. CFD investigation of bubble effects on Taylor-Couette flow patterns in the weakly turbulent vortex regime. Chem Eng J 270: 508-518.”

The effect of gas bubbles on Taylor–Couette flow patterns in the transition from laminar to weakly turbulent vortex flow is investigated by quasi-2D and 3D CFD simulation. The CFD model is based on the Eulerian–Eulerian two-fluid approach with constitutive closures for inter-phase forces and liquid turbulence and validated by comparison with previously published experimental data. The bubble spatial distribution patterns and the mechanism by which the dispersed fluid obtains a non-uniform radial distribution is discussed and the relative importance of various inter-phase forces is demonstrated. In addition, the experimental observation of vortex axial wavelength expansion due to the presence of bubbles was reproduced by the CFD simulations, and a two fluid Taylor–Couette flow regime map based on three observed regimes was constructed. Lastly, the influence of the azimuthal Reynolds number and gas superficial velocity on vortex wavelength, liquid velocity, mass transfer and turbulence are discussed in detail.

### 3.1. Introduction

Semi-batch gas-liquid Taylor-Couette flow (continuous feed of gas, no feed of liquid) has gathered attention not only as a canonical system for understanding micro-bubble assisted turbulent drag reduction, but also because of potential applications to a variety of chemical and biotechnological problems. For example, gas-liquid Taylor vortex flow has recently been used to speed the culture of microalgae (Kong et al., 2013; Kong and Vigil, 2013). Although hydrodynamic instabilities and flow patterns that arise in single-phase Taylor-Couette flow are well known and largely well understood, the introduction of even a very small volume fraction of gas into a liquid Taylor-Couette flow device can lead to substantial changes in fluid flow patterns (Gao et al., 2015d). For example, in a Taylor vortex flow device with its main axis oriented vertically, under some conditions gas bubble migration to the rotating inner cylinder surface produces drastic decreases in the torque required to spin the cylinder, and may also influence interphase mass transfer rates (Ramezani et al., 2015). Similarly, it is known that the strength of the axial gas flow relative to the inner cylinder rotation speed significantly impacts the vortex structure and can even disrupt them altogether. As a result, gas-liquid Taylor-Couette flow is much more complicated than single phase flow and is not nearly as well explored. Consequently, it is necessary to develop a better understanding of these phenomena with the assistance of both quantitatively accurate computational tools and experiments that can elucidate the mechanisms of mutual interaction between gas bubbles and the liquid flow structure.

A general schematic view of a Taylor-Couette device is shown in Fig. 3.1. When the outer cylinder is fixed, and for a specific reactor geometry (cylinder radii and length), single-phase flow can be characterized by the azimuthal Reynolds number,

$$Re_{\theta} = \frac{\omega_i r_i (r_o - r_i)}{\nu} \quad (3.1)$$

where  $\omega_i$  is the inner cylinder angular velocity,  $\nu$  is the fluid kinematic viscosity, and  $r_i$  and  $r_o$  are the inner and outer cylinder radii, respectively. With increasing  $Re$  number (and depending upon the ratio of the inner and outer cylinder radii), several well-known distinct flow regimes are attained as the flow undergoes transition to turbulence (Andereck et al., 1986).

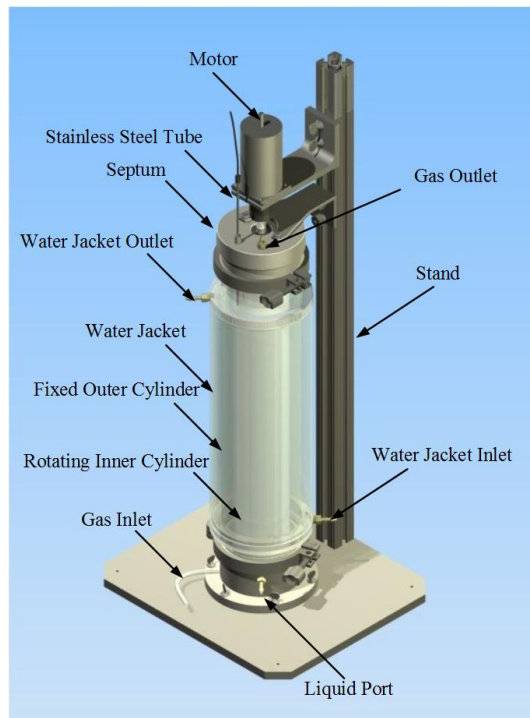


Figure 3.1. General schematic view of the Taylor–Couette flow system.

For the general case of immiscible two-fluid two-phase flow, the flow regime is not uniquely determined by the azimuthal Reynolds number and reactor geometry, but it also

depends upon other factors such as the axial Reynolds number, reactor orientation, interfacial surface tension, bubble size, fluid properties, etc (Sathe et al., 2010; Vedantam and Joshi et al., 2006; Vedantam et al., 2006; Joseph et al., 1984; Renardy et al., 1985; Joseph and Preziosi, 1987; Joseph et al., 1990; Zhu and Vigil, 2001; Zhu et al., 2000; Campero and Vigil, 1997; 1999; Baier and Graham, 2000a;2000b; Baier et al, 1999; 2000). For the specific case of vertically oriented semi-batch gas-liquid Taylor-Couette flow, we are aware of fifteen experimental (Shiomi et al., 1993; Djéridi et al., 1999; Atkhen et al., 2000; Djéridi et al., 2004; van den Berg et al., 2005; 2007; Murai et al., 2005; 2008; Mehel et al., 2006; 2007; Yoshida et al., 2009; van Gils et al., 2013; Fokoua and Gabillet, 2013; Watamura et al., 2013; Maryami et al., 2014) and four numerical investigations (Shiomi et al., 2000; Climent et al., 2007; Sugiyama et al., 2008; Chouippe et al., 2014) that have been published, as summarized in Table 3.1. Notice that a wide range of conditions have been studied including different reactor geometries (radius ratio  $\eta = r_i / r_o$  and aspect ratio  $\Gamma = (r_o - r_i) / L$  where  $L$  is the cylinder length), average bubble diameters  $d_b$ , and azimuthal Reynolds numbers. Whereas most of these studies are concerned primarily with inner cylinder drag reduction, several significant findings concerning the impact of bubbles on Taylor vortex flow patterns have been reported.

For example, Murai and coworkers observed that the axial wavelength of Taylor vortices is elongated by the presence of bubbles (Murai et al., 2005; 2008). Recently, they also reported that microbubbles ( $60 \mu\text{m}$ ) have a significant impact on wavy and modulated wavy vortex flow including intensification of the azimuthal wave amplitude, attenuation of wave modulation, and reduction of the azimuthal velocity gradient (Watamura et al., 2013).

Djéridi et al. (1999) studied the spatial distribution of bubbles for ventilated flow in the wavy vortex regime and they reported no significant effect of the bubbles on Taylor vortices. Later, Djéridi et al. (2004) reported that for low azimuthal Reynolds numbers, bubbles are trapped in Taylor vortex cores, whereas for larger Reynolds numbers bubbles migrate to vortex outflow boundaries and the axial wavelength of the vortices increases significantly. Mehel et al. (2006; 2007) considered bubble effects on flow structure in the weakly turbulent vortex regime, and they argued that the presence of bubbles near the inner cylinder increases wall shear stress, which in turn leads to the increase in Taylor vortex axial wavelength that has been observed in ventilated flow and stratified cavitating flow. In the highly turbulent vortex regime, van Gils and coworkers measured the local liquid velocity and local bubble statistics including the gas concentration profile, the bubble diameter and the bubble distribution and they found that bubbles mostly accumulate near the inner wall (van Gils et al., 2013).

Table 3.1. Summary of experimental and numerical work on bubbly Taylor-Couette flow in recent years.

Authors	Exp./Sim.	S-B/Cont. <sup>a</sup>	$\eta$	$\Gamma$	$\alpha_{g,global}$	$d_b$ (mm)	$Re_b$	$Re_\theta$	Flow Regime <sup>b</sup>
Shiomi et al. (1993)	Exp.	Cont.	0.9	100	NA	2-3	0-19	$0-8 \times 10^4$	TTVF
Djéridi et al. (1999)	Exp.	S-B	0.857	22	NA	0.1	NA	0-400	WVF
Atkhen et al. (2000)	Exp.	Cont.	0.88, 0.94	80, 40	NA	NA	NA	$2 \times 10^4$ - $2 \times 10^5$	TTVF
Djéridi et al. (2004)	Exp.	S-B	0.857	20-22	NA	NA	NA	250-2000	TVF, WVF, MWVF
van den Berg et al. (2005;2007)	Exp.	S-B	0.727	11.5	0-8%	0.5-2	NA	$7 \times 10^4$ - $1 \times 10^6$	TTVF, TF
Murai et al. (2005;2008)	Exp.	S-B	0.833	20	0-1%	0.5-0.6	0-0.04	600-4500	WVF, MWVF, TTVF
Mehel et al. (2006;2007)	Exp.	S-B	0.91	44.3	0-0.6%	0.6, 3	NA	2400-3800	TTVF

Table 3.1. Continued

Yoshida et al. (2009)	Exp.	S-B	0.833	32.5	NA	0.6	0-0.02	600-4500	WVF, MWVF, TTVF
van Gils et al. (2013)	Exp.	S-B	0.716	11.68	0-3%	0.9-1.2	0-11	$5.1 \times 10^5$ - $1 \times 10^6$	TTVF, TF
Fokoua et al. (2013)	Exp.	S-B	0.91	44.3	0-1.2%	1-2.4	NA	400-20000	WVF, WWVF, TTVF
Watamura et al. (2013)	Exp.	S-B	0.905	19.9	0-0.0012%	0.06	NA	269-1210	WVF, MWVF
Maryami et al. (2014)	Exp.	Cont.	0.857	10	0-10.33%	0.8-1.5	0-32.35	$5 \times 10^3$ - $7 \times 10^4$	TTVF
Shiomi et al. (2000)	Sim. (E-E)	Cont.	0.9	100	NA	2-3	0-19	$0-8 \times 10^4$	TTVF
Climent et al. (2007)	Sim. (E-L)	NA	0.889	2	NA	0.1	NA	0-167	TVF, WVF
Sugiyama et al. (2008)	Sim. (E-L)	NA	0.833	8	0-0.67%	0.5-0.6	0-0.04	600-2500	WVF, WWVF, TTVF
Chouippe et al. (2014)	Sim. (E-L)	NA	0.5, 0.72, 0.91	2.09, 3.08	NA	NA	NA	3000-8000	TTVF

<sup>a</sup>Continuous feed of gas but no feed of liquid (Semi-batch), Continuous feed of gas and liquid (Continuous)

<sup>b</sup>Taylor Vortex Flow (TVF), Wavy Vortex Flow (WVF), Modulated Wavy Vortex Flow (MWVF), Turbulent Taylor Vortex Flow (TTVF) and Turbulent Flow (TF)

As can be seen from Table 3.1, even fewer computational studies of gas-liquid Taylor vortex flow have been reported. In order to reduce computational cost, most of this simulation work was performed for only a small portion of the reactor and by using an Eulerian-Lagrangian approach whereby only one-way coupling (no force exerted by gas on the liquid) between phases is considered. Because only a portion of the annular flow region is simulated, the use of axial periodic boundaries is required in order to eliminate end effects and the vortex axial wavelength is not determined by any physical length scale, such as reactor length, but instead will be sensitive to the selected axial length to be simulated. For example, Sugiyama et al. (2008) investigated the effect of microbubbles on wavy vortex flow and found that the main effect of microbubbles is to create a local perturbation of the flow

that is able to break the coherent and mainly dissipative vortical structures of the flow. Climent et al. (2007) investigated the migration of bubbles in the Taylor vortex and wavy vortex regime and found that bubbles preferentially accumulate in low-pressure regions of the flow field. More recently, these investigators considered the mechanism of bubble dispersion in turbulent Taylor-Couette flow and they observed that patterns of bubble accumulation depend on bubble size (Chouippe et al., 2014). Similarly, Shiomi et al. (2000) performed simulations for gas-liquid two phase Taylor-Couette flow in the high-Re number regime, and their predictions that bubbles concentrate at vortex outflow boundaries are in qualitative agreement with their experimental results.

The aim of this study is to elucidate the role of bubbles on semi-batch gas-liquid Taylor-Couette flow patterns by using an Eulerian-Eulerian two-fluid CFD approach. Hence, the effects of two-way coupling between the gas and liquid phases are accounted for explicitly. In addition, the computational domain of the simulations includes the entire reactor length so that no assumption of axial periodicity is required. The remainder of this report is organized as follows. First, the two-fluid Eulerian-Eulerian CFD model is developed for gas-liquid bubbly Taylor-Couette flow. Second, simulation predictions are compared with previously published experimental data to validate the CFD model. Third, the mechanisms leading to observed bubble distributions are discussed in detail. Lastly, the effect of bubbles on the liquid flow patterns is analyzed and discussed.

### 3.2. Two-fluid model for Taylor-Couette flow

#### 3.2.1. Governing equation and interphase forces

Both the mixture model and the two-fluid model can be used to simulate bubbly flow where the gas volume fraction remains low. However, the mixture model assumes that all phases share a momentum equation, and therefore it suffers from the disadvantage that comprehensive inter-phase momentum exchange cannot be considered. Because interphase forces exerted on bubbles play an important role in their spatial distribution, the Eulerian-Eulerian two-fluid model was used. The phase averaged two-fluid mass and momentum conservation equations describing this system can be expressed as:

$$\frac{\partial}{\partial t}(\alpha_k \rho_k) + \nabla \cdot (\alpha_k \rho_k \vec{u}_k) = 0 \quad (3.2)$$

$$\frac{\partial}{\partial t}(\alpha_k \rho_k \vec{u}_k) + \nabla \cdot (\alpha_k \rho_k \vec{u}_k \vec{u}_k) = -\alpha_k \nabla p + \nabla \cdot (\overline{\overline{\tau}}_k + \overline{\overline{\tau}}_k^{Re}) + \alpha_k \rho_k \vec{g} + \vec{F}_{lk} \quad (3.3)$$

where subscript  $k$  refers to the liquid ( $k = l$ ) or bubble ( $k = g$ ) phase. Here,  $\alpha$  is the volume

fraction,  $\vec{u}$  is the phase time-averaged velocity,  $\overline{\overline{\tau}}$  and  $\overline{\overline{\tau}}^{Re}$  are phase stress and phase

Reynolds stress tensors, respectively.  $\vec{F}$  is the interphase momentum exchange term, which

can be decomposed into at least five independent forces (Gao et al., 2003):

$$\vec{F}_{lk} = \vec{F}_D + \vec{F}_L + \vec{F}_{VM} + \vec{F}_W + \vec{F}_T \quad (3.4)$$

These represent drag, lift, virtual mass, wall lubrication, and turbulent dispersion, respectively.

The drag force was expressed as (Gao et al., 2003)

$$\vec{F}_{Dg} = -\vec{F}_{Dl} = \frac{3}{4} \alpha_g \alpha_l \frac{\rho_l}{d_b} C_D \left| \vec{u}_g - \vec{u}_l \right| \left( \vec{u}_l - \vec{u}_g \right) \quad (3.5)$$

The Tomiyama et al. drag model (Tomiyama et al., 1998) is well suited to gas-liquid flows in which the bubbles may be deformed and have a range of shapes. The drag coefficient  $C_D$  used in the present work was determined from the following expression (Tomiyama et al., 1998),

$$C_D = \max\left(\min\left(\frac{24}{\text{Re}_b}(1+0.15\text{Re}_b^{0.687}), \frac{72}{\text{Re}_b}\right), \frac{8}{3} \frac{E_o}{E_o+4}\right) \quad (3.6)$$

Here, the Eötvös number and bubble Reynolds number are defined as

$$E_o = \frac{g(\rho_l - \rho_g)d_b^2}{\sigma} \text{ and } \text{Re}_b = d_b \left| \vec{u}_l - \vec{u}_g \right| \rho_l / \mu_l, \text{ respectively.}$$

The lift force is defined as (Drew and Lahey, 1993):

$$\vec{F}_{Lg} = -\vec{F}_{Ll} = -C_L \alpha_g \rho_l \left( \vec{u}_l - \vec{u}_g \right) \times (\nabla \times \vec{u}_l) \quad (3.7)$$

Where  $c_L$  is the lift force coefficient, which was taken to be 0.01 (Behzadi et al., 2004).

Virtual mass is significant when the secondary phase density is much smaller than the primary phase density as in the present case, and it is formulated as (Drew and Lahey, 1993):

$$\vec{F}_{VMg} = -\vec{F}_{VMl} = 0.5 \alpha_g \rho_l \left( \frac{d_l(\vec{u}_l)}{dt} - \frac{d_g(\vec{u}_g)}{dt} \right) \quad (3.8)$$

where

$$\frac{d_l(\vec{u}_l)}{dt} = \frac{\partial \vec{u}_l}{\partial t} + \vec{u}_l \cdot \nabla \vec{u}_l \quad (3.9)$$

$$\frac{d_g(\vec{u}_g)}{dt} = \frac{\partial \vec{u}_g}{\partial t} + \vec{u}_g \cdot \nabla \vec{u}_g \quad (3.10)$$

The lubrication wall force can be written as (Antal et al., 1991):

$$\vec{F}_{Wg} = -\vec{F}_{Wl} = \alpha_g \rho_l \left| \vec{u}_g - \vec{u}_l \right|^2 \max \left[ 0, \left( \frac{C_1}{d_b} + \frac{C_2}{y} \right) \right] \vec{n}_w \quad (3.11)$$

Where  $\vec{n}_w$  is the normal vector from the wall. Standard values for the lubrication force coefficients were used and given by  $c_1 = -0.01$  and  $c_2 = 0.1$ .

The turbulent dispersion force can be expressed as (Huang et al., 2010; Talvy et al., 2007):

$$\vec{F}_{Tg} = -\vec{F}_{Tl} = -\rho_l \overline{u'_g u'_l} \nabla \alpha_g \quad (3.12)$$

The covariance in the above equation is related to the turbulent kinetic energy of the liquid phase,  $\overline{u'_g u'_l} \approx 2k_l$ . See reference Talvy et al. (2007) for more details concerning derivation of Equation (3.12).

### 3.2.2. Turbulence modeling

Turbulence was simulated using the Reynolds stress model (RSM) as several authors have reported that this model yields the best results for simulation of single phase turbulent Taylor-Couette flow (Sathe et al., 2010; Vedantam et al., 2006; Wang et al., 2005). In this work only small values of the gas holdup ( $\alpha_g \leq 0.01$ ) are considered, and consequently turbulence is modeled only for the liquid phase. Hence, the transport equations for Reynolds stress,  $\overline{\rho u'_i u'_j}$  are given by:

$$\begin{aligned} \frac{\partial}{\partial t} (\alpha_l \rho_l \overline{u'_i u'_j}) + \frac{\partial}{\partial x_k} (\alpha_l \rho_l u_k \overline{u'_i u'_j}) = & \frac{\partial}{\partial x_k} [\alpha_l \rho_l \mu \frac{\partial}{\partial x_k} (\overline{u'_i u'_j})] + \frac{\partial}{\partial x_k} [\alpha_l \frac{\mu_t}{\sigma_k} \frac{\partial}{\partial x_k} (\overline{u'_i u'_j})] \\ & + P_{ij} + G_{ij} + \phi_{ij} + F_{ij} - \varepsilon_{ij} + \Pi_{Rij} \end{aligned} \quad (3.13)$$

and the turbulent kinetic energy is obtained from the trace of the Reynolds tensor:

$$k = \frac{1}{2} \overline{u'_i u'_i} \quad (3.14)$$

The scalar dissipation rate is similar to that used in the standard  $k - \varepsilon$  model:

$$\frac{\partial}{\partial t}(\alpha_l \rho_l \varepsilon) + \frac{\partial}{\partial x_i}(\alpha_l \rho_l \varepsilon u_i) = \frac{\partial}{\partial x_j} \left[ \alpha_l \left( \mu + \frac{\mu_t}{\sigma_\varepsilon} \right) \frac{\partial \varepsilon}{\partial x_j} \right] + \frac{1}{2} \alpha_l C_{\varepsilon 1} [P_{ij} + C_{\varepsilon 3} G_{ij}] \frac{\varepsilon}{k} - C_{\varepsilon 2} \alpha_l \rho_l \frac{\varepsilon^2}{k} + \alpha_l \rho_l \Pi_\varepsilon \quad (3.15)$$

and the turbulent viscosity  $\mu_t$  is computed as follows:

$$\mu_t = \rho_l C_\mu \frac{k^2}{\varepsilon} \quad (3.16)$$

### 3.2.3. Simulation conditions and strategy

The experiment conducted by Murai et al. (2005; 2008) was selected as a test case to validate our model for two-phase flow. They studied the bubble behavior in the Reynolds number range from 600 to 4500, which corresponds to the modulated wavy vortex regime and turbulent Taylor vortex regime for single phase flow, respectively. The flow parameters used for the simulations are identical with those used in the experimental work of Murai et al. (2005; 2008) and geometric parameters for this system are reported in Table 3.2. Murai et al. (2005) measured the local bubble size by particle image velocimetry and they reported an overall averaged bubble diameter of 0.6 mm for all cases. Thus an average bubble diameter of 0.6 mm was used in the simulation work presented here.

Both quasi-2D and 3D simulations were carried out and compared in this work. The quasi-2D simulations were assumed to be axisymmetric, and consequently the predictions include azimuthal velocity. A non-uniform 2D rectangular mesh was employed, and three different progressively finer mesh resolutions were tested until a grid-independent solution was obtained. The final grid had 30×400 (radial×axial) nodes. The maximal mesh size is 0.6mm×0.6mm, which is equal to the bubble diameter. Hence, the mesh is very fine for a

RANS model. In the single 3D simulation that was performed, no assumption regarding axisymmetry was invoked and a non-uniform cubic trapezoidal grid with  $30 \times 400 \times 150$  (radial $\times$ axial $\times$ azimuthal) nodes was used.

In the near-wall region (3mm), the grid was more narrowly spaced in order to more efficiently capture steep wall gradients. In the axial and azimuthal directions, the mesh grids are uniformly distributed. The typical maximal value of the wall coordinate  $r^+$  is 0.8 and 1.9 for 2D and 3D cases, respectively. The gas inlet was modeled as a narrow channel with a width of 2 mm near the inner wall, which is consistent with the experimental situation. The gas outflow boundary was taken to be equal to the cylinder gap width, which is also consistent with the experiments of Murai et al., (2005).

Table 3.2. Experimental conditions of Murai et al's experiment (at 298k)

$r_i$	60 mm	$\eta$	0.857
$r_o$	72 mm	$\rho_l$	915 kg/m <sup>3</sup>
$L$	240 mm	$\nu$	$5 \times 10^{-6}$ m <sup>2</sup> /s
$\Gamma$	20	$Re$	600-4500
$Q_{g,in}$	0-1.67ml/s	$d_b$	0.5-0.6 mm

The model formulated above was implemented into the commercial CFD code, ANSYS FLUENT 14.5 (Ansys Inc., US) with the help of user defined functions (UDFs) and solved using a finite volume method. Pressure-velocity coupling was resolved using the SIMPLE algorithm (Patankar, 1980). Transient CFD simulations were carried out using a time step of  $1 \times 10^{-4}$  s. The simulations were executed on a double eight core workstation (Dell precision T7600). It required four days to run a quasi-2D case with eight processors and 50 days to run

a 3D case with 30 processors. Because the mesh size of the 3D case (1.8 million) is much larger than the 2d case, the calculations require longer time as the simulation speed is limited by the available computational resources. For this reason, the standard  $k-\omega$  turbulence model with low-Re corrections and shear flow corrections was used in the 3D simulation instead of the much more computationally expensive Reynolds stress turbulence model. Thus, only a single 3D case ( $Q_g = 0.33$  ml/s,  $Re=2900$ ) was simulated in this work due to computational limitation. Time-averaged results were obtained by averaging over the final 30 seconds of simulated time, as it takes at least 50 seconds physical time to reach a quasi steady state.

Simulations were initialized assuming that only the liquid phase occupied the flow cell ( $\alpha_g = 0$ ). No-slip conditions and a scalable wall function were used at solid boundaries, and the azimuthal velocity of the inner wall was chosen to match experimental conditions. Boundary conditions at the inlet were set by prescribing a fixed gas velocity and by specifying an inlet bubble fraction of 0.01. Pressure outlet boundary conditions were used for both fluid phases.

### **3.3. Results and discussion**

#### **3.3.1. Bubble distribution patterns and mechanism**

Examples of the instantaneous spatial distribution of the gas phase obtained from quasi-2D simulations (after reaching steady state) are depicted in Fig. 3.2, which shows contour plots of the computed bubble phase volume fraction in the annulus for four Reynolds numbers in the range 600-3900. At  $Re = 600$ , the flow was laminar and therefore no

turbulence model was employed and the turbulent dispersion force was not included. For all higher azimuthal Reynolds numbers considered, turbulence modeling was operative. In all cases, gas was distributed preferentially near the inner cylinder wall. However, when  $Re = 600$  the bubbles simply rise vertically from inlet to outlet and do not form organized structures in the axial direction, as the rise velocity of bubbles ( $\approx 0.05$  m/s) is faster than the bubble azimuthal velocity ( $\approx 0.035$  m/s). In contrast, for  $Re \geq 1700$ , the bubble azimuthal velocity ( $\approx 0.07$  m/s) is greater than the rise velocity ( $\approx 0.03$  m/s) and organized bubble cloud structures form at periodic axial locations. The 3D simulation, which unlike the quasi-2D simulations does not assume axisymmetry, demonstrates that these rising bubbles form a spiral structure at the inner cylinder wall, as shown in Fig. 3.3. Comparison with velocity field calculations reveals that these locations correspond to Taylor vortex inflow boundaries (e.g. compare Fig. 3.2 and Fig. 3.8). Fig. 3.3 also shows that the gas volume fraction at the bottom of the reactor is lower than at the top, and this phenomenon can be explained by the fact that the inlet bubble volume fraction at the bottom of the reactor was specified to be 0.01.

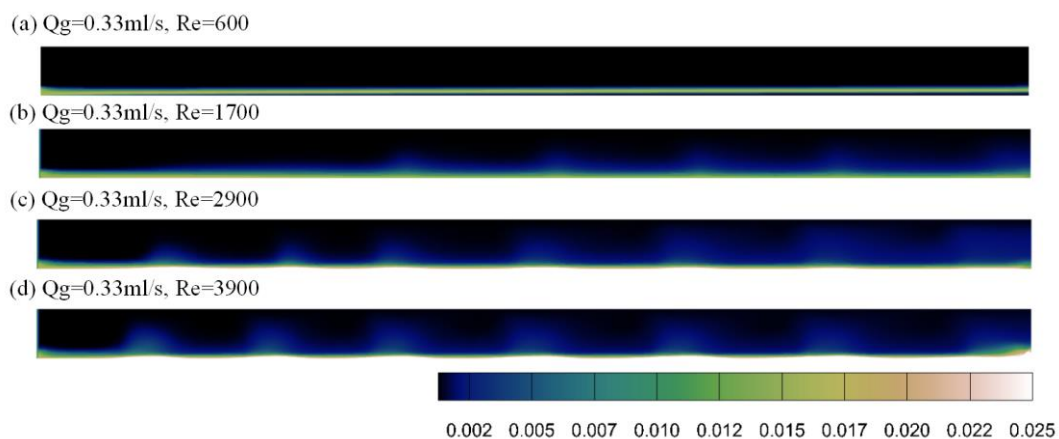


Figure 3.2. Computed bubble phase volume fraction contour plot in the annulus. The inner cylinder wall is shown on the bottom. The gas entrance is on the left side of the plot adjacent to the inner cylinder wall and the gas exits on the right side of the plot.

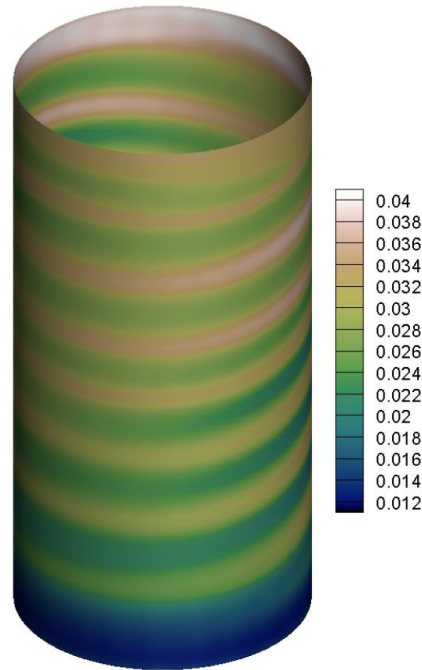


Figure 3.3. Computed bubble volume fraction contour plot on the inner wall by 3D.

The above results are in good agreement with experimental findings as can be seen in Fig. 3.4, which shows a comparison of the computed and experimental radial gas concentration profiles. For the test case at  $Re=600$ , the discrepancy between experimental data and simulation results may be a result of at least two causes. When the inlet gas flow rate is fixed, the global gas volume fraction of the reactor is expected to increase with the azimuthal  $Re$  number. In contrast, Murai's experiments seem to show that the global gas volume fraction for the case  $Re=600$  is larger than for the other cases at higher Reynolds numbers. This anomalous finding suggests that there may be significant experimental error for the case  $Re = 600$ . Secondly, as can be seen from the simulated gas volume fraction distribution in the 3D simulation, the gas volume fraction distribution is not axisymmetric, and therefore the spiral distribution of bubbles cannot be faithfully captured by quasi-2D simulation, which in turn leads to errors.

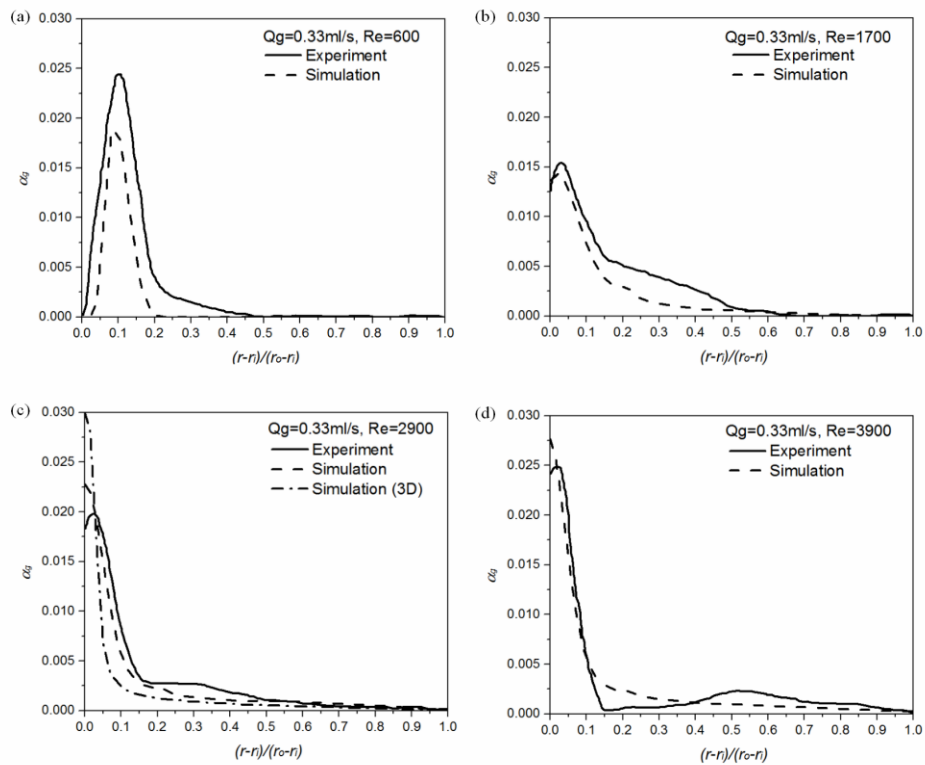


Figure 3.4. Comparison between numerical and experimental data of radial gas concentration profiles at different Reynolds number.

Comparison of simulated volume fraction by quasi-2D and 3D simulation at  $Re=2900$  is shown in Fig. 3.4c, where it can be seen that the 3D simulation predicts slightly larger gas volume fraction near the inner cylinder than does the quasi-2D simulation. Axially averaged radial gas volume fractions computed for higher gas flow rates are shown in Fig. 3.5. In all cases, the maximum gas volume fraction is located on the inner cylinder wall, but gas volume fraction in the bulk liquid increases with increasing inlet gas flow rate.

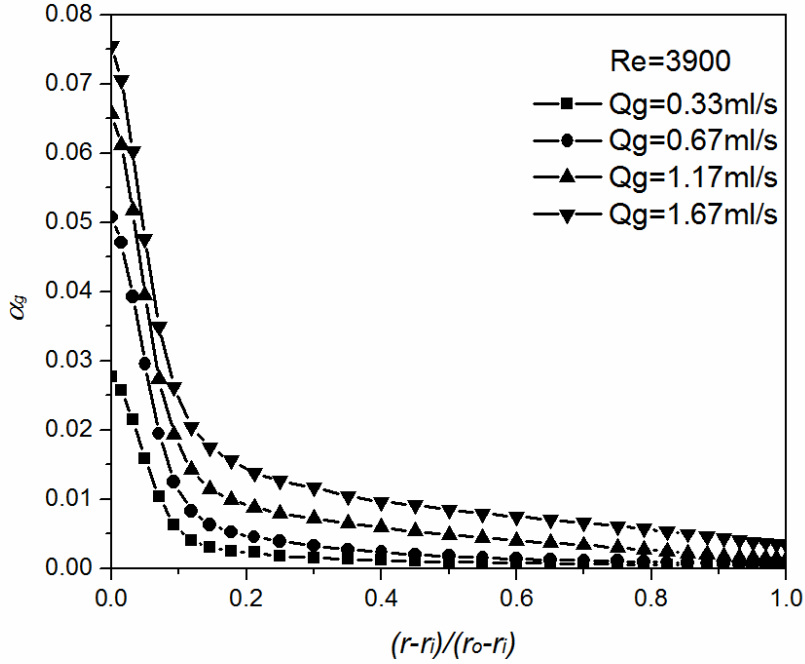


Figure 3.5. Simulated radial gas concentration at different gas flow rate.

In order to better understand the radial bubble distribution, the interphase forces acting on the bubbles were considered individually. In the fully developed region of a Taylor vortex reactor, the magnitudes of the azimuthal and radial velocities of both phases are almost the same, as can be seen in Fig. 3.12. At steady-state conditions, the radial component of the bubble phase momentum balance can be simplified as:

$$\begin{aligned}
 0 &= F_{Pr} + F_{Lr} + F_{Tr} + F_{Wr} \\
 &= -\alpha_g \frac{dp}{dr} - C_L \alpha_g \rho_l (u_{lz} - u_{gz}) \frac{du_{lz}}{dr} - 2\rho_l k_l \frac{d\alpha_g}{dr} + \alpha_g \rho_l (u_{gz} - u_{lz})^2 \max \left[ 0, \left( \frac{C_1}{d_b} + \frac{C_2}{y} \right) \right] \quad (3.17)
 \end{aligned}$$

The radial distribution of the radial component of each of these contributing forces (except for virtual mass, which is zero) are shown in Fig. 3.6. It is evident from these plots that in the laminar Taylor vortex flow regime ( $Re = 600$ ), radial non-uniformity is due to competition between the pressure gradient force and the wall lubrication force. In contrast,

for the turbulent regime ( $Re=1700-3900$ ) radial non-uniformity is mainly determined by competition between the pressure gradient force, the wall lubrication force and the turbulent dispersion force. With increasing values of  $Re$ , both the wall lubrication and lift forces become progressively negligible in comparison to the pressure and turbulent dispersion forces. Thus, the non-uniform phase distribution can be understood as a competition primarily between centrifugal force, which causes bubbles to migrate to the inner wall and turbulent velocity fluctuations that transport bubbles towards the middle of the annulus.

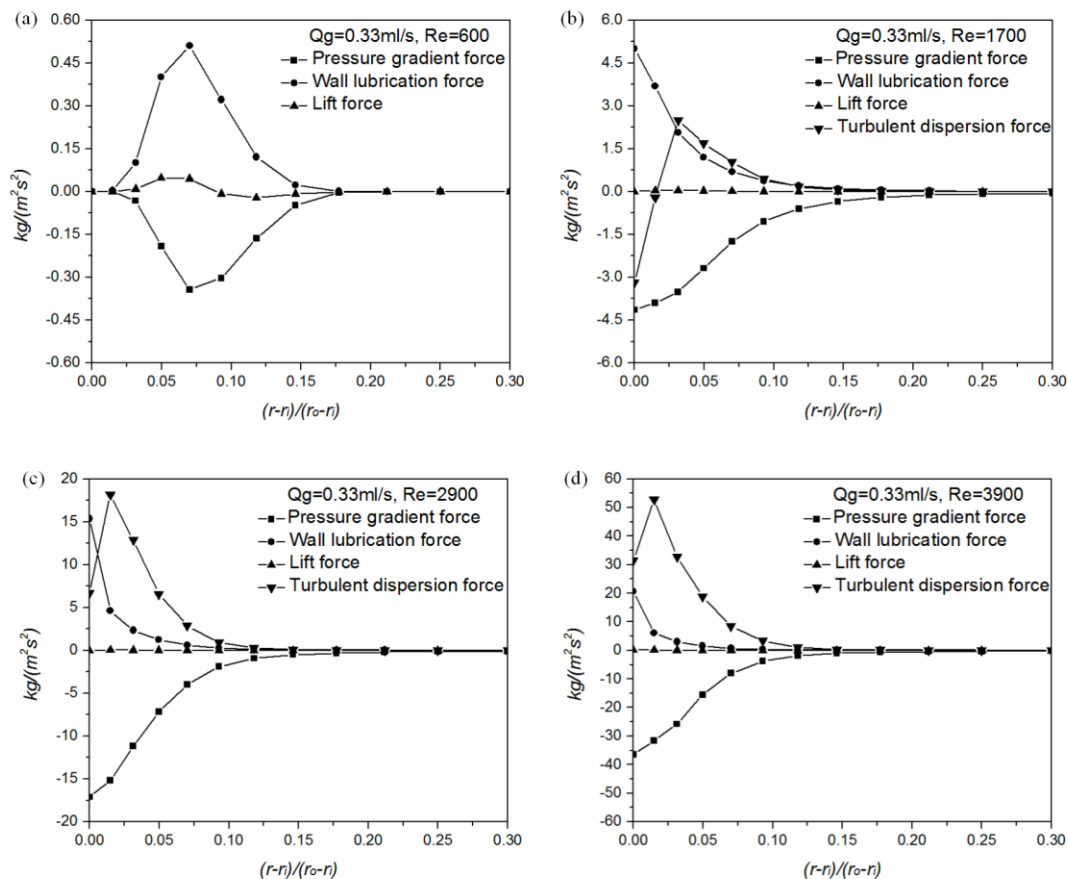


Figure 3.6. Radial profiles of interphase forces acting on the bubble phase at different Reynolds numbers.

### 3.3.2. Transition of Taylor vortex structure

Figs. 3.7 and 3.8 show contour plots of liquid phase stream function for single-phase (no gas feed) and two-phase simulations ( $Q_g = 0.33$  ml/s), respectively. It can be seen from Fig. 3.7 that in the single phase simulations the normalized axial wavelength  $\lambda/d$ , where  $d = r_o - r_i$ , is nearly constant and equal to 2, independent of the azimuthal Reynolds number. In contrast, the low cylinder rotation speed ( $Re = 600$ ) for the two phase case results in axial bubble velocities exceeding the azimuthal velocity and consequently complete disruption of Taylor vortices (Fig. 3.8a). At higher azimuthal Reynolds numbers, the swirl velocity becomes more dominant and Taylor vortices remain coherent despite the passage of gas bubbles in the axial direction. Comparing Figs. 3.7 and 3.8, it can also be seen that in the presence of bubbles, the vortex wavelength is elongated by approximately 45% compared to the corresponding single-phase case. As is the case for single-phase flow, the vortex wavelength during two-phase flow is independent of the azimuthal Reynolds number in the range 1700-3900. Differences in the predicted axial wavelength for the quasi-2D and 3D simulations will be discussed in the next section.

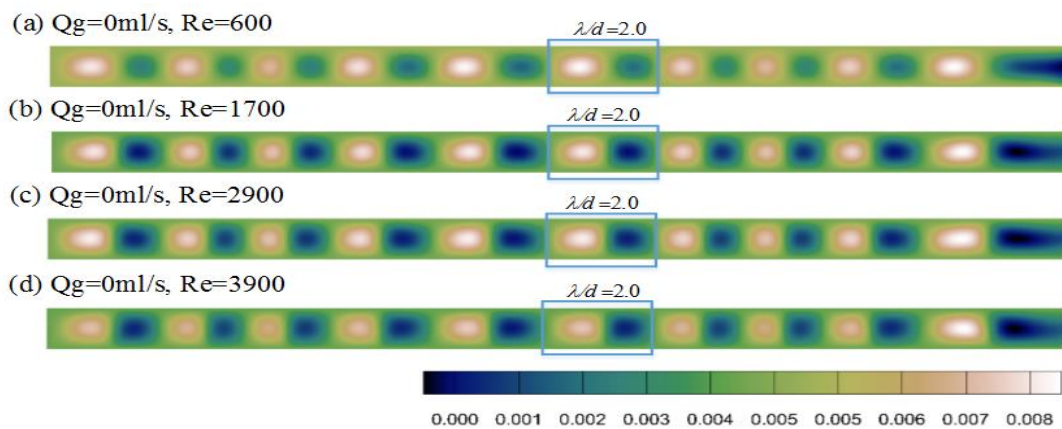


Figure 3.7. Stream function of the liquid phase in single-phase cases and effect of Reynolds number on the wavelength of Taylor vortices (kg/s).

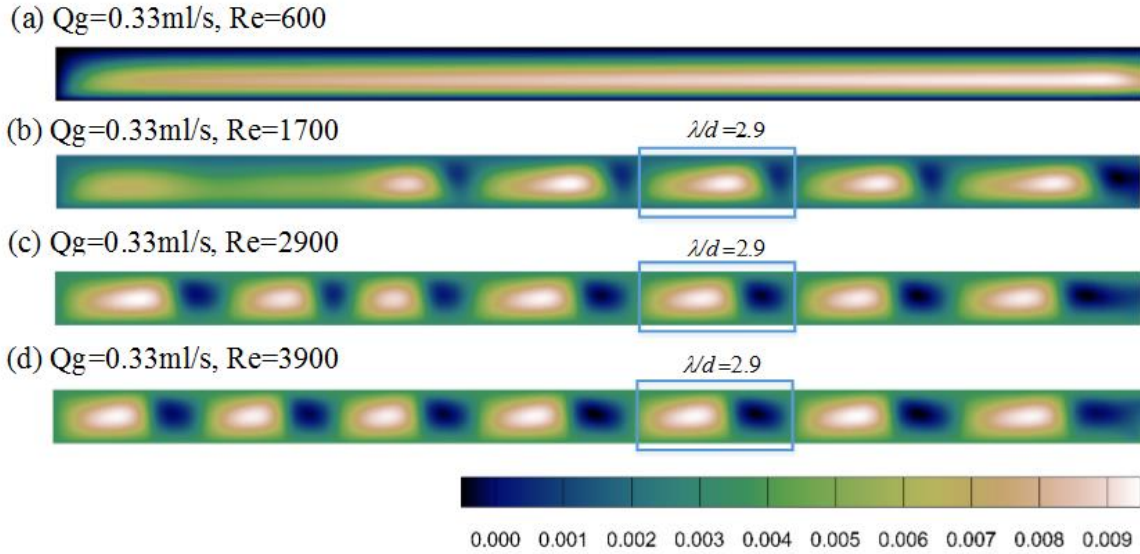


Figure 3.8. Stream function of the liquid phase in two-phase cases and effect of Reynolds number on the wavelength of Taylor vortices (kg/s).

The effect of gas flow rate on stream function and axial wavelength is depicted in Fig. 3.9. It is clear that for fixed azimuthal Reynolds number and increasing gas flow rate, the vortex wavelength becomes increasingly elongated until eventually Taylor vortices are destroyed altogether. Based upon these simulations, a flow regime map for the three observed patterns (annulus filled with vortices, partially filled with vortices, and no vortices) was constructed using the axial Reynolds number ( $Re_a = \rho_l U_g (r_o - r_i) / \mu_l$ , where  $U_g$  is superficial gas velocity) to characterize the strength of the axial gas flow and the azimuthal Reynolds number ( $Re_\theta$ , see Eq. (3.1)) as a representation of the robustness of the Taylor vortices, as shown in Fig. 3.10. The two boundaries of the three regimes are roughly determined by 34 simulation cases at different gas inlet flow rate and rotation speed. It can be concluded from this phase diagram that the existence and wavelength of Taylor vortices depends upon a competition between the azimuthal liquid flow and the axial gas flow. This result could

provide useful guidance for the design and optimization of semi-batch Taylor-Couette devices.

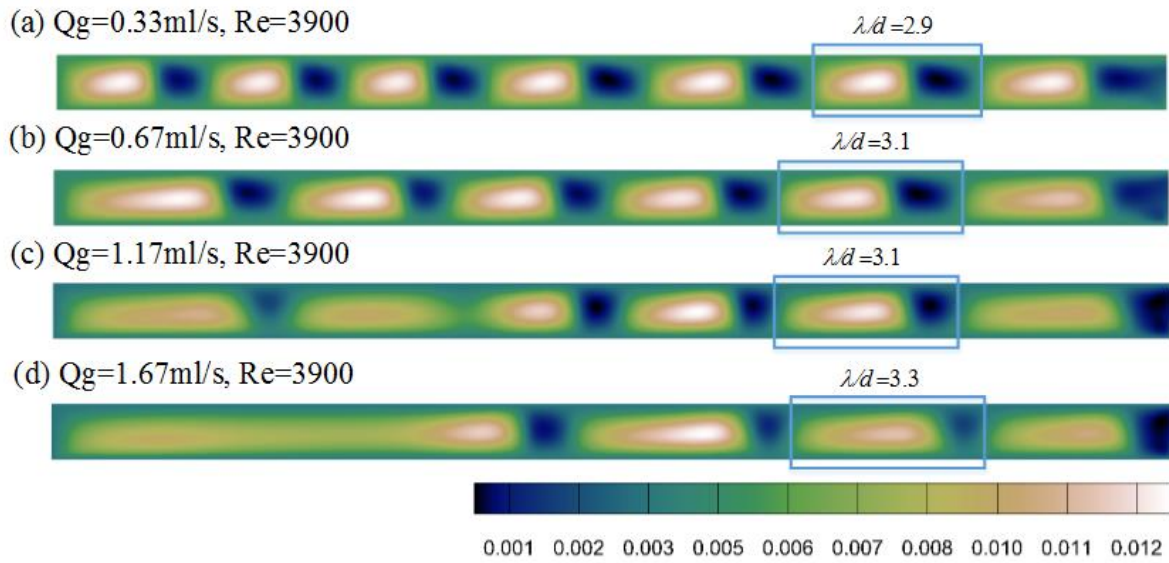


Figure 3.9. Stream function of the liquid phase in two-phase cases and effect of bubble

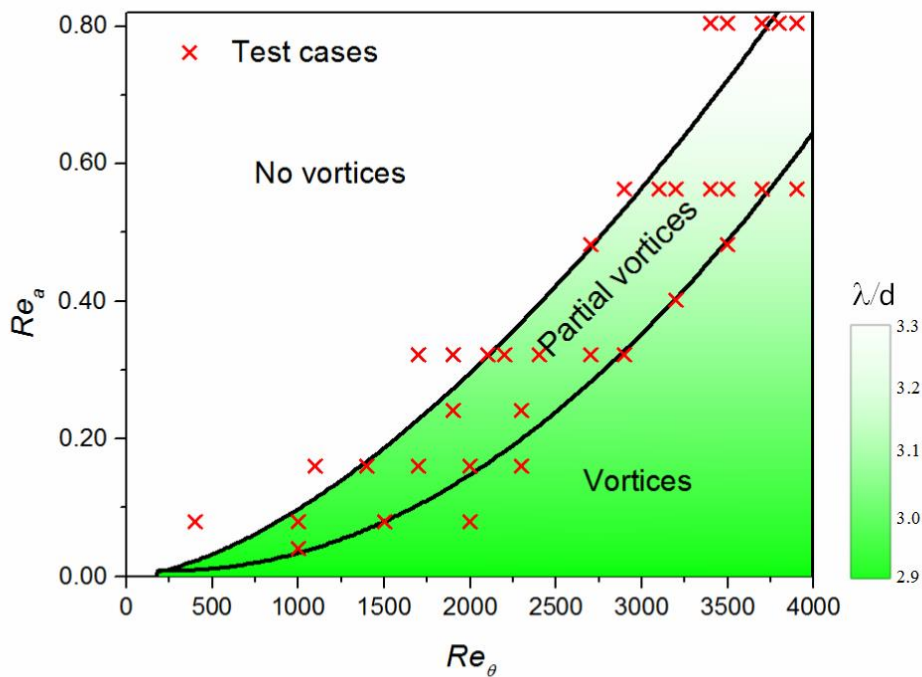


Figure 3.10. Flow regime map for bubble-liquid two phase Taylor-Couette flow.

### 3.3.3. Liquid hydrodynamics

Fig. 3.11 shows liquid axial, radial and azimuthal velocity contours for both the quasi-2D and 3D simulations. The results are in reasonably close agreement except that eight vortex pairs are observed in the 3D simulation whereas only seven vortex pairs appear in the quasi-2D simulation. A comparison of radial profiles for each velocity component for both the liquid and gas phases at a fixed gas flow rate and  $Re = 3900$  is shown in Fig. 3.12a. The azimuthal and radial velocity components for both phases are nearly identical, whereas due to the imposed axial gas flow, the axial gas velocity is significantly greater than the axial liquid velocity. One ramification of this observation is that for applications involving gas-liquid mass transfer, the mass transfer coefficient can be expected to be relatively insensitive to azimuthal Reynolds number, in comparison to the superficial gas velocity. Indeed, this prediction has recently been verified Ramezani et al., (2015).

Radial distributions of the liquid phase normal Reynolds stresses for single phase and two-phase flows are plotted in Fig. 3.12b for  $Re = 3900$ . Notice that although the magnitude of the azimuthal velocity component is dominant ( $\sim$  ten times greater than the axial and radial components) as is evident from Fig. 3.12a, all components of the normal Reynolds stress are of the same order. These results are consistent with those of Burin et al., who reported that velocity fluctuations for single-phase turbulent Taylor vortex flow are of the same order of magnitude for all three velocity components (Burin et al., 2010). A second interesting feature of Fig. 3.12b is that at small gas flow rate, the introduction of gas bubbles decreases the liquid normal Reynolds stress near the inner wall, compared to the single phase flow case, whereas the liquid normal Reynolds stresses increase near the outer wall relative to the single

phase case. In contrast, at large gas flow rates the introduction of bubbles increases the liquid normal Reynolds stress across the entire gap. In the highly turbulent flow regime, van Gils et al. also observed an increase in  $u'_\theta$  as compared to the case of single phase flow at radial locations  $(r-r_i)/(r_o-r_i) \leq 0.3$ , but a decrease in  $u'_\theta$  at radial location near the outer wall. However, because their experiments were performed in a different flow regime and inlet gas flow rate, the spatial distribution of bubbles is likely to be quite different. Thus, whether and how the local increase or decrease in velocity fluctuations is linked with the bubble distribution is still an open question and may be answered using other techniques, such as DNS simulation.

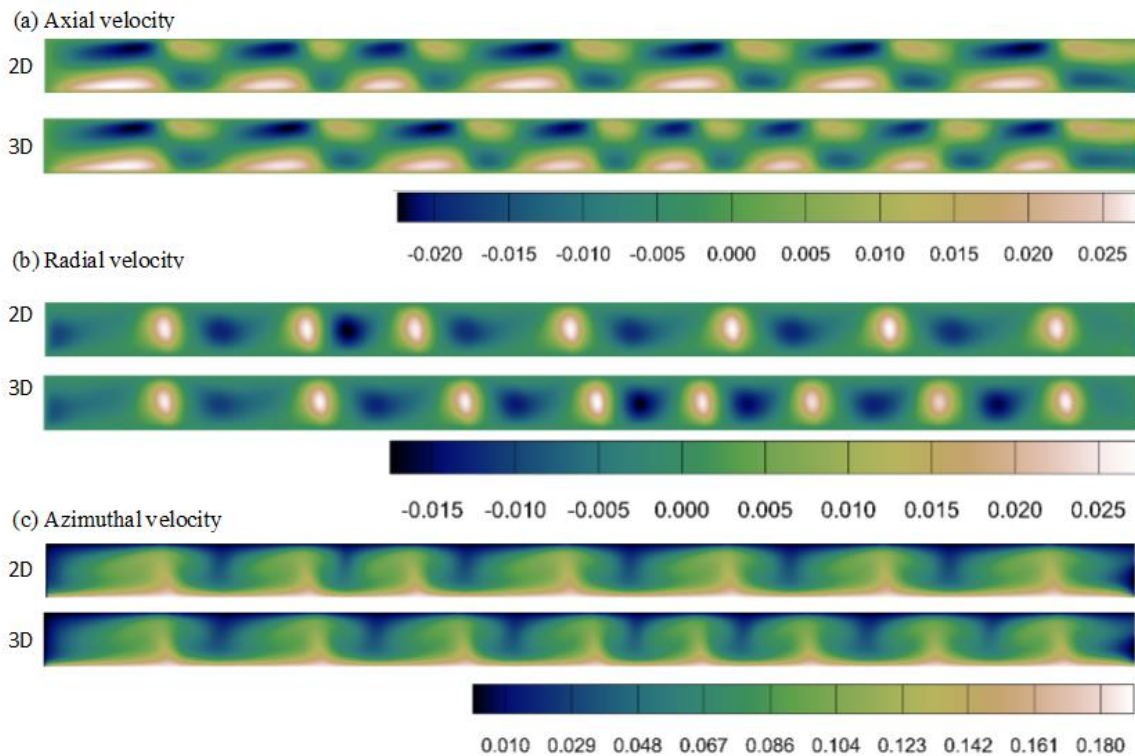


Figure 3.11. Comparison between simulated axial, radial and azimuthal liquid velocity in the annulus. The inner cylinder wall is shown on the bottom. The gas entrance is on the left side of the plot adjacent to the inner cylinder wall and the gas exits on the right side of the plot.

( $Q_g = 0.33$  ml/s,  $Re = 2900$ ).

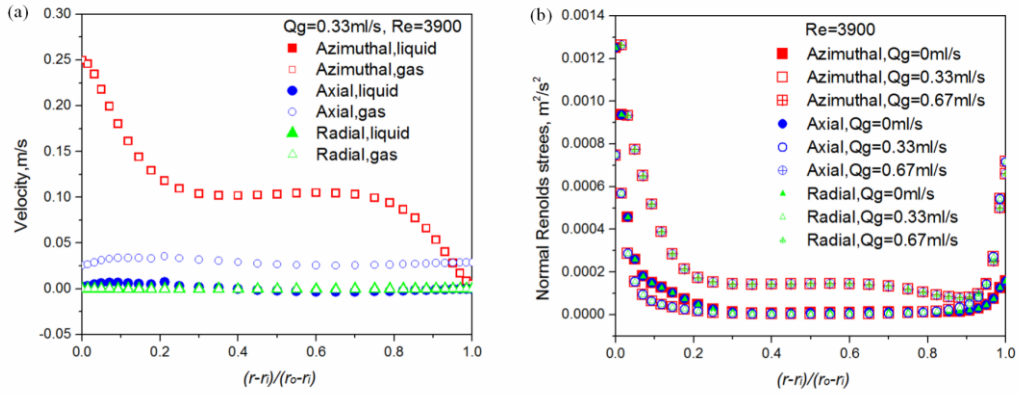


Figure 3.12. Simulated three components of the liquid velocity (a) and simulated three components of the normal Reynolds stress tensor for both single-phase case and two-phase case (b).

### 3.4. Conclusion

Bubble effects on Taylor-Couette flow patterns and structures in the weakly Taylor vortex flow regime were numerically investigated by quasi-2D and 3D simulation and compared with experimental data available in the literature. We demonstrated that bubble flow patterns and spatial distributions can be reproduced by an Eulerian-Eulerian two fluid model that includes several interphase forces and a turbulence model. By comparing the contributions of the radial component of various forces acting on the bubble phase, it was shown that radial non-uniformity in the gas phase volume fraction is mainly determined by the balance between the pressure gradient force, the wall lubrication force and the turbulent dispersion force, whereas the virtual mass and lift forces have negligible effect on the spatial distribution of bubbles. It was also demonstrated that gas velocity strongly influences the wavelength of Taylor vortices, in contrast to the azimuthal Reynolds number, which has little effect in the range  $Re = 600-3900$ .

The azimuthal and radial velocity components for both phases were found to be nearly identical, whereas due to the imposed axial gas flow, the axial gas velocity is significantly greater than the axial liquid velocity. Hence, changing the inlet gas velocity has a stronger influence on the bubble slip velocity than does changing the azimuthal Reynolds number. Neglecting changes in the size and spatial distribution of bubbles, it follows logically that gas flow rate can be expected to have a greater impact on interphase mass transport than does cylinder rotation speed. It was also observed that for fixed azimuthal Reynolds number, increasing gas flow rate causes axial elongation of vortices and, at sufficiently high flow rates, complete disruption. In order to organize these observations, a regime map was constructed for two fluid Taylor-Couette flow based upon the three observed patterns (annulus filled with vortices, partially filled with vortices, and no vortices) using axial Reynolds number and azimuthal Reynolds number as parameters. While this flow regime map provides a good starting point for systematically investigating semibatch gas-liquid Taylor vortex flow, a better understanding of these flow structures (for example secondary instabilities such as wavy vortex flow) is needed in order to rationally design two-phase Taylor vortex reactors. Such an understanding requires additional experiments to obtain more extensive velocity field and phase distribution information, which in turn could be used to validate and assess both quasi-two dimensional and three dimensional CFD simulations.

## **CHAPTER 4. AN ADAPTIVE MODEL FOR GAS-LIQUID MASS TRANSFER IN A MULTIPHASE TAYLOR-COUPETTE REACTOR**

Modified from the paper “Gao X, Kong B, Ramezani M, Olsen MG, Vigil RD. 2015. An adaptive model for gas-liquid mass transfer in a Taylor vortex reactor. *Int J of Heat Mass Transfer* 91: 433-446.”

Gas–liquid Taylor–Couette flow devices have attracted interest for use as chemical and biological reactors, and consequently the accurate prediction of interphase mass transfer coefficients is crucial for their design and optimization. However, gas–liquid mass transport in these systems depends on many factors such as the local velocity field, turbulent energy dissipation rate, and the spatial distribution and size of bubbles, which in turn have complicated dependencies on process, geometric, and hydrodynamic parameters. Here we overcome these problems by employing a recently developed and validated Eulerian two-phase CFD model to compute local values of the mass transfer coefficient based upon the Higbie theory. This approach requires good estimates for mass transfer exposure times, and these are obtained by using a novel approach that automatically selects the appropriate expression (either the penetration model or eddy cell model) based upon local flow conditions. By comparing the simulation predictions with data from corresponding oxygen mass transfer experiments, it is demonstrated that this adaptive mass transfer model provides an excellent description for both the local and global mass transfer of oxygen in a semibatch

gas–liquid Taylor–Couette reactor for a wide range of azimuthal Reynolds numbers and axial gas flow rates.

#### 4.1. Introduction

Interphase mass transfer plays a crucial role in the design, scale-up and optimization of multiphase chemical and biological reactors. As a result, considerable effort has been expended to develop reliable correlations for estimating interphase mass transfer coefficients. For gas–liquid systems, it is usually assumed that the liquid side mass transfer resistance at gas–liquid interfaces limits interphase mass transport, and therefore gas side mass transfer resistance is neglected (Deckwer et al., 1974). Hence, the liquid side volumetric mass transfer coefficient ( $k_L a$ ) is used to compute the overall mass transfer rate across a gas–liquid interface. However, it can be difficult to estimate  $k_L a$  because of the many factors affecting this quantity, such as gas holdup and bubble size, slip velocity, and turbulent energy dissipation rate. These factors in turn depend non-trivially on reactor operating conditions, geometry, and physical properties of the gas and liquid phases. Some dependencies of the volumetric mass transfer coefficient on hydrodynamic, operating, and geometric parameters are illustrated in Fig. 4.1.

Although numerous empirical correlations have been developed for gas–liquid mass transfer in bubble columns (Gourich et al., 2006; Colombet et al., 2011; Muroyama et al., 2013), airlift reactors (Kawase and Hashiguchi, 1996; Huang et al., 2010; Cockx et al., 2001), and stirred tanks (García-Ochoa and Gomez, 2004; 1998; 2005; Özbek and Gayik, 2001), comparatively little is known concerning interphase mass transfer in Taylor–Couette flow cells (Kadam et al., 2008; Wroński et al., 1999; Dłuska et al., 2001; 2004), which have

recently gained interest for use as bioreactors (Haut et al., 2003; Sorg et al., 2011; Zhu et al., 2010; Kliphuis et al., 2010; Qiao et al., 2014; Kong et al., 2013; Kong and Vigil, 2014). These devices, which consist of fluids confined in the annular space between two coaxial cylinders (see Fig. 4.2) with the inner cylinder undergoing rotation, can be used to generate pairs of toroidal vortices with mixing characteristics advantageous for culturing a variety of microorganisms (Haut et al., 2003; Sorg et al., 2011; Zhu et al., 2010; Qiao et al., 2014; Kong et al., 2013). Specifically, as the inner cylinder rotation speed increases above a critical value that depends upon the reactor geometry and fluid properties, the fluid undergoes transition from laminar Couette flow (circular flow with only an azimuthal component) to laminar Taylor vortex flow. Subsequent increases in cylinder rotation speed lead to higher order instabilities such as wavy vortex flow, modulated wavy vortex flow, and turbulent Taylor vortex flow (Andereck et al., 1986; Coles, 1965; Wang et al., 2005a; 2005b).

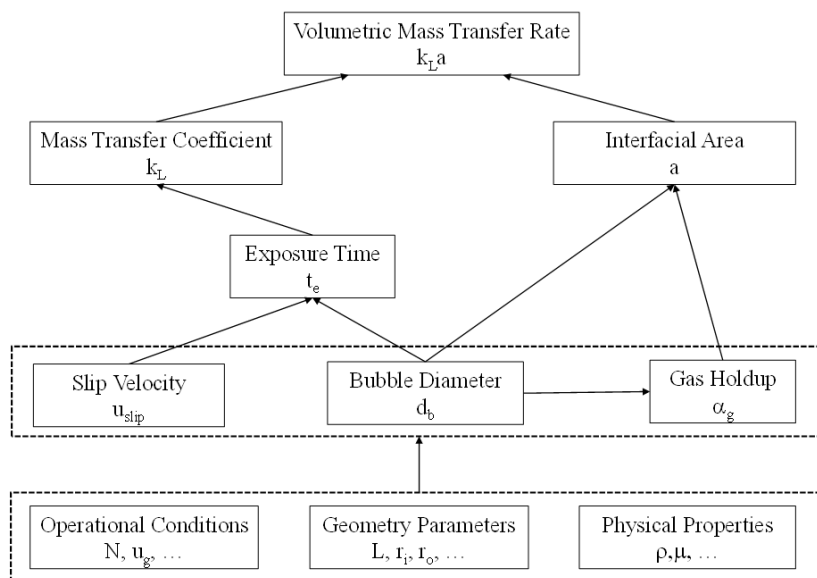


Figure 4.1. Illustration of the relationships between volumetric mass transfer coefficient and various geometric, operational, and hydrodynamic parameters.

Although a large literature concerning single phase Taylor vortex flow has been built over many years, far less is understood concerning multiphase Taylor vortex flow, particularly with respect to mass transport in such systems. The addition of a second fluid phase leads to instabilities and flow patterns not observed in single-phase flow (e.g. phase inversions and nonhomogeneous distribution of fluid phases) (Joseph et al., 1984; Renardy and Joseph, 1985; Joseph and Preziosi, 1987; Zhu et al., 2000; Zhu and Vigil, 2001). The available information for interphase mass transport in two-phase Taylor–Couette flow is even more limited, and until now, no computational or theoretical models for interphase mass transfer have been developed for this system. Most of what has previously been reported concerning interphase mass transfer in Taylor–Couette flow is attributable to work performed by Wroński et al. (1999) and Dluska et al. (2001; 2004), who carried out experiments in a continuously-fed horizontally-oriented gas–liquid Taylor–Couette reactor and observed volumetric mass transfer coefficients with values on the order of  $0.1 \text{ s}^{-1}$ . However, the flow patterns generated in a horizontal gas–liquid reactor are significantly different from those that are produced in a vertically oriented reactor, because axial symmetry is destroyed in a horizontal reactor by the vertical gravity field that gives rise to a nonaxisymmetric buoyant force.

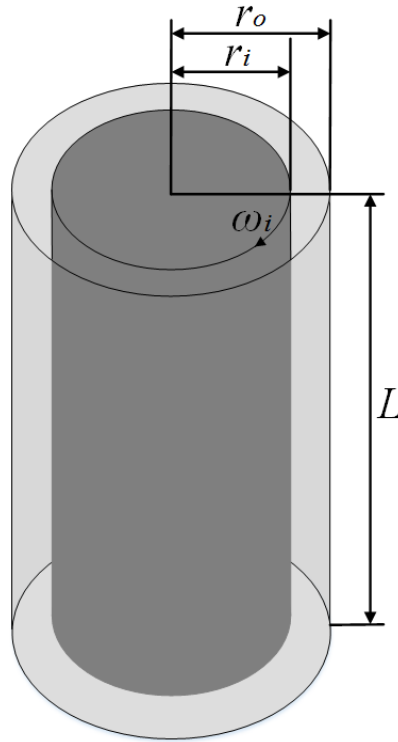


Figure 4.2. Configuration of a Taylor vortex reactor.

In contrast to horizontally oriented gas–liquid Taylor–Couette reactors, the buoyant force acting on gas bubbles is parallel to the cylinder axis in vertically oriented reactors. As a result, effluent gas can easily be separated from the liquid phase by feeding gas through the bottom of the reactor and by providing sufficient head space for bubbles to rupture as they emerge from the liquid free surface at the top of the reactor. Such a configuration is particularly useful for delivery of carbon dioxide and removal of oxygen during the culture of phototrophic microorganisms. Interest in vertically oriented gas–liquid Taylor vortex reactors has also been driven by the discovery of the existence of nontrivial bubble distributions and dramatic drag reduction on the rotating inner cylinder (van Gils et al., 2011; 2013; Chouippe et al., 2014; Maryami et al., 2014).

Recently the authors carried out oxygen transport experiments in a vertical gas–liquid Taylor–Couette reactor (Ramezani et al., 2015). They found that gas–liquid mass transfer coefficients in the vertical reactor were significantly smaller than those reported for horizontal reactors. In addition, the authors developed empirical correlations for the mass transfer coefficient and the mean bubble diameter as functions of the liquid azimuthal Reynolds number and the gas axial Reynolds number. While these correlations are useful for understanding the relative contributions of the azimuthal and axial flows in determining the magnitude of mass transfer coefficients, they cannot easily be generalized because (a) Taylor vortex flow patterns cannot be predicted based solely upon axial and azimuthal Reynolds numbers (they also depend upon reactor geometry) and (b) Taylor vortex flow is known to exhibit flow pattern multiplicity, depending upon flow history (Andereck et al., 1986).

In view of the above discussion, it is evident that the prediction of interphase mass transport coefficients for arbitrary Taylor–Couette reactor geometries and operating conditions requires an approach that incorporates details of the fluid flow. To that end, and by making use of our recently-developed computational fluid dynamics simulations for two-phase Taylor vortex flow (Gao et al., 2015a; 2015b), in this work we compute interphase mass transfer coefficients by integrating local fluid velocity and phase distribution information into well-known theoretical models for interfacial mass transport. This method for computing mass transfer coefficients is then validated by comparing model predictions against our existing experimental data for interphase mass transport in a vertical Taylor–Couette gas–liquid reactor (Ramezani et al., 2015). Indeed, by properly selecting the mass transport model appropriate to the fluid flow regime, we demonstrate that this computational

approach is capable of reproducing experimental data with high accuracy. Consequently, by making use of information obtained from the computational fluid dynamics (CFD) simulations that is difficult to obtain experimentally, we are able to identify the mechanisms that most strongly impact interphase mass transfer in vertical gas–liquid Taylor–Couette devices.

The remainder of the paper is organized as follows. In Sections 4.2 and 4.3 we present the model equations and computational details for both the CFD simulations and the mass transfer coefficient calculations. In Section 4.4 we validate the computational approach for the prediction of interphase mass transport coefficients by comparing simulation results with experimental data. The computational results are also discussed in greater detail, including consideration of factors such as gas spatial distribution and fluid flow in regions with high bubble concentrations. General conclusions are presented in Section 4.5.

## 4.2. Model equations

### 4.2.1. CFD model for bubbly Taylor–Couette flow

In this work, the two-phase fluid flow was modeled using an Eulerian–Eulerian approach that we recently employed and validated for bubbly Taylor–Couette flow (Gao et al., 2015b). The flow was assumed to be axisymmetric (Gao et al., 2015a; 2015b; Sathe et al., 2009), so that the quasi-two-dimensional mass, momentum, and species transport equations include an axisymmetric azimuthal velocity component:

$$\frac{\partial}{\partial t}(\alpha_k \rho_k) + \nabla \cdot (\alpha_k \rho_k \vec{u}_k) = S_{pk} \quad (4.1)$$

$$\frac{\partial}{\partial t}(\alpha_k \rho_k \vec{u}_k) + \nabla \cdot (\alpha_k \rho_k \vec{u}_k \vec{u}_k) = -\alpha_k \nabla p + \nabla \cdot (\overline{\overline{\tau_k}} + \overline{\overline{\tau_k^{\text{Re}}}}) + S_{pk} \vec{u}_{pk} + \alpha_k \rho_k \vec{g} + \vec{F}_{lk} \quad (4.2)$$

$$\frac{\partial}{\partial t}(\alpha_k \rho_k Y_k^i) + \nabla \cdot (\alpha_k \rho_k \vec{u}_k Y_k^i) = -\nabla \cdot \alpha J_k^i + S_{pk}^i \quad (4.3)$$

Here,  $\alpha_k$  and  $\vec{u}_k$  are the phase volume fraction and the phase velocity, respectively.  $Y_k^i$  is the mass fraction of species  $i$  in phase  $k$ . The term  $S_{pk}$  is the rate of mass transfer from phase  $p$  to phase  $k$ . The phase stress and Reynolds stress tensors are represented by  $\overline{\overline{\tau_k}}$  and  $\overline{\overline{\tau_k^{\text{Re}}}}$ , respectively.  $J_k^i$  and  $S_{pk}^i$  represent the diffusive flux and the net rate of appearance of species  $i$  due to interphase mass transfer. The term  $\vec{F}_{lk}$  is the interphase momentum exchange term, which can be decomposed into at least five independent interphase forces (Gao et al., 2015a; 2015b; 2013):

$$\vec{F}_{lk} = \vec{F}_D + \vec{F}_L + \vec{F}_{VM} + \vec{F}_W + \vec{F}_T \quad (4.4)$$

These interphase forces represent drag, lift, virtual mass, wall lubrication, and turbulent dispersion, respectively. The constitutive relations and model constants are summarized in Table 4.1 and Table 4.2, respectively. The rationale for the selection of these five interphase forces is as follows. In a recent report on simulation of turbulent gas–liquid Taylor–Couette flow, it was demonstrated that the radial bubble distribution depends primarily upon the competition between the radial pressure gradient, the turbulent dispersion force, and to a lesser extent wall lubrication forces (Gao et al., 2015b). However, because the axial motion of bubbles is driven by buoyancy, it can be expected that the same interphase forces important for accurately simulating bubble columns, namely drag, virtual mass, and lift forces, must also be included in the analysis (Monahan and Fox, 2007). A fuller discussion of various interphase force terms can be found in the recent review article by Buffo and Marchisio (Buffo and Marchisio, 2014).

Table 4.1. Constitutive relations for bubbly Taylor-Couette two-fluid model

Drag model (Tomiyama et al., 1998)	$\vec{F}_{Dg} = -\vec{F}_{Dl} = \frac{3}{4} \alpha_g \alpha_l \frac{\rho_l}{d_b} C_D \left  \vec{u}_g - \vec{u}_l \right  \left( \vec{u}_l - \vec{u}_g \right)$ $C_D = \max\left(\min\left(\frac{24}{\text{Re}_b} (1 + 0.15 \text{Re}_b^{0.687}), \frac{72}{\text{Re}_b}\right), \frac{8}{3} \frac{E_O}{E_O + 4}\right)$
Lift force (Antal et al., 1991)	$\vec{F}_{Lg} = -\vec{F}_{Ll} = -C_L \alpha_g \rho_l \left( \vec{u}_l - \vec{u}_g \right) \times (\nabla \times \vec{u}_l)$
Virtual mass force (Antal et al., 1991)	$\vec{F}_{VMg} = -\vec{F}_{VMl} = C_{VM} \alpha_g \rho_l \left( \frac{d}{dt} (\vec{u}_l - \vec{u}_g) + \vec{u}_l \cdot \nabla \vec{u}_l - \vec{u}_g \cdot \nabla \vec{u}_g \right)$
Lubrication wall force (Antal et al., 1991)	$\vec{F}_{Wg} = -\vec{F}_{Wl} = -\frac{\alpha_g \rho_l \left  \vec{u}_g - \vec{u}_l \right ^2}{d_b} \max\left[0, (C_1 + C_2 \frac{d_b}{y})\right] \vec{n}_r$
Turbulent dispersion force (Huang et al., 2010; Talvy et al., 2007; Behzadi et al., 2004 )	$\vec{F}_{Tg} = -\vec{F}_{Tl} = -\rho_l \overline{u'_g u'_l} \nabla \alpha_g = -C_T \rho_l k_l \nabla \alpha_g$

Table 4.2. Constants in bubbly Taylor-Couette two-fluid model (Gao *et al.*, 2015a; 2015b)

$C_L$	$C_{VM}$	$C_1$	$C_2$	$C_T$
0.02	0.5	-0.01	0.05	2

The source terms attributable to interphase mass transport,  $S_{pk}$ , depend upon the specific physical system under consideration. In this work we seek to validate our computational approach by comparing simulation predictions with our experiments previously reported (Ramezani et al., 2015). In the experiments, the feed liquid and gas phases consisted of water and a binary mixture of oxygen and nitrogen in proportions that approximate the composition of dry air, and the rate of transport of oxygen from the gas bubbles to the water phase was determined from temporal measurements of dissolved oxygen concentration in the liquid phase. Similarly, in this simulation work bubbles are assumed to be dry and the effect

of water vapor on bubble physical properties and interfacial mass transfer is neglected because the saturation pressure of water vapor in the bubbles at room temperature (2310 Pa) is much smaller than the partial pressures of oxygen and nitrogen. Hence only the interphase transport of oxygen and nitrogen was considered at the bubble–liquid interface, governed by the following equation:

$$R_{gl}^i = (k_L a)(c_{l,*}^i - c_l^i), \quad i = \text{O}_2, \text{N}_2 \quad (4.5)$$

where  $R_{gl}^i$  is the interphase mass transfer rate of species  $i$ ,  $c_{l,*}^i = P^i / H^i$ ,  $H_g^i$  is the Henry's Law constant for species  $i$ ,  $k_L a$  is the volumetric mass transfer coefficient, and  $a$  is the specific interfacial area,

$$a = \frac{6\alpha_g}{d_b(1 - \alpha_g)} \quad (4.6)$$

Thus, the total volumetric mass transfer rate can be expressed as

$$S_{gl} = \sum_{i=1}^I S_{gl}^i = - \sum_{i=1}^I \alpha_g R_{gl}^i M_w^i \quad (4.7)$$

where  $M_w^i$  is the molecular weight of species  $i$ . Although tracking of interphase nitrogen transport was included for comprehensiveness, simulations performed with and without nitrogen transport demonstrated that no difference was found in the predictions, due to the low solubility of nitrogen in water. Consequently it is not necessary to include interphase nitrogen transport in the model equations. Lastly, we note that care must be taken in the use of Eq. (4.6) for bubble populations with non-monodisperse distributions. In such cases, it is necessary to use the Sauter mean bubble diameter for  $d_b$ .

#### 4.2.2. Turbulence modeling

In this work, the standard  $k$ - $\omega$  model was employed to simulate turbulence, as this method has been shown to accurately predict velocity fields, global gas holdup, and the spatial bubble distribution in turbulent gas–liquid Taylor–Couette flow (Gao et al., 2015b). Only liquid phase turbulence is considered, since the bubble phase volume fraction is very low (<2%). Indeed, we performed simulations that include bubble induced turbulence (by embedding the Sato bubble induced turbulence model into the standard turbulence model – see Sato and Sekoguchi (Sato and Sekoguchi, 1975) for details) and found no significant difference in the predictions compared to cases simulated without bubble induced turbulence. For the same reason, bubble–bubble interactions were also neglected. The turbulent kinetic energy ( $k_l$ ) and the specific dissipation rate ( $\omega_l$ ) are governed by the following transport equations (Wilcox, 1998):

$$\frac{\partial}{\partial t}(\alpha_l \rho_l k_l) + \nabla \cdot (\alpha_l \rho_l k_l \vec{u}_l) = \nabla \cdot (\alpha_l (\mu_l + \frac{\mu_{l,t}}{\sigma_k}) \nabla k_l) + \alpha_l G_k - \alpha_l Y_k \quad (4.8)$$

$$\frac{\partial}{\partial t}(\alpha_l \rho_l \omega_l) + \nabla \cdot (\alpha_l \rho_l \omega_l \vec{u}_l) = \nabla \cdot (\alpha_l (\mu_l + \frac{\mu_{l,t}}{\sigma_\omega}) \nabla \omega_l) + \alpha_l G_\omega - \alpha_l Y_\omega \quad (4.9)$$

where  $G_k$  and  $Y_k$  represent the generation and dissipation of turbulent kinetic energy, and  $G_\omega$  and  $Y_\omega$  represent the generation and dissipation of  $\omega$ , respectively. The terms  $\sigma_k$  and  $\sigma_\omega$  represent the turbulent Prandtl number for  $k$  and  $\omega$ , respectively, and are both taken to be equal to 2.0. The turbulent viscosity  $\mu_{l,t}$  depends upon  $k_l$  and  $\omega_l$  as follows:

$$\mu_{l,t} = \frac{\rho_l k_l}{\omega_l} \quad (4.10)$$

### 4.2.3. Mass transfer models

Commonly employed models for the prediction of the liquid-side mass transport coefficient for gas bubbles in a continuous liquid phase include the penetration (Higbie, 1935), eddy cell (Lamont and Scott, 1970) and laminar boundary layer models (Griffith, 1960). Thorough overviews of these and other models can be found in Huang et al. (2010) and Garcia-Ochoa and Gomez (2009). The laminar boundary layer model is written as

$$k_L = C \sqrt{\frac{u_{slip}}{d_b}} D_L^{2/3} \nu_l^{-1/6} \quad (4.11)$$

where the slip velocity is defined as  $u_{slip} = \left| \vec{u}_g - \vec{u}_l \right|$ ,  $d_b$  is the bubble diameter,  $D_L$  is the diffusivity of the solute in the liquid phase,  $\nu_l$  is the kinematic viscosity of the liquid, and  $C$  is a constant. Different values of  $C$  have been reported including 0.6 (Huang et al., 2010; Lochiel and Calderbank, 1964) and 0.42 (Griffith, 1960; Linek et al., 2004). The laminar boundary layer model can be applied only for rigid bubbles with small diameter ( $d_b < 1$  mm) or bubbles with completely immobile surface due to contamination (Alves et al., 2006). Some authors have found that the laminar boundary layer model underpredicts the mass transfer coefficient when it is applied to bubble columns or stirred tanks (Huang et al., 2010).

The penetration theory proposed by Higbie (1935) assumes that bubble surfaces are immobile, but it accounts for unsteady diffusion of gas into the liquid at the gas–liquid interface by introducing a characteristic gas–liquid exposure time, leading to the following expression:

$$k_L = \left( \frac{4D_L}{\pi t_e} \right)^{1/2} \quad (4.12)$$

An estimate is needed for the exposure time, given by  $t_e = d_b / F^2 u_{slip}$ , where  $u_{slip}$  is the slip velocity,  $d_b$  is the bubble diameter, and where  $F$  is a constant. Substitution of the exposure time into Eq. (4.12) leads to

$$k_L = F \sqrt{\frac{4D_L u_{slip}}{\pi d_b}} \quad (4.13)$$

In the Higbie penetration theory for a single bubble, the constant  $F$  is taken as unity, whereas smaller values have been used by investigators when considering bubble swarms and high gas volume fractions. For instance, Wang et al. (2007) found that the volumetric mass transfer rate in a bubble column can be well predicted using  $F=0.8$ .

The penetration theory model is known to underpredict mass transfer for highly turbulent flows, and Eq. 4.12 implies that this is caused by an overestimation of the exposure time. Indeed, several experimental studies of gas–liquid transport in turbulent flow have revealed that the liquid-side mass transfer is controlled by interfacial surface renewal by small scale eddies rather than by any measure of the mean flow of the liquid relative to the bubbles, such as the slip velocity (Lamont and Scott, 1970). As a result, for highly turbulent flow it is more appropriate to estimate the characteristic gas–liquid exposure time using the Kolmogorov theory of isotropic turbulence, which leads to the following “eddy cell model”:

$$k_L = K \sqrt{\frac{4D_L}{\pi} \left( \frac{\varepsilon_l}{\nu_l} \right)^{1/2}} = K' \sqrt{D_L \left( \frac{\varepsilon_l}{\nu_l} \right)^{1/2}} \quad (4.14)$$

In the above equation,  $\varepsilon_l$  represents the liquid turbulence dissipation rate. Various values of the model constant  $K'=(4/\pi)^{1/2}K$  have been suggested in the literature, e.g.  $(4/\pi)^{1/2}$  (Kawase et al., 1987), 0.592 (Alves et al., 2006), 0.4 (Lamont and Scott, 1970), 0.301 (Kawase and

Hashiguchi, 1996), 0.523 (Linek et al., 2004), 0.27 (Wang et al., 2007). Wang (2007) has hypothesized that the inconsistency of the various estimates for  $K'$  stem from two causes including (1) the difficulty in accurately calculating turbulent dissipation rates and (2) lack of consideration of the bubble swarm effect on mass transfer.

Although the various mass transfer models discussed above find wide usage, none are appropriate for simulating all of the local conditions and flow patterns that arise in Taylor–Couette devices. Specifically, the assumptions associated with the classical penetration theory model are inconsistent with turbulent flow and lead to an overestimation of the exposure time at high cylinder rotation speeds, whereas the eddy cell model overpredicts exposure time for low dissipation rates at low rotation speeds. For this reason, we introduce an adaptive mass transfer model that combines the strengths of both models and that can be used over a wide range of Reynolds numbers and at all locations in the reactor. Specifically, by computing the local exposure time for both models, the most appropriate model for given flow conditions can be selected by choosing the one that predicts the smallest exposure time. i.e.,

$$t_e = \min\left(\frac{1}{F^2} \frac{d_b}{u_{slip}}, \frac{1}{K^2} \left(\frac{v_l}{\varepsilon_l}\right)^{1/2}\right) \quad (4.15)$$

Here,  $F$  and  $K$  are adjustable constants that are needed to account for the fact that the slip velocity is sensitive to the drag model used and the turbulence dissipation rate is sensitive to the turbulence model employed. Consequently, the adaptive mass transfer model used in this work can be expressed as follows:

$$k_L = \max\left(F \sqrt{\frac{4D_L}{\pi} \frac{u_{slip}}{d_b}}, K \sqrt{\frac{4D_L}{\pi} \left(\frac{\varepsilon}{v_l}\right)^{1/2}}\right) \quad (4.16)$$

In order to make use of the penetration model, the eddy cell model, or the adaptive model described above, it is necessary to choose values for the model constants  $F$  and  $K$ . Although the range of previously reported values for  $F$  and  $K$  is not large, we have chosen to fit these parameters by making use of measurements reported in our experimental investigation of oxygen mass transport in gas–liquid Taylor–Couette (Ramezani et al., 2015), which is described in more detail in Section 4.4.1. After testing several values for both  $F$  and  $K$ , these constants were taken to be  $F=1.2$  and  $K=0.35$ . These values are consistent with those used by other investigators, as was discussed previously.

### 4.3. Simulation approach and computational details

#### 4.3.1. Overview of computational approach

As was previously mentioned, the overall strategy for computing interphase mass transfer coefficients includes (1) performing two-phase CFD simulations in order to compute instantaneous and time-averaged velocity fields and fluid phase distributions, and (2) computing local interphase mass transfer coefficients  $k_L$  from Eq. (4.16) by using flow field predictions to estimate turbulence energy dissipation rates ( $\varepsilon$ ) and slip velocities ( $u_{slip} = \left| \vec{u}_g - \vec{u}_l \right|$ ). It should be noted that the Eulerian CFD approach used here requires foreknowledge of the mean gas bubble diameter, as this quantity is needed to compute components of the interfacial momentum exchange rate  $\vec{F}_k$ , such as drag and virtual mass. Furthermore, once the mean bubble diameter is specified and the resulting gas holdup is computed, the specific surface area can also be computed from Eq. 4.6, and subsequently interphase mass transfer rates can be determined. For this reason, and also to validate the

computational approach with experiments, the simulations reported here were performed using the same geometry and fluids corresponding to the experimental conditions used by Ramezani et al. (2015), who developed the following correlations for the volumetric mass transfer coefficient and mean bubble size in a vertical gas–liquid Taylor–Couette reactor:

$$sh = \frac{k_L a d_b^2}{D_L} = 1.45 \times 10^{-7} \text{Re}_a^{0.82} (\text{Re}_\theta + 1.47 \times 10^4)^{1.61} \quad (4.17)$$

$$\frac{d_b}{r_o - r_i} = 1.0 \times 10^{-5} \text{Re}_a^{0.11} (\text{Re}_\theta + 3.3 \times 10^4)^{0.91} \quad (4.18)$$

In the above expressions,  $d_b$  is the Sauter mean diameter,  $\text{Re}_a$  is the axial Reynolds number based upon the gas flow rate, and  $\text{Re}_\theta$  is the azimuthal Reynolds number based upon the liquid phase fluid properties. Hence, the mean bubble size needed to carry out the CFD simulations was obtained from Eq. (4.18), and the resulting simulation predictions for  $k_L$  were compared against those given by Eq. (4.17).

#### 4.3.2. Computational domain and boundary conditions

A schematic of the Taylor–Couette apparatus used in the experiments of Ramezani et al. (2015) and in the simulations presented here is shown in Fig. 4.3. The rotating inner cylinder has an outer radius of 3.81 cm and the fixed transparent acrylic outer cylinder has an inner radius of 5.08 cm, resulting in a gap width of 1.27 cm. The length of the reactor is 50.8 cm and the reactor is filled to a height of  $h=48$  cm, thus the total liquid working volume within the reactor is 1.70 L. The corresponding radius ratio and aspect ratio of the apparatus are given by  $\eta=r_i/r_o=0.75$  and  $\Gamma=h/(r_o-r_i)=40$ , respectively.

A non-uniform rectangular mesh was employed to simulate the annular flow chamber, and three progressively finer mesh resolutions (20×240, 32×480, 50×720) radial × axial nodes were tested until a grid-independent solution was obtained. Because no differences were observed in the solution between the two finest grids tested, all subsequent computations were performed using the 32×480 mesh. It should be noted that in the near-wall regions a finer grid spacing was used (8 grid points within 2.5 mm of either wall) to capture steep gradients associated with the no-slip boundary conditions. The first layer of grid points was located within the viscous sublayer at wall units  $y^+=3.3$  and 5.0 for the inner and outer cylinders, respectively, and the mesh is depicted graphically in Fig. 4.S1 in the Supplemental Information.

The reactor operated in a semi-batch mode with continuous flow of gas and no feed or removal of liquid. The gas inlet was modeled as a narrow channel with a width of 10 mm near the outer wall at the bottom of the reactor to mimic the feed conditions in the experiment. The boundary at the top of the annular fluid mixture was treated as a gas outflow boundary to simulate the liquid free surface in contact with a head space. In summary, the boundary conditions used were as follows. No-slip conditions were used at solid boundaries, and the azimuthal velocity of the inner cylinder was chosen to match experimental conditions. A fixed gas velocity was prescribed at the gas inlet at the bottom of the reactor and by specifying an inlet bubble volume fraction of 0.05. Pressure outlet boundary conditions were used for both fluid phases.

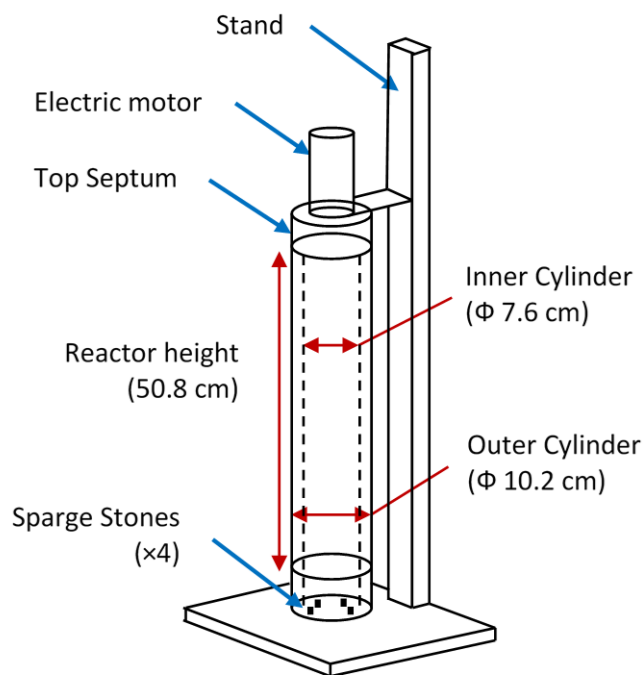


Figure 4.3. Schematic of Taylor–Couette bioreactor used for mass transfer experiments.

Simulations were initialized assuming that only the liquid phase occupied the annular flow chamber so that  $\alpha_g = 0$ . Subsequently, the momentum, mass, and species conservation equations described above were solved in double precision using the commercial finite volume CFD code, ANSYS FLUENT 14.5 (Ansys Inc., US). The interphase mass transfer model was embedded into the CFD code with the aid of user defined functions (UDFs). The pressure–velocity coupling was resolved using the SIMPLE algorithm (Patankar, 1980). Transient CFD simulations were carried out using a time step of  $5 \times 10^{-4}$  s. Generally 30–60 s of simulated physical time was required to reach a quasi steady state wherein the global gas volume fraction did not change with time.

## 4.4. Results and discussion

In our previous work (Gao et al., 2015b), the two-fluid model described in Section 4.2 was validated by direct comparison of simulated results with velocity and phase distribution data from experiments performed by Murai et. al. (Murai et al., 2005), who carried out studies of a vertical semibatch gas–liquid Taylor–Couette reactor. Consequently, we focus here on model predictions for mass transfer calculations.

### 4.4.1. Selection of mass transfer model parameters

As was mentioned in Section 4.2.3, the penetration, eddy cell, and adaptive mass transfer models require specification of the model constants  $F$  and  $K$ . The values used here ( $F=1.2, K=0.35$ ) were obtained by fitting simulation predictions for the penetration and eddy cell models to data from corresponding experiments described in our earlier work (Ramezani et al., 2015). Specifically, in order to select the optimal value of  $F$ , simulations of gas–liquid oxygen mass transfer using the penetration model (4.13) were performed for several values of  $F$  and for the lowest rotation speed considered, and the volumetric averaged values of  $k_L a$  were compared with experimentally determined values. A similar procedure was used to select the optimal value of  $K$ , except that simulations were performed using the eddy cell mass transfer model (4.14) and compared with data from experiments performed at the highest rotation speeds considered.

#### 4.4.2. Validation of adaptive mass transfer model

Axially averaged plots of the radial distribution of the simulated volumetric mass transfer coefficient using different theoretical models are shown in Fig. 4.4(a). Specifically, calculations were performed using the laminar boundary layer (Eq. 4.11), penetration (Eq.4.13), eddy cell (Eq. 4.14), and adaptive (Eq. 4.16) models. It can be seen from these plots that interphase mass transfer is virtually non-existent in the reactor except near the inner cylinder, because that region is where most of the gas is located (Fig. 4.4(b)).

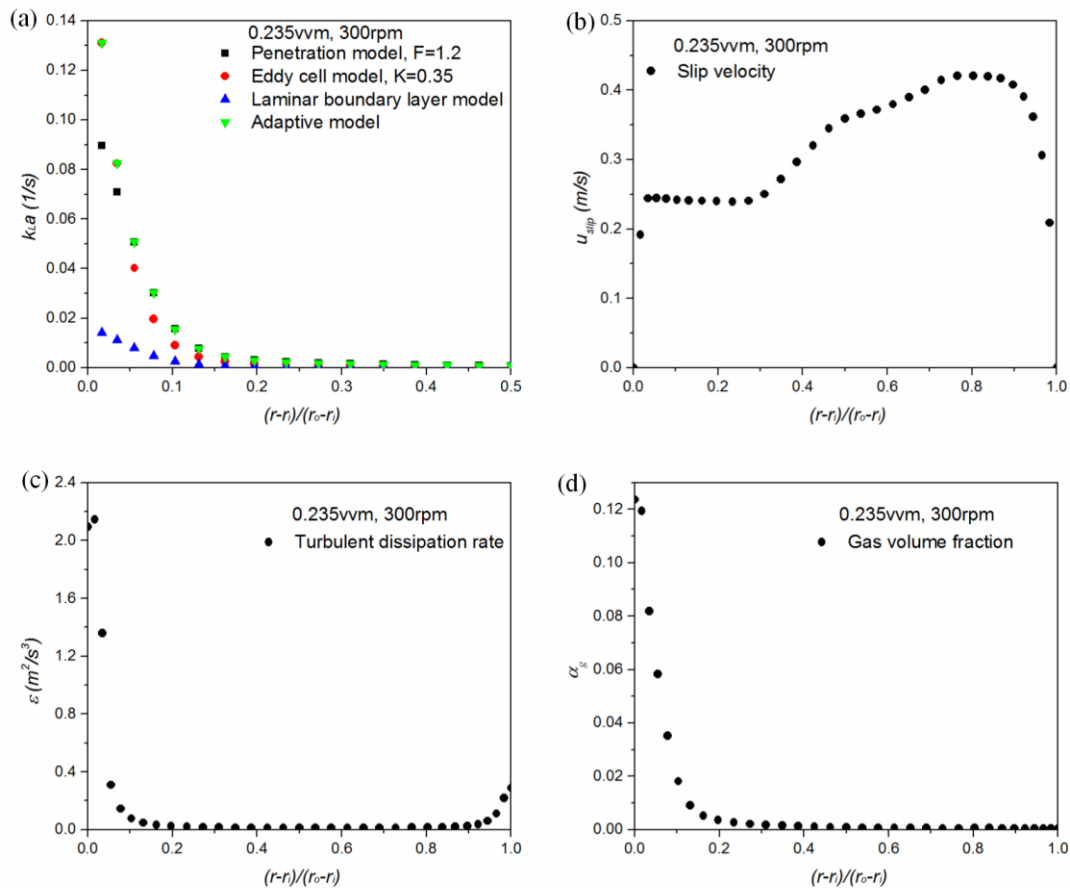


Figure 4.4. Axially averaged radial distributions of (a) volumetric mass transfer coefficient (1/s), (b) gas volume fraction, (c) slip velocity (m/s), and (d) turbulence dissipation rate ( $m^2/s^3$ ) for rotation speed and gas flow rate of 300 rpm and 0.235 vvm, respectively.

Comparison of the simulated spatially averaged volumetric mass transfer coefficient with experimental data is shown in Fig. 4.5 and Fig. 4.6 for various rotation speeds and gas flow rates. Examination of the data presented in Fig. 4.5 suggests that  $k_L a$  is relatively insensitive to rotation speed for speeds lower than 300 rpm, but increases monotonically at higher rotation speeds. In contrast, Fig. 4.6 demonstrates that the volumetric mass transfer coefficient increases with increasing gas flow rate over the entire range of cylinder speeds studied. In all cases considered, mass transfer coefficients computed using the laminar boundary layer model are significantly lower than the corresponding experimental values, as is expected since the flow conditions do not satisfy the laminar boundary layer model assumptions. As expected, the penetration model, which relies on slip velocity to estimate characteristic gas–liquid exposure time, produces values of  $k_L a$  very close to experimental values observed at low rotation speeds, whereas it fails at the higher rotation speeds studied. In contrast, the eddy cell model is more accurate for high cylinder rotation speeds but produces values that are too low at the lower rotation speeds. These results are consistent with findings of Alves et al. (2006), who showed that the penetration model can be used to calculate bubble mass transfer coefficients for turbulent dissipation rates up to at least  $\varepsilon \approx 0.04 \text{ m}^2 \text{ s}^{-3}$ . For the calculations presented in Fig. 4.5 and Fig. 4.6, the penetration model becomes inaccurate for spatially averaged turbulent dissipation rates larger than approximately  $0.1 \text{ m}^2 \text{ s}^{-3}$ . Fortunately, the eddy cell model accurately predicts the volumetric mass transfer coefficient when the turbulent dissipation rate is larger than  $0.1 \text{ m}^2 \text{ s}^{-3}$ . Consequently, the proposed adaptive mass transfer model (Eq. 4.16) combines the advantages of both the penetration and eddy cell models in order to produce good global predictions over

a wide range of turbulent flow conditions by automatically selecting the most appropriate mass transfer model for local conditions. A few exceptions occur at high rotation speeds and low gas flow rates, where the penetration model appears to perform slightly better than the adaptive model. Further experiments under these conditions will be needed in order to determine if the selection criterion of the adaptive model can be improved, for example by accounting for the local gas holdup.

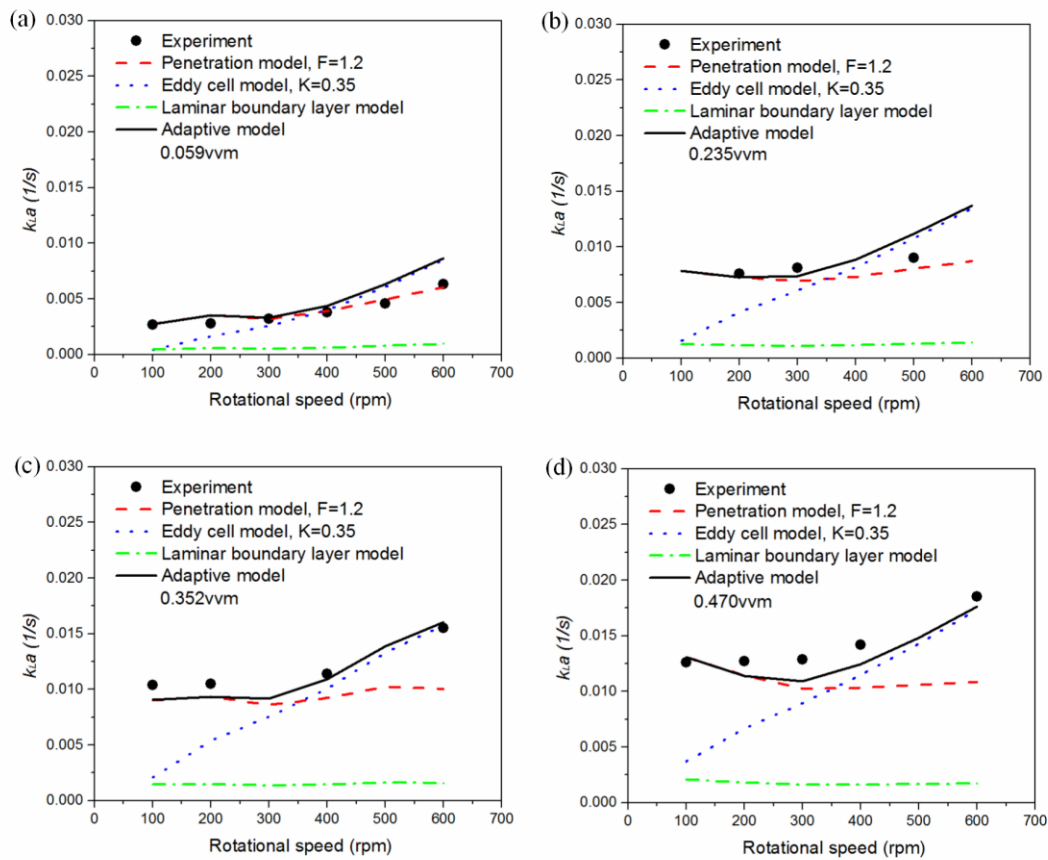


Figure 4.5. Comparison of predicted average volumetric mass transfer rate by different mass transfer models with experimental data under different rotational speeds.

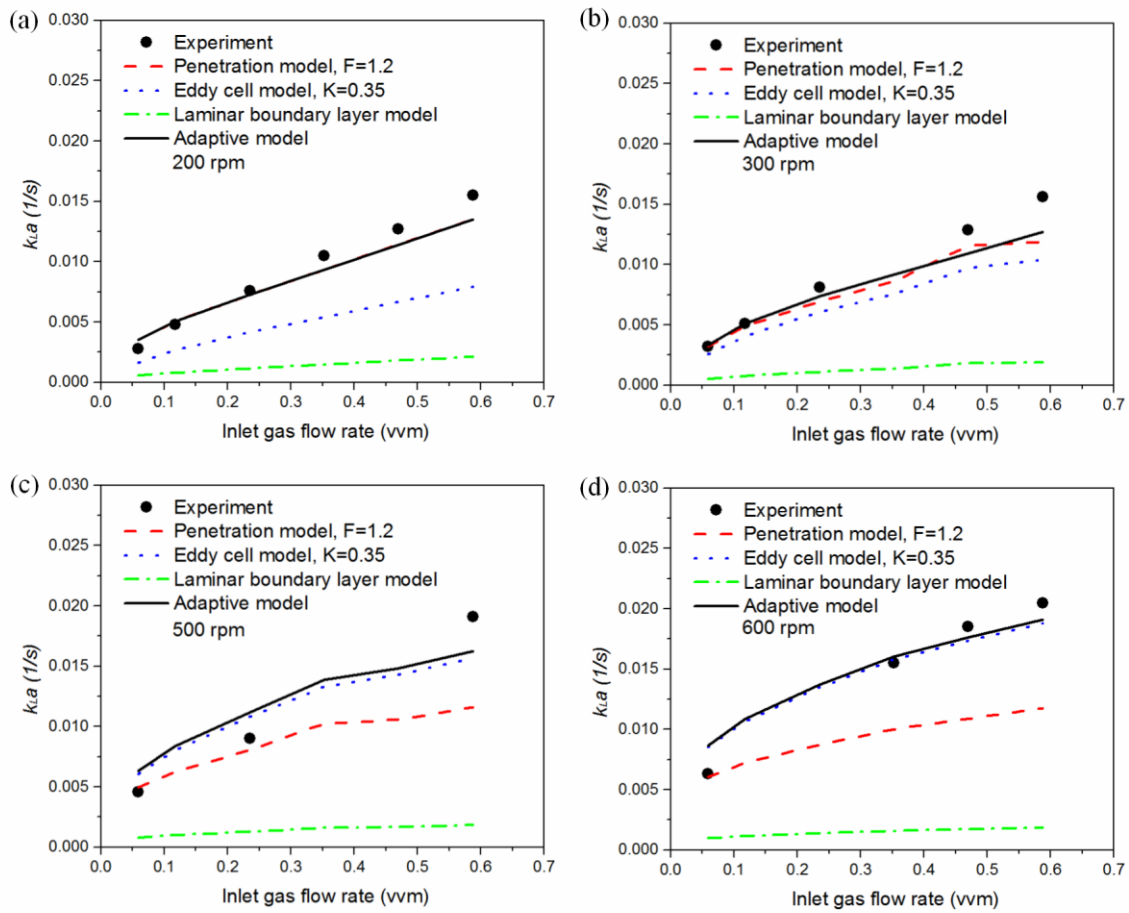


Figure 4.6. Comparison of predicted average volumetric mass transfer rate by different mass transfer models with experimental data under different inlet gas flow rates.

Although the comparison of experimental measurements with predictions based upon the adaptive mass transport model combined with CFD simulations provide evidence for the validity of the modeling approach used here, it is possible to further validate the model by comparing simulation predictions with raw experimental results. For example, in the work of Ramezani et al. (2015), values of  $k_La$  were determined by measuring dissolved oxygen in the liquid phase in response to a step change in the feed gas composition. Simulation of the evolution of dissolved oxygen concentration for one of these experiments (by including species transport equations in the CFD simulations) is shown in Fig. 4.7 and compared

directly to the experimental measurements. Because of startup transients associated with the experimental protocol (more fully described in (Ramezani et al., 2015), there is a brief induction period before dissolved oxygen is detected by the oxygen sensor. This startup transient is not observed in the simulations because mass transfer was enabled only after the two-phase fluid flow reached a steady state. In spite of these important differences, the predictions are in remarkably good agreement with the experiments.

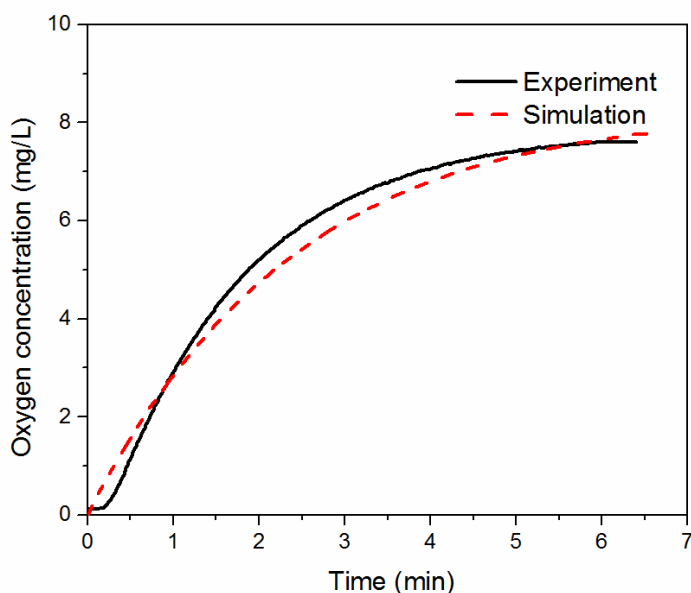


Figure 4.7. Comparison of simulated instantaneous liquid phase oxygen concentration with experimental data of a specific case (0.235 vvm, 300 rpm) at an axial location of 12.7 cm from the bottom of the reactor and near the outer cylinder wall.

We also note that Ramezani et al. (2015) assumed (and confirmed by experiments) that the bulk liquid phase was sufficiently well mixed so that the dissolved oxygen concentration was essentially spatially uniform and therefore dissolved oxygen measurements at a single point are sufficient for determining the global value of  $k_L a$ . Indeed, the simulation of these

experiments predicts spatial homogeneity in the distribution of oxygen in the liquid phase (not shown).

#### 4.4.3. Factors influencing mass transfer rate

For the mass transfer models considered here,  $k_L$  and  $a$  are most directly impacted by slip velocity, dissipation rate and bubble diameter. These quantities in turn are determined by system operating conditions, geometrical parameters, and physical properties, as shown in Fig. 4.1. Here, we discuss the impact of several factors, including quantities that are difficult to obtain from experiments but that are accessible from CFD calculations.

As was discussed previously, a priori knowledge concerning bubble diameter is required to carry out the computations. Specifically, the Sauter mean bubble diameter was estimated using the empirical correlation given by Eq. 4.18 (Ramezani et al., 2015), which depends upon both the azimuthal and axial Reynolds numbers. From this equation, it is evident that the azimuthal Reynolds number (cylinder rotation speed) has a stronger effect on bubble diameter than does the axial Reynolds number (gas flow rate). For example, a fivefold increase in rotation speed produces an increase in bubble diameter of  $\approx 50\%$ , whereas a fivefold increase in gas feed rate only results in a bubble diameter increase of  $\approx 20\%$ . These dependencies in turn have a direct effect on the specific interfacial area  $a$ , as well as indirect effects on  $k_L$  (for example by impacting the bubble drag force and slip velocity).

Fig. 4.4(b)–(d) shows axially averaged plots for the radial distribution of gas volume fraction, slip velocity, and turbulence dissipation rate for a specific gas flow rate and rotation speed (0.235 vvm, 300 rpm), but these results are representative of all the conditions studied

here. As can be seen in Fig. 4.4(c), the largest slip velocities occur near the outer cylinder wall. This phenomenon can be explained by the fact that most of the gas is concentrated near the inner cylinder wall (see Fig. 4.4(b)). The rising gas near the inner cylinder entrains liquid, which recirculates toward the bottom of the reactor near the gas-depleted outer cylinder. As a result, the slip velocity near the outer cylinder is quite large, but there are very few bubbles in this region.

The dependence of the volume averaged (global) slip velocity on gas flow rate and cylinder rotation speed is depicted in Fig. 4.8. Surprisingly, this quantity decreases with increasing gas flow rate. While this result may be counter-intuitive, several factors should be considered when interpreting this result. For example, the slip velocity depends upon the bubble drag. The Tomiyama drag model used here in turn has a very complicated dependence on gas flow rate, particularly as it impacts bubble diameter (Ramezani et al., 2015). In addition, gas flow rate can lead to significant changes in the flow patterns, including stretching the vortex axial wavelength (Gao et al., 2015b).

The global volume averaged turbulent kinetic energy dissipation rate is plotted in Fig. 4.9 for various rotation speeds and gas flow rates, and it is apparent that this quantity is insensitive to the gas flow rate. While such a result may not be surprising since the gas phase is neglected in the turbulence model and bubble induced turbulence is not considered (due to the low gas holdup), the presence of gas could be expected to indirectly impact the dissipation rate since the liquid velocity field is influenced by the presence of gas bubbles. In contrast,  $\varepsilon$  increases rapidly with cylinder rotation speeds above 300 rpm. Furthermore, the

turbulence dissipation rate is much larger near the cylinder walls than in the middle of the annulus, as is evident from Fig. 4.4(d).

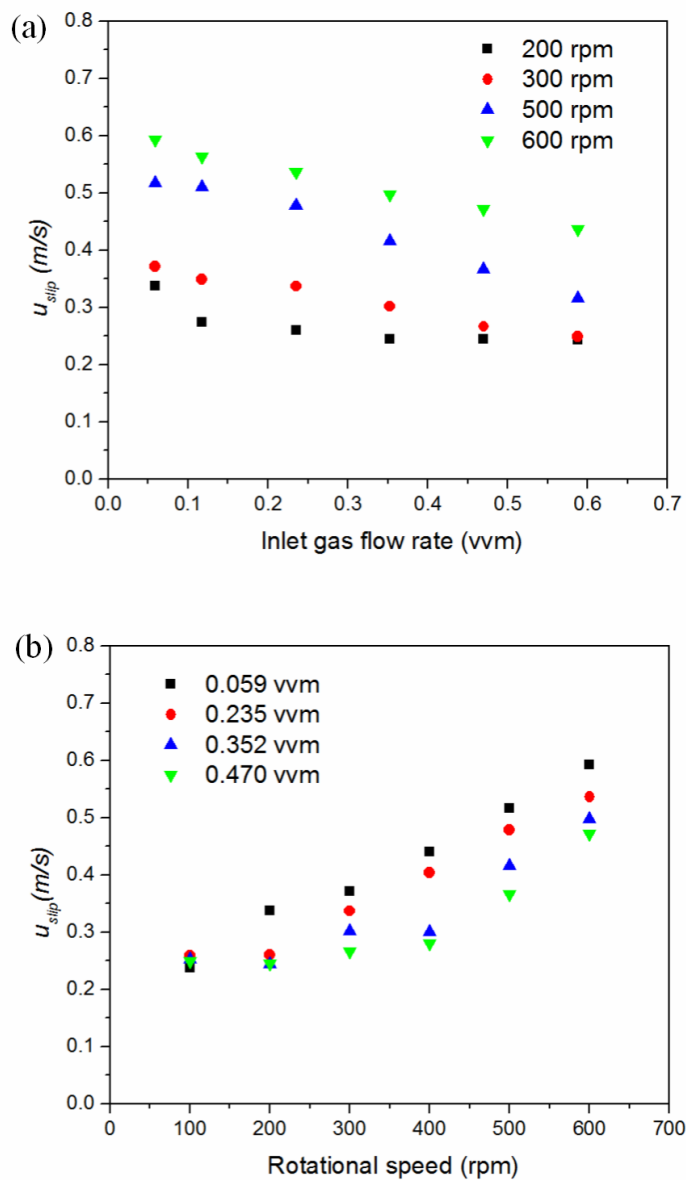


Figure 4.8. Global slip velocity as a function of inlet gas flow rate and cylinder rotation speed.

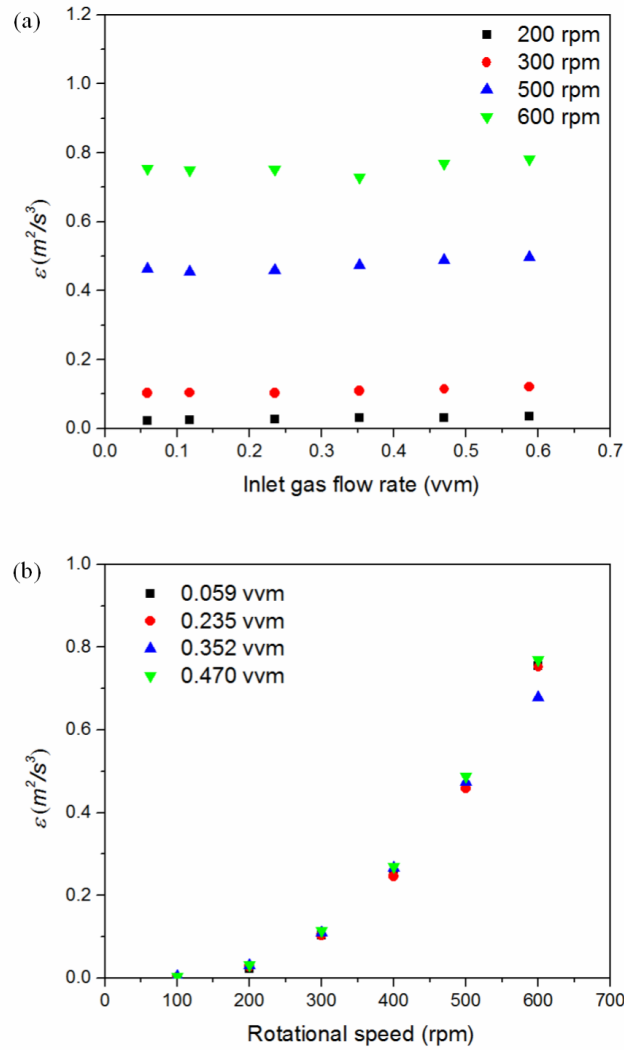


Figure 4.9. Global turbulent dissipation rate as a function of inlet gas flow rate and cylinder rotation speed.

The simulated global gas holdup, which was obtained by spatial averaging, is shown in Fig. 4.10 for the case of no cylinder rotation, and these results are compared with experimental data from our previous work (Ramezani et al., 2015). Although the predicted gas holdup agrees well with the experimental data for a wide range of inlet gas flow rates tested, the simulated gas holdup is slightly but consistently lower than the experimental data, particularly at the higher gas flow rates considered. This discrepancy can probably be

attributed to one or both of two causes, including (1) errors in estimates of the bubble diameter in Eq. 4.18 at high gas flow rates, due to the fact that in such cases individual bubbles are difficult to distinguish because of the presence of bubble swarms (Ramezani et al., 2015) and (2) errors associated with the drag model when bubble swarms are present. Indeed, the Tomiyama (1998) drag model used in this study was developed for single bubbles rather than for bubble swarms, and subsequent studies of drag on bubble swarms in bubble columns (Simonnet et al., 2007; Roghair et al., 2013) have demonstrated that corrections are required, although no such correction currently exists for gas–liquid Taylor–Couette flow.

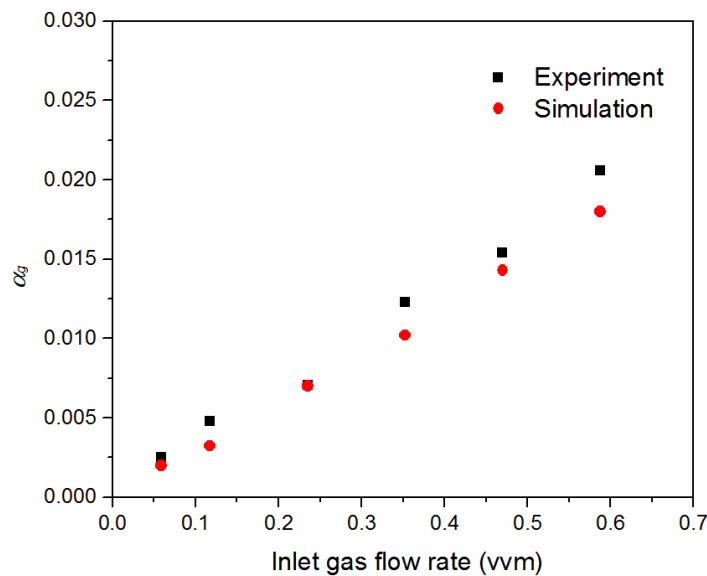


Figure 4.10. Comparison of simulated volume averaged gas holdup with experimental data for the case of no cylinder rotation.

For cases with rotation of the inner cylinder (turbulent Taylor–Couette flow), the predicted global gas holdup is shown in Fig. 4.11 for various gas flow rates and rotation speeds. No experimental data are available for comparison, because the liquid free surface at the top of the reactor has a complex topography when the inner cylinder rotates, and therefore

it is difficult to accurately measure global gas holdup. It can be seen from Fig. 4.11(a) that for constant cylinder rotation speed, gas holdup increases approximately linearly with the inlet gas flow rate. In contrast, for fixed inlet gas flow rate, the gas holdup is relatively insensitive to rotation speeds below 300 rpm ( $Re_\theta = 15200$ ), whereas it increases approximately linearly for rotation speeds above this value.

In view of the non-uniform spatial distribution of slip velocity and turbulent kinetic energy dissipation, it is important to understand not only how the global gas holdup depends upon operating parameters, but also how the spatial distribution of gas is affected. Returning to Fig. 4.4(a), this plot demonstrates that bubbles concentrate near the inner cylinder wall, driven by the strong centrifugal force (Gao et al., 2015b), as was discussed previously. Note that Fig. 4.4(d) shows that this region is also characterized by high dissipation rates. The same results occur for the other flow conditions studied with cylinder rotation, and together these findings demonstrate that interphase mass transport is mainly confined to the region near the inner cylinder, which is discussed further in the next section.

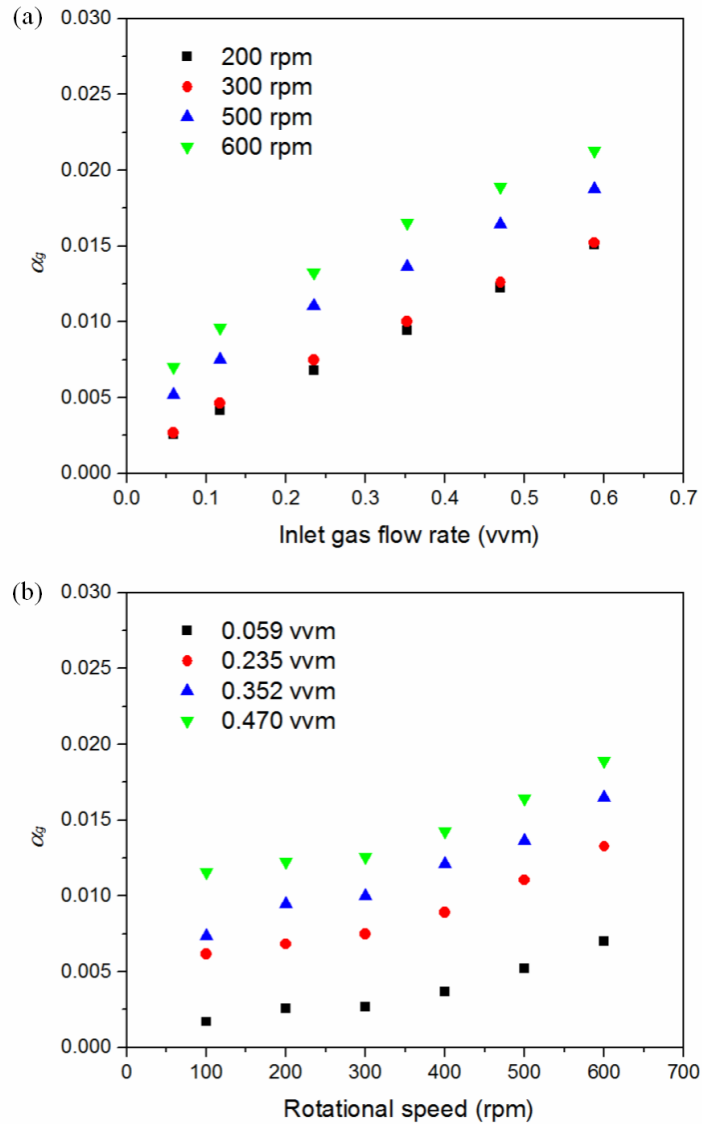


Figure 4.11. Predicted global volume averaged gas fraction as a function of inlet gas flow rate and rotational speed.

#### 4.4.4. Mass transfer coefficients and interfacial area

Although globally averaged values of  $k_L a$  were computed in order to compare model predictions to experimental findings, a deeper understanding of the relationship between this quantity and reactor operating conditions can be obtained by examining the local and global

dependencies of the specific interfacial area  $a$  and the mass transfer coefficient,  $k_L$ , individually. For example, typical local values of the mass transfer coefficient  $k_L$  computed using the adaptive model are shown in the spatial contour plot in Fig. 4.12(a), whereas the local specific interfacial area  $a$ , which was computed based upon knowledge of the gas spatial distribution and the mean bubble diameter, is presented in Fig. 4.12(b). Figs. 4.12(a) and (b) demonstrate that the mass transfer coefficient is much more uniformly distributed (although there are enhancements near both cylinders) than is the specific interfacial area, because the latter quantity depends upon the local gas volume fraction. The enhanced values of the mass transfer coefficient near the inner and outer cylinders reflect the corresponding distributions of turbulent energy dissipation rate and slip velocity discussed previously and depicted in Fig. 4.4.

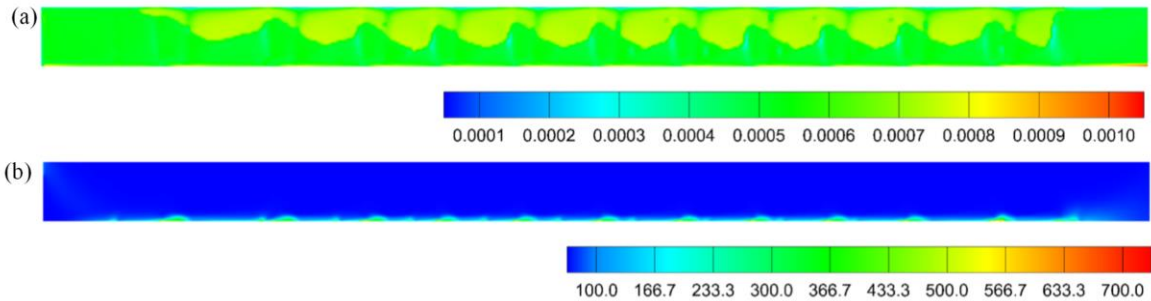


Figure 4.12. Contour plots of (a) mass transfer coefficient  $k_L$  (m/s) predicted by the adaptive mode and (b) specific interfacial area  $a$  (m<sup>2</sup>/m<sup>3</sup>) for a gas flow rate of 0.235 vvm and cylinder rotation speed of 300 rpm. In each plot, the inner cylinder wall is represented by the bottom boundary and the outer cylinder wall is represented by the top boundary.

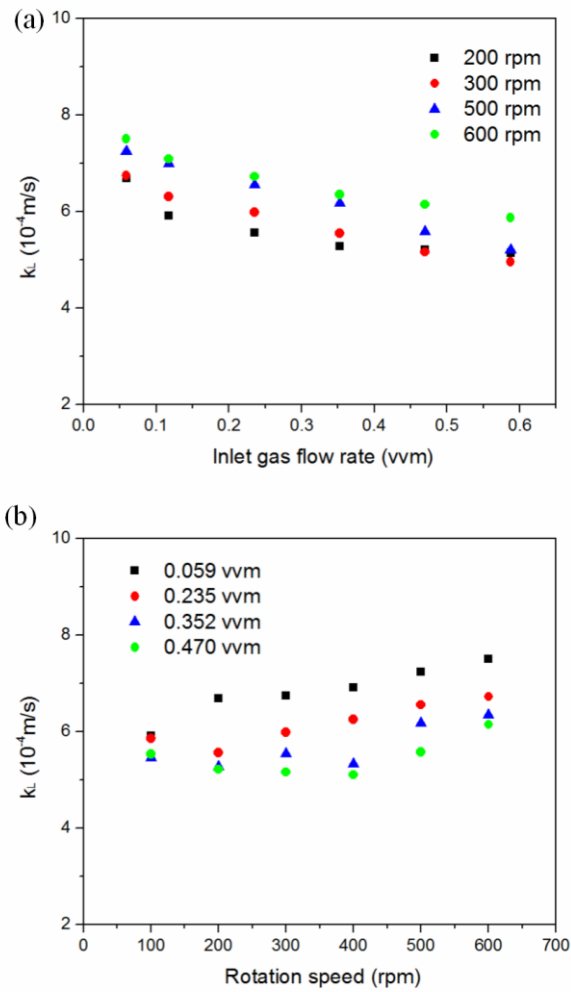


Figure 4.13. Predicted average mass transfer coefficients by the adaptive mass transfer model under different rotational speeds and inlet gas flow rates.

The effect of inlet gas flow rates and rotation speeds on the global spatially averaged values of the mass transfer coefficient and the interfacial area are shown in Fig. 4.13 and Fig. 4.14. Interestingly, the global mass transfer coefficient decreases with increasing gas flow rate at constant cylinder rotation speed. This result can be understood by considering how increased gas flow rate impacts local mass transfer coefficients, which are computed using Eq. 4.16. In particular, we note that for regions with high turbulence dissipation rates,  $k_L$  is governed by the eddy cell model, which is essentially independent of the gas flow rate

because the turbulence dissipation rate is insensitive to gas flow rate (Fig. 4.9(a)) for the conditions studied. In regions with low dissipation rates,  $k_L$  is governed by the penetration theory model, which has a more complicated dependence on gas flow rate. Specifically, as was discussed previously the slip velocity decreases while bubble diameter increases with increasing gas flow rate, thereby causing the local value of  $k_L$  to decrease. Hence, increasing the feed gas flow rate leads to reduced local values of the mass transfer coefficient in regions governed by the penetration theory model and unchanged values in high dissipation rate regions governed by the eddy cell model, thereby leading to an overall decrease in the global mass transfer coefficient.

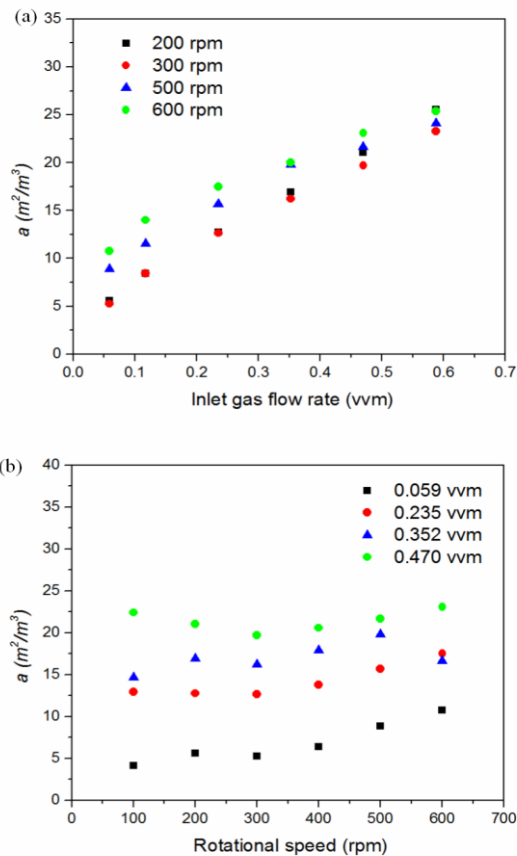


Figure 4.14. Predicted specific interfacial area as a function of cylinder gas flow rate and cylinder rotation speed.

Fig. 4.14 demonstrates that specific interfacial area, which depends upon both the gas holdup and bubble diameter, increases rapidly with gas flow rate. In contrast, for cylinder rotation speeds less than 300 rpm, the specific interfacial area is insensitive to rotation speed. Above 300 rpm, the specific interfacial area increases weakly with rotation speed. In view of the results shown in Fig. 4.13 and Fig. 4.14, the monotonic increase of the volumetric mass transfer coefficient  $k_L a$  with gas flow rate, which was also observed in corresponding experimental work (Ramezani et al., 2015) and reflected in Eq. 4.17, is a result of the rapid increase in specific interfacial area  $a$  even while  $k_L$  decreases with increasing gas flow rate. In contrast to the dependence on gas flow rate,  $k_L a$  is essentially independent of cylinder rotation rate for cylinder speeds below 300 rpm, but at higher speeds increases rapidly due to increases in both  $k_L$  and  $a$ . This more complicated dependence of  $k_L a$  on cylinder rotation speed is also mirrored and confirmed by Eq. 4.17.

#### 4.5. Conclusions

Gas–liquid mass transfer in a Taylor vortex reactor was simulated by using a two-fluid CFD model to obtain local phase distribution and velocity field information, which is then used to select an appropriate mass transfer model for computing the volumetric mass transfer coefficient,  $k_L a$ . The two-fluid model, which was previously validated by comparing velocity and phase distribution predictions with experimental measurements in a vertically oriented semibatch gas–liquid Taylor vortex flow device (Gao et al., 2015b), accounts for two-way coupling of several interphase forces including drag, virtual mass, lift, wall lubrication, and turbulent dispersion. The mass transfer model is based upon the Higbie theory, but automatically adapts to the local hydrodynamic environment by computing exposure time

using either the penetration theory or eddy cell model based upon the turbulence dissipation rate. This adaptive approach was shown to provide much more accurate predictions for the volumetric mass transfer coefficient than does either model used alone.

After developing the approach described above, the effects of several important operating conditions on local and global mass transfer coefficients were explored. For all flow conditions studied, gas bubbles congregate near the inner cylinder, and therefore most interphase mass transfer also is located near the inner cylinder wall. The cylinder rotation speed, in contrast to the gas feed flow rate, strongly impacts the bubble diameter, slip velocity, and turbulence dissipation rate. The gas flow rate has a greater effect than the cylinder speed on gas holdup,  $\alpha_g$ , but because the holdup is small ( $<2\%$ ) even for the highest gas flow rates studied, the rate of interphase mass transfer in general depends more strongly on the azimuthal Reynolds number, in agreement with experimental findings for this system (Ramezani et al., 2015).

Further evidence for the validity of the modeling approach described here was obtained by comparing simulation predictions with experimental measurements for the temporal evolution of the concentration of dissolved oxygen at a specific location in the reactor in response to a step change in feed gas composition. A key assumption in determining mass transfer coefficients from the experimental measurements is that the liquid mixing time is short compared to the characteristic mass transfer time. The simulations support this assumption, and consequently the hypothesis that measurements at a single location in the reactor are sufficient for determining the mass transfer coefficient appears to be justified. Lastly, we note that determination of  $k_L a$  from experimental data at a single location also

requires that the local liquid saturation concentration does not depend upon position (gas partial pressure) and only depends upon temperature. Such an assumption can be justified if the gas phase partial pressures do not vary strongly with position. In the CFD model presented here, no assumption of spatial homogeneity in the distribution of the gas phase partial pressures is invoked, and the saturation concentration  $c_{l,*}$  in Eq. 4.5 was computed locally. However, because oxygen is in great excess, the value of  $c_{l,*}$  is practically constant at all positions in the reactor, consistent with the assumption used to compute  $k_L a$  from the experimental data.

**CHAPTER 5. CHARACTERISTIC TIME SCALES OF MIXING, MASS TRANSFER  
AND BIOMASS GROWTH IN A TAYLOR VORTEX ALGAL  
PHOTOBIOREACTOR**

Modified from the paper “Gao X, Kong B, Vigil RD. 2015. Characteristic time scales of mixing, mass transfer and biomass growth in a Taylor vortex algal photobioreactor. *Biores Technol* 198: 283-291.”

Recently it has been demonstrated that algal biomass yield can be enhanced using fluid flow patterns known as Taylor vortices. It has been suggested that these growth rate improvements can be attributed to improved light delivery as a result of rapid transport of microorganisms between light and dark regions of the reactor. However, Taylor vortices also strongly impact fluid mixing and interphase (gas–liquid) mass transport, and these in turn may also explain improvements in biomass productivity. To identify the growth-limiting factor in a Taylor vortex algal photobioreactor, experiments were performed to determine characteristic time scales for mixing and mass transfer. By comparing these results with the characteristic time scale for biomass growth, it is shown that algal growth rate in Taylor vortex reactors is not limited by fluid mixing or interphase mass transfer, and therefore the observed biomass productivity improvements are likely attributable to improved light utilization efficiency.

## 5.1. Introduction

Development of more efficient algal photobioreactors (PBRs) is driven by increasing interest in algaculture for the production of fuels, chemicals, food, animal feed, and medicine (Spolaore et al., 2006). Even for high-volume applications that require pond systems, such as the production of biofuels, PBRs play an important auxiliary role in maintaining pond cultures. Moreover, because of the better control of mixing and containment of growth media and feed gas offered by PBR systems, the prospect exists for using industrial CO<sub>2</sub> waste streams for cultivation of microalgae (Morweiser et al., 2010). Consequently, there is significant incentive to design and operate algal PBRs with high biomass productivity and conversion efficiency.

Many factors affect performance of PBRs, such as the type of PBR, culture media, temperature, pH, microorganism used, CO<sub>2</sub> mass transfer, O<sub>2</sub> accumulation, mixing, light intensity and light/dark cycles (Kumar and Das, 2012). Among these, the major limiting factors for growth of microalgae are usually light availability and interphase mass transfer. Light limitations caused by absorption and scattering can occur even in dilute cell cultures, depending upon the distance of the light path through the reactor and the intensity of the incident radiation (Hu and Richmond, 1996). Near the reactor irradiated surface, algal radiative exposure is usually adequate or in excess, whereas a dark volume with insufficient light for photosynthesis to occur often resides only a few centimeters or less from the irradiated surface, depending on the cell concentration (Kong and Vigil, 2014). For this reason, a key factor in the design of PBRs is the incorporation of mechanisms to periodically transport cells between light and dark regions of the reactor (mixing-induced light/dark

cycles) in order to efficiently utilize radiation near the illuminated reactor surface and distribute it evenly to microorganisms (Hu and Richmond, 1996, Ugwu et al., 2005, Sobczuk et al., 2006 and Huang et al., 2014).

Mixing induced light/dark (L/D) cycles usually occur at frequencies on the order of 1 Hz or less, which is significantly lower than the minimum frequencies required to produce the flashing light effect ( $>25$  Hz). Nevertheless, it has been demonstrated that photosynthesis can be enhanced by low frequency L/D cycles (Miller et al., 1964, Grobbelaar, 1994, Morweiser et al., 2010, Huang et al., 2014 and Takache et al., 2015). In flat-plate (Hu and Richmond, 1996 and Janssen et al., 2003), bubble column (Merchuk et al., 1998), and airlift bioreactors (Merchuk et al., 1998 and Degen et al., 2001), fluid transport between light and dark regions of the reactor occurs primarily via diffusive processes resulting from bubble-induced mixing, and consequently these reactors do not generate the characteristic L/D cycles required to more evenly distribute light to microorganisms (Liao et al., 2014). As a result, some conventional PBR designs incorporate foils or baffles to generate coherent L/D cycles (Degen et al., 2001, Ugwu et al., 2005 and Liao et al., 2014).

As an alternative approach for generating L/D cycles for culturing algae, Miller et al. (1964) used a Taylor–Couette device (fluid confined to the annulus between two concentric cylinders, with the inner cylinder rotating) to generate toroidal Taylor vortices that rapidly and reliably shuttle fluid between the poorly lit inner cylinder and the well-illuminated outer cylinder. Although they performed only short time scale experiments, they were able to demonstrate that the rate of photosynthesis (via oxygen measurements) increased with

increasing cylinder rotation speed, and they attributed these enhancements to increases in the L/D frequencies experienced by microorganisms.

More recently, Taylor vortex PBRs have been used to culture *Chlorella vulgaris* to very high concentrations in both batch (Kong et al., 2013) and continuous cultures (Kong and Vigil, 2013), and it has been demonstrated that the biomass yields are significantly greater than those obtained in the absence of Taylor vortices (i.e. an annular bubble column with no cylinder rotation). However, it should be noted that gas–liquid mass transport is also significantly enhanced by the presence of Taylor vortices (Ramezani et al., 2015), and as a result the question arises as to whether algal growth rate enhancements in these devices is attributable primarily to the creation of L/D cycles, to improved interphase mass transport of carbon dioxide and oxygen, or to a combination of both effects. Hence, the purpose of this report is to describe the findings of a series of batch culture experiments designed to determine characteristic times for liquid mixing, gas–liquid mass transfer, and algal biomass growth in a Taylor–Couette PBR for a range of reactor inner cylinder rotation speeds, feed gas flow rates, and feed gas compositions. As a result of these experiments, it can be concluded that improved light delivery is apparently the only plausible physical mechanism that can explain the enhanced algal growth rates observed in Taylor vortex PBRs.

## **5.2. Method**

### **5.2.1. Organism, media, and subculture**

All experiments were carried out using *C. vulgaris* (UTEX #265) grown in a modified M8-a medium having the composition described by Kliphuis et al. (2010). Subcultures were

maintained in 250-mL shake flasks at room temperature with an incident photon flux of 10–20  $\mu\text{mol m}^{-2} \text{s}^{-1}$  provided by compact fluorescent light bulbs, and agitated by a gas mixture of air enriched with 5% (molar) carbon dioxide. The culture medium was sterilized with a 0.22  $\mu\text{m}$  sterile filter after the pH was adjusted to a value of  $6.7 \pm 0.1$  by adding 2 N potassium hydroxide solution. In the Taylor vortex PBR, the solution pH depends upon the carbon dioxide gas–liquid equilibrium, and it was consistently measured during culture conditions to be in the range of 7.0–8.0. In all experiments reported here, the PBR was inoculated at cell dry biomass concentration of 0.067 g/L, as determined from optical density measurements.

### 5.2.2. Photobioreactor

A 3D rendering of the Taylor–Couette PBR used in this study can be found in Gao et al. (2015a), and a schematic diagram of the batch culture system is shown in Fig.5. 1. The fixed outer cylindrical reactor wall and surrounded heating jacket were constructed using transparent Plexiglas. The diameters of the rotating inner and fixed outer cylinders were 7.62 and 10.16 cm, respectively, resulting in an annular gap width of 1.27 cm. The length of the reactor (48 cm) provided an annular working volume of approximately 1.7 L. The stainless steel inner cylinder was rotated by a stepper motor (Applied Motion Products, STM24SF) mounted at the top of the reactor. Sterilization of the annular reaction chamber was achieved by filling it with a solution of 70% alcohol followed by rinsing with autoclaved deionized water. The reactor temperature was maintained at 37 °C by circulating water through the reactor jacket using a NESLAB Instruments EX-221 water bath circulator. The reactor was

enclosed along its length by four Hydrofarm eco-4441B flat light panels, each of which was comprised of four T5 fluorescent light tubes. The photosynthetic photon flux on the surface of the reactor (external surface of the heating jacket) was measured to be  $450 \mu\text{mol m}^{-2} \text{s}^{-1}$  using a LICOR LI-190 2 quantum sensor connected to a LI-250 light meter. The feed gas, consisting of a binary mixture of nitrogen and carbon dioxide (6–12 mol%  $\text{CO}_2$ ) at a total flow rate of 85–510 mL/min (0.05–0.30 vvm) was first passed through a sterile filter and then pumped into the reactor via four 40- $\mu\text{m}$  sureseal miniature mufflers (McMaster-Carr, type H) arranged symmetrically inside the bottom end cap of the reactor. The inlet gas flow rate of each gas component was controlled by digital gas flow controllers and the off-gas flow rate was measured using a gas flow meter. Further details concerning the apparatus and procedure can be found in Kong et al. (2013).

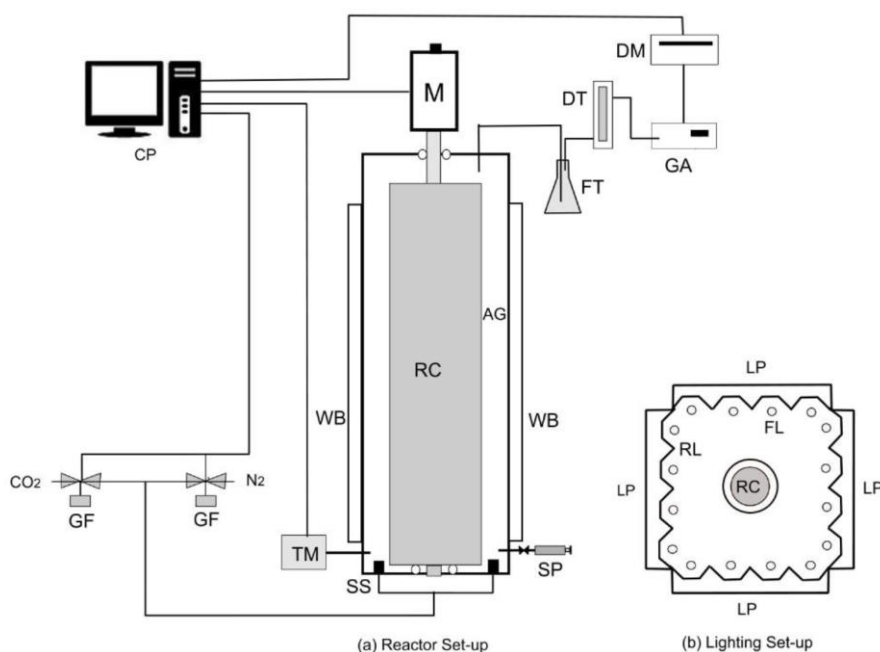


Figure 5.1. Schematic diagram of the batch culture and data acquisition system.

### 5.2.3. Experimental measurements

The mole fractions of carbon dioxide and oxygen in the off-gas were continuously measured and recorded throughout each experiment at 10 min intervals by passing the off-gas through a gas analyzer (Quantek Instruments, 902P, Grafton, MA) connected downstream of a desiccant purifier (Drierite, L68GP). The biomass concentration was monitored at 6–12 h intervals by extracting culture samples from the reactor using a syringe and measuring optical density. In addition, dry biomass was determined from 10 mL reactor broth samples that were centrifuged at 3400 rpm for 12 min, freeze-dried for 48 h, and weighed using a balance with 0.1 mg resolution. The relationship between optical density ( $OD_{680}$ ) and dry biomass ( $C_b$ ), as previously determined from hundreds of measurements in our earlier work (Kong et al., 2013 and Kong and Vigil, 2013), is well represented by the following correlation,

$$C_b (\text{g/L}) = 0.33OD_{680} \quad (R^2 = 0.997) \quad (5.1)$$

Because of the reliability of the above relation, dry biomass was not weighed at every sampling interval; in some instances biomass concentration was computed from optical density measurements, thereby reducing the culture volume loss during the course of an experiment.

Elemental composition (C, H, N and S) of dry biomass samples was determined using an elemental analyzer (Perkin Elmer 2100 Series II CHN/S Analyzer). Dry biomass samples were first freeze-dried for 48 h and subsequently heated in an oven at 65 °C for an additional 48 h to completely remove water before they were analyzed for composition. Three measurements were performed for each sample in order to improve accuracy. The mean elemental composition of the biomass produced under various experimental conditions

(cylinder rotation speed, gas feed rate and composition) was: 45.92% C, 7.46% H, 5.59% N and 0.67% S.

### 5.3. Calculation of characteristic time scales

#### 5.3.1. Rate controlling step

Transport of gas phase species such as oxygen and carbon dioxide to and from microorganisms in general involves several mechanistic steps including transit across a gas boundary layer to the gas–liquid interface, dissolution at the gas–liquid boundary, transit across a liquid boundary layer near the interface, convective liquid mixing, transit across a biofilm at the microorganism surface, and consumption/production in the microorganism itself (Kraakman et al., 2011). Commonly, the resistances in the gas film and in bulk liquid mixing are neglected, as these quantities are usually small compared to the resistances in liquid films at interface boundaries. In principle, the mass transfer coefficients for the gas–liquid interface ( $k_L$ ) and the biofilm ( $k_b$ ) both depend upon fluid flow in the reactor, but computational fluid dynamics calculations of the Kolmogorov length for typical conditions in a Taylor vortex reactor reveal that most algal microorganisms with characteristic sizes on the order of 10  $\mu\text{m}$  or less are too small to be sensitive to fluid shear, and as a result it is unlikely that  $k_b$  is impacted by the inner cylinder rotation speed (Thomas and Gibson, 1990). Therefore, it can be anticipated that changes in cylinder rotation speed affect interphase mass transport primarily through modulation of  $k_L$ .

In batch culture systems, which are inherently unsteady, the rate-limiting step may change with time. In such cases, it is useful to compare characteristic time scales for each

mechanistic step in order to identify the rate-limiting process. In this work we identify these time scales for liquid phase mixing ( $t_{\text{mix}}$ ) of dissolved  $\text{CO}_2$ , transport of  $\text{CO}_2$  across the liquid film at the gas–liquid interface ( $t_{\text{MT}}$ ), and consumption of  $\text{CO}_2$  by microorganisms, as reflected by the characteristic time for biomass growth ( $t_{\text{g}}$ ).

### 5.3.2. Characteristic mixing time

Fluid mixing behavior is characterized by a mixing time, which is defined as the time required to achieve a specific degree of homogeneity after a trace pulse has been injected into the reactor (Gavrilescu and Roman, 1996). In this work, the acid tracer method (Chisti, 1989 and Kumar and Das, 2012) was used to measure the mixing time. The annulus was first filled with room temperature deionized water. Subsequently nitrogen was pumped through sparge stones into the reactor for 10 min to purge dissolved carbon dioxide. Thereafter, 5 mL of 2 M HCl was added to the water to lower the pH to approximately 3.50 at steady state. The tracer (10 mL of 1 M KOH) was then rapidly injected into the bottom of the reactor using a syringe, and the temporal pH response inside the annulus was recorded using a pH probe located at the top of the reactor. The time required for the pH to attain a value within 5% of the final steady state value ( $t_{\text{tr}}$ ) was then determined from pH time series measurements.

The protocol described above provides a good representation of the time required for the reactor to achieve spatial homogeneity from an initial condition with maximal fluid segregation (tracer located as far as possible from the detector). However, as we are primarily interested in the transport of  $\text{CO}_2$ , this species enters the liquid growth medium not at a single source point far from the reactor exit but at many locations in the reactor via rapidly rising

gas bubbles. Furthermore, since it is well-known that fluid mixing within Taylor vortices is much more rapid than is the mixing between vortices (Campero and Vigil, 1997), it is more appropriate to estimate the fluid mixing time by normalizing the pH response measurements described above by the number of Taylor vortices present in the system. The latter quantity can be estimated by making use of the analytical result that the axial wavelength  $\lambda$  of a pair of vortices at the onset of Taylor vortex flow is given by  $\lambda=2(r_o-r_i)$ , where  $r_o$  and  $r_i$  are the radii of the inner and outer cylinders, respectively (Coles, 1965). Hence, the characteristic mixing time can be estimated as

$$t_{mix} = \frac{t_r(r_o - r_i)}{L} \quad (5.2)$$

where  $L$  is the fluid height in the reactor.

### 5.3.3. Characteristic gas–liquid mass transfer time

Neglecting gas film resistance, the instantaneous volumetric rate of gas–liquid mass transfer  $R_{MT}$  is given by

$$R_{MT} = k_L a (C_{CO_2}^* - C_{CO_2}) \quad (5.3)$$

where  $C_{CO_2}^*$  and  $C_{CO_2}$  are the dissolved  $CO_2$  concentrations in the liquid at the gas–liquid interface and in the liquid bulk, respectively. The characteristic mass transfer time,  $t_{MT}$ , is therefore given by

$$t_{MT} = \frac{1}{k_L a} \quad (5.4)$$

where  $k_L$  is the liquid side mass transfer coefficient and  $a$  is the specific interfacial area.

For an air–water system, the volumetric mass transfer coefficient for oxygen,  $k_L a(\text{O}_2)$ , in a vertically-oriented Taylor vortex PBR at room temperature can be computed from correlations recently developed by Ramezani et al. (2015), given by:

$$Sh = \frac{k_L a d_b^2}{D_L} = 2.9 \times 10^{-8} \text{Re}_a^{0.85} (\text{Re}_\theta + 1.9 \times 10^4)^{1.9} \quad (5.5)$$

$$\frac{d_b}{r_o - r_i} = 1.0 \times 10^{-5} \text{Re}_a^{0.11} (\text{Re}_\theta + 3.3 \times 10^4)^{0.91} \quad (5.6)$$

In the above equations  $Sh$  is the Sherwood number,  $d_b$  is the Sauter mean bubble diameter,  $D_L$  is the diffusivity of the solute in the liquid phase, and  $Re_a$  and  $Re_\theta$  are the axial and azimuthal Reynolds numbers defined as

$$Re_a = \frac{2u_G(r_o - r_i)}{\nu_L} \quad (5.7)$$

and

$$Re_\theta = \frac{\omega r_i (r_o - r_i)}{\nu_L} \quad (5.8)$$

The axial Reynolds number  $Re_a$  is based upon the hydraulic diameter and superficial gas velocity,  $u_G$ , and the azimuthal Reynolds number  $Re_\theta$  is based on the inner cylinder speed and annular gap width. Because the gas holdup in vertical gas–liquid Taylor vortex reactors is low ( $\approx 3\%$ ), the fluid kinematic viscosity is used in both definitions (Gao et al., 2015a). Experimental details concerning the development of the correlations given by Eqs. (5.5) and (5.6) can be found in Ramezani et al. (2015), who used a minimally invasive oxygen sensing system (PreSens Fibox 4 transmitter and Pst3 sensor spots) to measure time-dependent dissolved oxygen concentrations in response to step input changes.

From Eqs. (5.4), (5.5), (5.6), (5.7) and (5.8) it is possible to compute  $t_{MT}$  based upon the mass transfer coefficient for oxygen. The characteristic mass transfer time based upon the mass transfer coefficient for carbon dioxide can also be computed by making use of the Higbie theory (Higbie, 1935) to determine the relationship between  $k_L a(O_2)$  and  $k_L a(CO_2)$ :

$$k_L a(CO_2) = k_L a(O_2) \sqrt{\frac{D_{CO_2}}{D_{O_2}}} \quad (5.9)$$

where  $D_{CO_2}$  and  $D_{O_2}$  are the diffusivities of carbon dioxide and oxygen in water. Because the correlations presented in Eqs. (5.5) and (5.6) are based upon experiments carried out at room temperature, whereas the culture experiments described here were performed at 37 °C, it is necessary to make use of the following relationships to estimate the temperature dependence of the diffusion coefficients (Tamimi et al., 1994 and Han and Bartels, 1996):

$$\log_{10}(D_{CO_2}) = -2.047 - \frac{541.2}{T} - \left(\frac{275.7}{T}\right)^2 \quad (5.10)$$

And

$$\log_{10}(D_{O_2}) = -4.410 + \frac{773.8}{T} - \left(\frac{506.4}{T}\right)^2 \quad (5.11)$$

Hence, the characteristic  $CO_2$  mass transfer time in the experiments discussed here can be expressed as

$$t_{MT} = \frac{1}{k_L a(O_2, 298\text{ K})} \sqrt{\frac{D_{O_2}(298\text{ K})}{D_{CO_2}(310\text{ K})}} \quad (5.12)$$

where  $k_L a(O_2, 298\text{ K})$  can be determined from Eq. (5.5).

### 5.3.4. Characteristic biomass growth time

The characteristic biomass growth time  $t_g$  can be estimated by assuming that the growth rate has first order dependence on the dissolved CO<sub>2</sub> concentration, which is available at its equilibrium concentration  $C_{CO_2}^*$  (i.e. no transport limitations), leading to

$$t_g = \frac{C_{CO_2}^*}{Q_{CO_2}} \quad (5.13)$$

In the above equation,  $Q_{CO_2}$  is the volumetric uptake rate of CO<sub>2</sub> (g/L s) by the microorganisms, which can be determined by analyzing the composition and flow rate of the off gas and comparing it with the feed gas. Alternatively, the CO<sub>2</sub> uptake rate can be determined from the evolution of the dry biomass concentration provided that the biomass yield coefficient,  $Y_{CO_2}$  (biomass produced/CO<sub>2</sub> mass consumed), is known:

$$Q_{CO_2} = \frac{1}{Y_{CO_2}} \frac{dC_b}{dt} \quad (5.14)$$

The yield coefficient in the experiments carried out here is estimated to have the value  $Y_{CO_2} = 0.594$  based upon the elemental analysis of the dry biomass product described earlier. Hence, the characteristic biomass growth time can be expressed as (Doran, 1993):

$$t_g = \frac{Y_{CO_2} C_{CO_2}^*}{\mu C_b} \quad (5.15)$$

where  $\mu$  is the specific growth rate defined as

$$\mu = \frac{1}{C_b} \frac{dC_b}{dt} \quad (5.16)$$

The evolution of the biomass concentration using *C. vulgaris* in a batch-operated Taylor vortex PBR can be well represented by least-square fits of the logistic equation (Kong et al., 2013):

$$C_b = \frac{C_{b,\infty}}{1 + e^{-k(t-t_0)}} \quad (5.17)$$

where  $C_{b,\infty}$  is the asymptotic value of  $C_b$  at long times,  $k$  is a constant representing the maximal instantaneous growth rate (slope of the inflection point on the sigmoidal growth curve), and  $t_0$  is the time at which the maximal instantaneous growth rate occurs. Combining Eqs. (5.15), (5.16) and (5.17) leads to the following expression:

$$t_g = \frac{Y_{CO_2} C_{CO_2}^* (1 + e^{-k(t-t_0)})^2}{k C_{b,\infty} e^{-k(t-t_0)}} \quad (5.18)$$

In order to compute  $t_g$  using either Eq. (5.13) or (5.18), the  $CO_2$  equilibrium concentration,  $C_{CO_2}^*$ , must be known. This quantity can be estimated from Henry's law,

$$C_{CO_2}^* = \frac{y_{CO_2} P M_{CO_2}}{H_{CO_2}} \quad (5.19)$$

where,  $y_{CO_2}$  is the mole fraction of carbon dioxide in the feed gas,  $P$  is the total gas pressure,  $M_{CO_2}$  is the molecular weight of  $CO_2$ , and  $H_{CO_2}$  is the Henry coefficient for carbon dioxide. The dependence of the latter quantity on temperature for water is given by Sander (2015):

$$H_{CO_2} = 29.41 e^{-2400(\frac{1}{T} - \frac{1}{298})} \quad (5.20)$$

## 5.4. Results and discussion

### 5.4.1. Mixing time

Fig. 5.2 shows plots of the experimentally measured mixing time for different rotational speeds and gas flow rates. It is evident from these plots that the liquid mixing time, which ranged between approximately 10–30 s for the conditions shown in Fig. 5.2, decreases with increasing cylinder rotation speed as well as with increasing feed gas flow rate. These results

are consistent with those reported by Racina et al. (2010), who measured mixing time for single phase Taylor–Couette flow in a reactor with similar geometry as the device used in this work ( $r_i=3.79$  cm,  $r_o=5.0$  cm and  $L=39.0$ cm) using laser-optical methods.

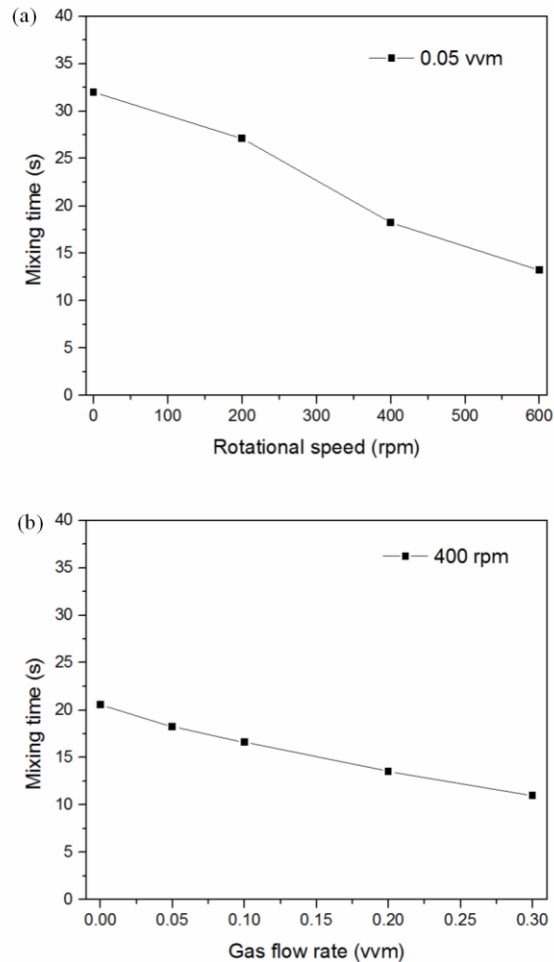


Figure 5.2. Mixing time,  $t_{\text{mix}}$ , as functions of (a) cylinder rotation speed and (b) gas flow rate. The same trends are observed independent of the choice of constant gas volumetric flow rate in (a) or constant cylinder speed in (b).

#### 5.4.2. Interphase mass transfer time

As was discussed previously, an empirical correlation (Eqs. (5.5), (5.6), (5.7) and (5.8)) for the oxygen volumetric mass transfer coefficient  $k_L a$  ( $\text{O}_2$ ) in a vertical Taylor vortex

reactor identical to the reactor used here was recently developed by Ramezani et al. (2015). By making use of this correlation and Eq. (5.9), plots for  $k_L a$  (CO<sub>2</sub>) were generated as functions of the cylinder rotation speed and gas flow rate for the algal culture conditions investigated here, as shown in Fig. 5.3. It is clear from these plots that  $k_L a$  (CO<sub>2</sub>) increases linearly with gas flow rate, whereas it has a more complicated dependence upon cylinder rotation speed. Below 300 rpm  $k_L a$  (CO<sub>2</sub>) is relatively insensitive to rotation speed, whereas it increases approximately linearly at higher rotation speeds. This phenomenon can be attributed to a shift in the relative importance of the contributions of gas–liquid slip velocity and turbulence dissipation rate to interphase mass transfer above 300 rpm, as is explained by Gao et al. (2015a). As was discussed earlier, the characteristic time for CO<sub>2</sub> gas–liquid mass transfer is simply the reciprocal of  $k_L a$ , and therefore based upon the plots in Fig. 5.3,  $t_{MT} \approx 1\text{--}8$  min, which is significantly greater than the values found for  $t_{mix}$ .

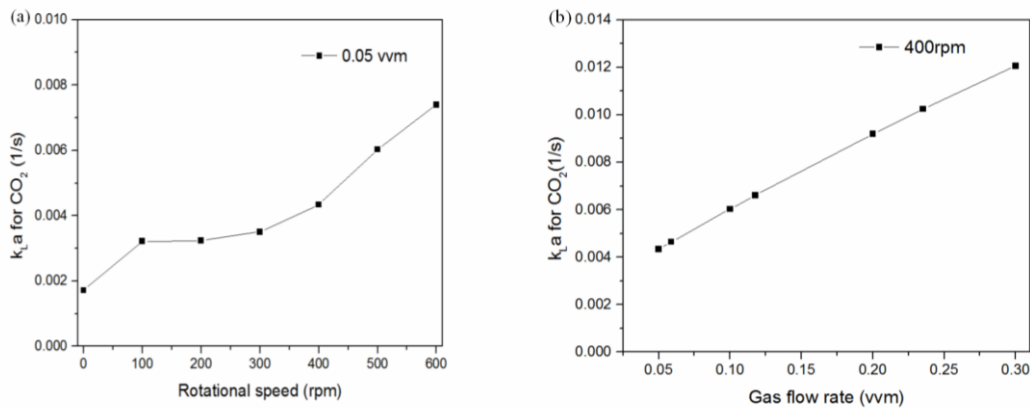


Figure 5.3. CO<sub>2</sub> volumetric mass transfer coefficient,  $k_L a$ , as functions of (a) cylinder rotation speed and (b) gas flow rate. The same trends are observed independent of the choice of constant gas volumetric flow rate in (a) or constant cylinder speed in (b).

Interphase gas–liquid mass transfer is also important with respect to oxygen, which is toxic to algal microorganisms if the O<sub>2</sub> dissolved concentration becomes too large. With respect to *C. vulgaris* in particular, Markl and Mather (1985) reported that saturation of the culture media using pure oxygen results in a dissolved oxygen concentration of 44.16 mg/L at 20 °C (475% of the value for the concentration observed in air-saturated water), which in turn reduces the photosynthetic rate by 35% in an open pond system. The level of oxygen accumulation in the liquid culture media depends on the hydrodynamic conditions and PBR design. It has previously been reported that commonly used bubble column and airlift PBRs operate at a maximum dissolved oxygen concentration of approximately 115% of the value for water saturated with air, whereas dissolved oxygen concentrations reach as high as 400% of the value for water–air saturation in horizontal tubular PBRs (Miron et al., 2002).

In contrast, Fig. 5.4 shows that even using a low gas flow rate, the maximum observed dissolved oxygen concentration, which occurs during periods of maximal photosynthetic activity, was only 90% of the water–air saturation value. As a result, it is reasonable to conclude that oxygen transport limitations do not inhibit algal growth in the Taylor vortex reactor experiments considered in this study.

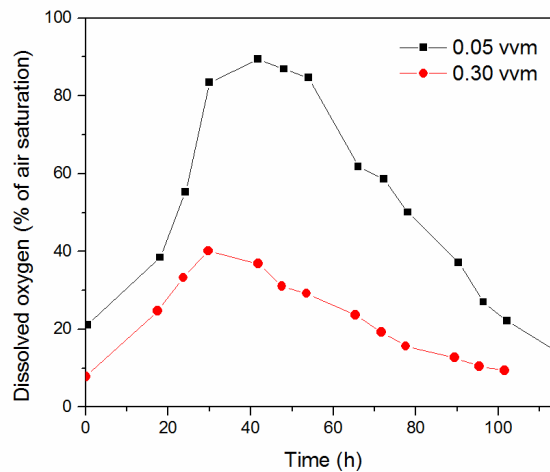


Figure 5.4. Experimental measurement of dissolved oxygen concentration in the Taylor vortex reactor as a percentage of water saturated with air at 20 °C. Inner cylinder rotation speed in both experiments was 400 rpm.

### 5.4.3. Biomass growth experiments

Although algal growth rate in a Taylor vortex PBR depends upon many factors other than fluid mixing and interphase mass transfer, such as choice of culture medium and temperature, here we limit our considerations to the effects of the two most important operational parameters for these devices, namely the inner cylinder rotation speed and the feed gas flow rate (Gao et al., 2015a). Both quantities strongly impact fluid flow patterns which in turn determine microorganism light exposure history (L/D cycles). In addition, a series of experiments was also carried out using constant gas volumetric flow rate but with different feed gas compositions. Biomass growth curves (and corresponding yield plots) showing the effects of cylinder rotation speed, gas flow rate, and gas composition are presented in Fig. 5.5.

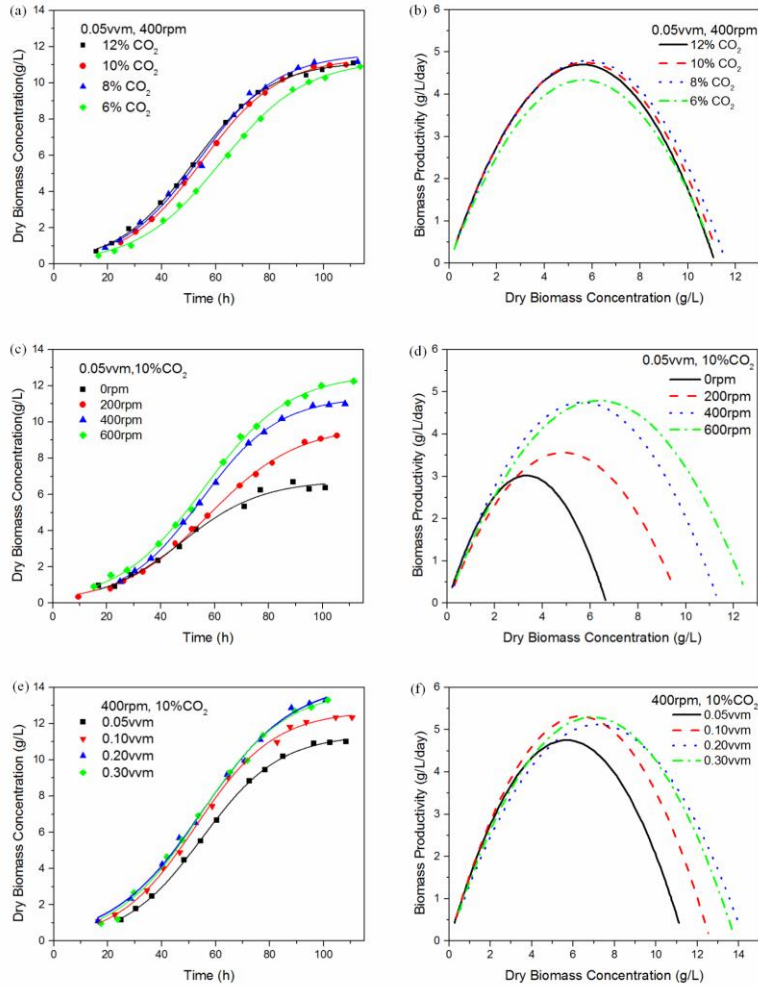


Figure 5.5. Dry biomass growth curves and yield plots showing the effect of gas composition (plots (a and b)), cylinder rotation speed (plots (c and d)), and gas flow rate (plots (e and f)).

In all experiments the biomass undergoes rapid initial growth followed by an approximately linear growth phase before leveling off at a maximum concentration of approximately 10–14 g/L at long times. These growth curves are typical of batch systems that must eventually become limited by supply of nutrients, and they can be well-approximated by the logistic Eq. (5.17) (best fits are shown as solid lines in Fig. 5.5). The instantaneous biomass yield can be computed by differentiating these best fit equations for biomass growth, i.e.  $\text{yield} = dC_b/dt$ , and these results are plotted as functions of the resident biomass

concentration (instantaneous yields are shown in units of days rather than hours by assuming 24 h of illumination/day) in Fig. 5.5(b), (d), and (f).

The plots in Fig. 4.5(a) and (b) demonstrate that the growth rate is insensitive to the feed composition when the CO<sub>2</sub> concentration is greater than 6%. As the feed concentration of CO<sub>2</sub> increases, the dissolved concentration of CO<sub>2</sub> should also increase according to Henry's law, provided that other factors remain unchanged. Because the total gas volumetric flow rate and cylinder rotation speed were fixed in the experiments depicted in Fig. 5.5(a), it is reasonable to assume that the fluid flow patterns are identical in all the experiments, and hence the lack of sensitivity of the growth curves to gas feed composition for CO<sub>2</sub> concentrations greater than 6% suggests that the growth rate is not limited by O<sub>2</sub> supply or interphase mass transport resistance for feed compositions with CO<sub>2</sub> concentrations greater than approximately 8%. In view of the fact that the mixing time  $t_{\text{mix}}$  was found to be significantly shorter than the interphase mass transfer time  $t_{\text{MT}}$ , any limitation in the biomass growth rate can only be attributable to limitations in light availability, nutrients other than CO<sub>2</sub>, or some other factor. Further evidence that growth is not limited by CO<sub>2</sub> supply for cases studied with feed CO<sub>2</sub> concentrations greater than 8% is provided by temporal data for the CO<sub>2</sub> uptake rate, which can be computed from measurements of the off-gas composition. Specifically, in the experiment carried out using a CO<sub>2</sub> feed composition of 6% nearly all of the fed CO<sub>2</sub> was consumed during the interval of time corresponding to the maximum biomass growth rate. In contrast, the maximum CO<sub>2</sub> uptake in cases using higher CO<sub>2</sub> feed concentrations ranges between approximately 60% and 90%.

Fig. 5.5(c) and (d) illustrate the effect of cylinder rotation speed for constant gas flow rate (0.05 vvm) and composition (10% CO<sub>2</sub>). Based upon Eq. (5.5), it is evident that increases in inner cylinder rotation speed lead to increases in the gas–liquid mass transfer coefficient. Furthermore, because the feed concentration of CO<sub>2</sub> used in these experiments was much greater than 6%, algal growth was not likely to be limited by CO<sub>2</sub> supply or mass transfer resistance for any of the rotation speeds studied, and therefore the growth rate dependence on cylinder rotation speed can only be attributed to some other factor that is sensitive to hydrodynamics. Having eliminated mixing and mass transfer as causes, the remaining explanation for these observations is that increases in inner cylinder speed produce higher frequency L/D cycles due to faster rotation of the toroidal vortices around a circular axis passing through their cores, and these higher frequencies improve light utilization efficiency (Kong et al., 2013).

The effect of feed gas volumetric flow rate on biomass growth rate was also considered, and the results are shown in Fig. 5.5(e) and (f) for constant cylinder rotation speed (400 rpm) and feed gas composition (10% CO<sub>2</sub>). Biomass growth rate is improved by increasing the feed gas flow rate from 0.05 vvm to 0.2 vvm, whereas further increases in the flow rate do not appear to have any impact on biomass growth. As has already been discussed, biomass growth rate in experiments using sufficiently high CO<sub>2</sub> concentrations in the feed gas is not limited by interphase mass transport, and hence the impact of increasing the gas flow rate must be explained in terms of fluid flow patterns and light delivery. In our previous work (Gao et al., 2015a), it was shown that centrifugal force concentrates gas bubbles near the inner cylinder. The accumulation of bubbles near the inner cylinder slightly reduces the radial

light path into the liquid growth medium by forcing the liquid to reside closer to the outer cylinder. It may also be possible that increases in gas flow rate (and consequently gas volume fraction near the inner cylinder) result in greater reflection of light off the inner cylinder wall and back into the liquid media. However, at higher gas flow rates Taylor vortices become significantly elongated (Gao et al., 2015a), and this may have an adverse effect on L/D cycle frequency, which may explain why further increases in gas flow rate do not result in enhanced biomass growth rates.

#### 5.4.4. Comparison of characteristic time scales

Evidence presented in the previous section suggests that neither fluid mixing nor gas–liquid mass transfer inhibit biomass growth in the Taylor vortex PBR. This view is further supported by computing the characteristic growth time using either Eq. (5.13) or (5.18) and comparing these with  $t_{\text{mix}}$  and  $t_{\text{MT}}$  over an extended time during a culture experiment. As was discussed previously, the computation of  $t_{\text{g}}$  assumes that dissolved  $\text{CO}_2$  is at its maximal (saturation) value of  $C_{\text{CO}_2}^*$ . As a result, the experimentally determined values for  $t_{\text{g}}$  depend primarily upon light delivery or nutrition limitations other than  $\text{CO}_2$ .

Fig. 5.6(a) and (b) depict the evolution of the three characteristic time scales discussed above, for two experimental conditions (although these results are typical for all experiments performed with sufficient  $\text{CO}_2$  supply in the feed gas). For the duration of both experiments, the characteristic growth time is one to two orders of magnitude greater than the mass transfer and mixing time scales. Hence, neither mass transfer of  $\text{CO}_2$  from gas bubbles to the liquid growth medium nor liquid mixing limit biomass growth in the Taylor vortex PBR.

Nevertheless, Fig. 5.5(c) demonstrates that algal growth rates can be enhanced by increasing the reactor inner cylinder speed. Since mass transport effects have been excluded as a cause for these growth rate enhancements, the remaining probable explanation is that increased cylinder rotation speeds lead to better light delivery to microorganisms through an increase in L/D cycle frequency.

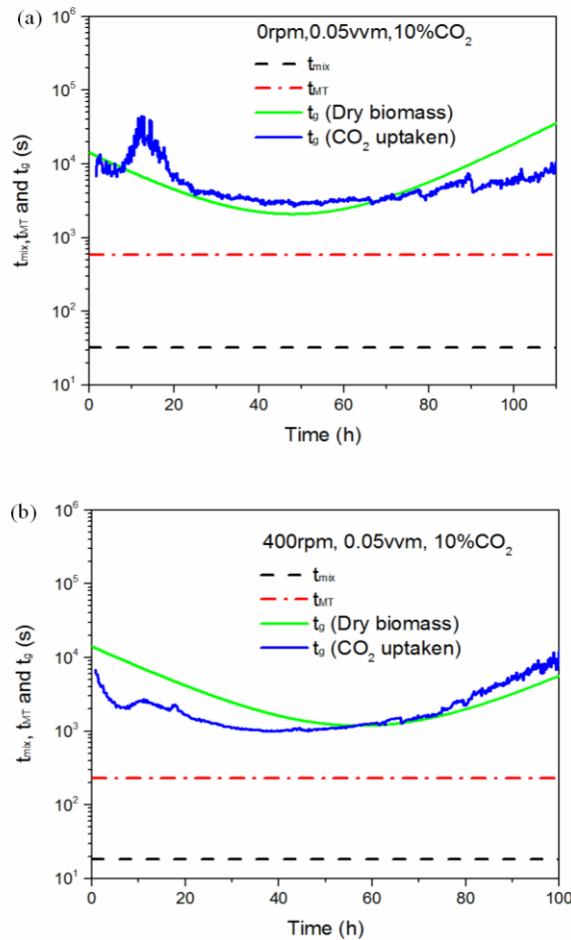


Figure 5.6. Characteristic time scales for mixing ( $t_{mix}$ ), mass transfer ( $t_{MT}$ ), and biomass growth ( $t_g$ ) plotted as a function of time for two typical *C. vulgaris* growth experiments. Two curves are shown for  $t_g$ , corresponding to calculations using Eqs. (5.13) and (5.18), respectively.

## 5.5. Conclusion

An analysis and comparison of time scales computed for three key mechanistic steps in the production of algal biomass, including gas–liquid mass transfer, liquid mixing, and algal growth, supports the conclusion that fluid flow patterns in these systems accelerate growth through improved light delivery to microorganisms rather than by improved delivery of carbon dioxide. The analysis presented here provides a guide for deconvoluting the effects of mixing, mass transfer, and light delivery for other PBR designs as well, and such information could be useful for optimizing PBR design and operation.

**CHAPTER 6. COMPREHENSIVE COMPUTATIONAL MODEL FOR COMBINING  
FLUID HYDRODYNAMICS, LIGHT TRANSPORT AND BIOMASS GROWTH IN A  
TAYLOR VORTEX ALGAL PHOTOBIOREACTOR: LAGRANGIAN APPROACH**

Modified from the paper “Gao X, Kong B, Vigil RD. 2016. Comprehensive computational model for combining fluid hydrodynamics, light transport and biomass growth in a Taylor vortex algal photobioreactor: Lagrangian approach. In press. Biores Technol.”

A comprehensive quantitative model incorporating the effects of fluid flow patterns, light distribution, and algal growth kinetics on biomass growth rate is developed in order to predict the performance of a Taylor vortex algal photobioreactor for culturing *Chlorella vulgaris*. A commonly used Lagrangian strategy for coupling the various factors influencing algal growth was employed whereby results from computational fluid dynamics and radiation transport simulations were used to compute numerous microorganism light exposure histories, and this information in turn was used to estimate the global biomass specific growth rate. The simulations provide good quantitative agreement with experimental data and correctly predict the trend in reactor performance as a key reactor operating parameter is varied (inner cylinder rotation speed). However, biomass growth curves are consistently over-predicted and potential causes for these over-predictions and drawbacks of the Lagrangian approach are addressed.

## 6.1. Introduction

In order to optimize the design and to reliably scale up photobioreactors, it is necessary to accurately simulate the complex interplay between physical, chemical and biological phenomenon that occur on multiple-time and length scales. For example, Figure 1 depicts some important relationships between hydrodynamics, mass transport, radiation transport, and algal growth kinetics. However, obtaining quantitatively accurate and reliable models for each of the fundamental processes governing global reactor performance can be challenging or computationally expensive. For example, accurate simulation of fluid mixing and mass transport requires at a minimum the use of validated gas-liquid fluid flow simulations. Accurate simulation of radiation transport in photobioreactors is also a difficult and computationally expensive endeavor for realistic geometries involving curved reactor walls (Kong and Vigil, 2014).

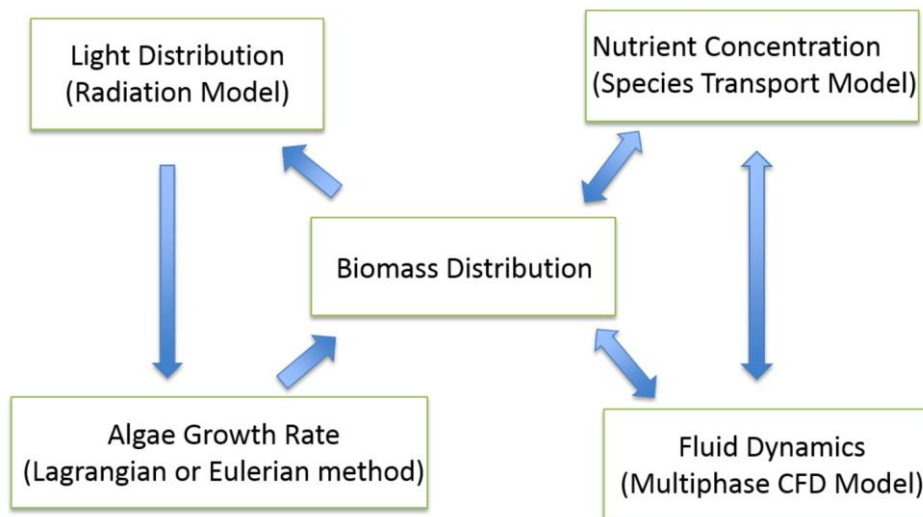


Figure 6.1. Coupling of fluid dynamics, radiation transport and algal growth kinetics.

In addition to challenges associated with developing suitable models for fluid flow, radiation transport, and microorganism growth, an efficient computational scheme for capturing the interplay between these processes is required. A comprehensive model should in principle account for all mutual interactions between these basic processes. However, several justifiable assumptions can significantly reduce computational costs, for example by neglecting the effect of biomass loading on hydrodynamics. However other phenomena, particularly insofar as they impact the amount and manner of light delivery to microorganisms, must be carefully simulated as irradiance of microorganisms is known to be the most critical factor affecting photobioreactor performance. Specifically, fluid mixing patterns that shuttle microorganisms periodically between light and dark regions of the reactor can substantially enhance both biomass productivity and light utilization efficiency (Hu and Richmond, 1996; Ugwu *et al.*, 2005; Sobczuk *et al.*, 2006; Kong *et al.*, 2013). Consequently, the essential elements of a comprehensive model of photobioreactor performance should include (a) accurate prediction of radiation distribution in the reactor as a function of biomass concentration, (b) a photosynthetic growth model that accounts for temporal variations in light exposure experienced by microorganisms, and (c) a hydrodynamic model capable of accurately predicting flow patterns, mixing, and the spatial trajectories of microorganisms.

The most common approach for integrating hydrodynamic, radiative, and kinetic growth models to predict global reactor behavior is to (1) compute velocity fields in the reactor, (2) compute microorganism spatial trajectories (Lagrangian particle tracking), (3) generate temporal light exposure trajectories by mapping microorganism position-time data to

predictions for the photon flux obtained from a radiation model, and (4) use light exposure trajectories to integrate an algal biomass kinetic growth equation. However, as has been demonstrated by Pruvost *et al.* (2008), such an approach requires that the Lagrangian particle tracks be consistent with a spatially uniform distribution of biomass for consistency with energy conservation. Although the use of the Lagrangian simulation approach in the present study is not novel, computations described here were carried out using detailed and experimentally validated hydrodynamic and radiative transport models applied to a reactor with more complex hydrodynamics and distribution of radiative flux (Taylor vortex algal photobioreactor) than is found in more familiar flat panel or tubular reactors. Furthermore, predictions for reactor performance are compared with experimental data, and weaknesses of the Lagrangian simulation approach are explored.

## 6.2. Comprehensive Reactor Model

### 6.2.1. Gas-Liquid Two-Phase Flow CFD Model

In this work, our previously validated two-fluid flow model was used to simulate multiphase flow dynamics in a Taylor vortex reactor (Gao *et al.*, 2015a; 2015b; Gao *et al.*, 2016a). Microalgal growth in this high biomass concentration system is not limited by gas-liquid interphase mass transfer, and therefore no interphase mass transfer model is required (Gao *et al.*, 2015c; Ramezani *et al.*, 2015). The axisymmetric equations of continuity and conservation of momentum equations are given by:

$$\frac{\partial}{\partial t}(\alpha_k \rho_k) + \nabla \cdot (\alpha_k \rho_k \vec{u}_k) = 0 \quad (6.1)$$

$$\frac{\partial}{\partial t}(\alpha_k \rho_k \vec{u}_k) + \nabla \cdot (\alpha_k \rho_k \vec{u}_k \vec{u}_k) = -\alpha_k \nabla p + \nabla \cdot (\overline{\overline{\tau}}_k + \overline{\overline{\tau}}_k^{Re}) + \alpha_k \rho_k \vec{g} + \vec{F}_{Ik} \quad (6.2)$$

Here,  $\alpha_k$  and  $\vec{u}_k$  are the phase volume fraction and the phase velocity for liquid ( $k = l$ ) and gas ( $k = g$ ), respectively. The phase stress and Reynolds stress tensors are represented by  $\overline{\tau}_k$  and  $\overline{\tau}_k^{\text{Re}}$ . The liquid-gas momentum exchange term,  $\vec{F}_{lg}$  can be decomposed into five independent interphase forces: drag, lift, virtual mass, wall lubrication, and turbulent dispersion forces. The interested reader can find expressions for the constitutive relations and model parameters in Gao *et al.* (2015b).

### 6.2.2. Lagrangian Particle Tracking Simulations

The photosynthesis rate depends on cell light exposure history which in turn depend upon microorganism spatial trajectories and light distribution. A Lagrangian particle tracking model coupled with the gas-liquid CFD model described above was employed to compute thousands of cell trajectories by integrating Newton's law for random cell initial positions. The equation of motion for microorganisms in the reactor could in general include many interphase forces such as drag, buoyancy, virtual mass and lift. However, due to the small characteristic size ( $\sim 5 \mu\text{m}$ ) of the microorganism considered in this work (*Chlorella vulgaris*), the drag force is dominant so that particle trajectories can be computed by integrating the following equations:

$$m_p \frac{d\vec{u}_p}{dt} = \vec{F}_D \quad (6.3)$$

$$\frac{d\vec{X}_p}{dt} = \vec{u}_p \quad (6.4)$$

The drag force  $\vec{F}_D$  can be expressed as (Schiller and Naumann, 1935):

$$\vec{F}_D = \frac{\pi d_p^2}{8} \rho_l C_D |\vec{u}_l - \vec{u}_p| (\vec{u}_l - \vec{u}_p) \quad (6.5)$$

where the drag coefficient  $C_D$  is given by

$$C_D = \begin{cases} \frac{24}{\text{Re}_p} (1 + 0.15 \text{Re}_p^{0.687}) & \text{Re}_p \leq 1000 \\ 0.44, & \text{Re}_p > 1000 \end{cases} \quad (6.6)$$

Note that the drag force exerted on algal cells depends upon the turbulent continuous liquid phase velocity  $\vec{u}_l$ . This quantity can be decomposed into time-averaged and fluctuating components, such that

$$\vec{u}_l = \overline{\vec{u}_l} + \vec{u}'_l \quad (6.7)$$

where  $\vec{u}'_l$  is the fluctuating liquid eddy velocity given by

$$\vec{u}'_l = \xi_i \sqrt{\frac{2k}{3}} \quad (6.8)$$

Here  $k$  is the turbulence kinetic energy and  $\xi_i$  is the zero mean unit variance Gaussian random value. Particles (algal cells) remain under the influence of the eddy until either (1) the integration time exceeds the eddy life time ( $t_e$ ), or (2) the distance between the center of an eddy and a particle exceeds the eddy length ( $L_e$ ). In the eddy lifetime model the particle interaction time ( $t_i$ ) is assumed to be equal to the smaller of the eddy lifetime and the eddy crossing time and is given by

$$t_i = \min(t_e, t_c) \quad (6.9)$$

When this time is reached, a new value of the instantaneous velocity is obtained by applying a new value of  $\xi_i$ . The characteristic lifetime and length scale of an eddy can be estimated as (Gosman and Loannides, 1983):

$$t_e = C_e \frac{k}{\epsilon}, \quad L_e = t_e |\vec{u}'_l| = C_e \sqrt{\frac{3}{2}} \frac{k^{3/2}}{\epsilon} \quad (6.10)$$

where the constant  $C_e$  is typically assumed to be in the range 0.2-0.56 (Yeoh and Tu, 2010).

In this work,  $C_e$  was taken as 0.3. The particle eddy crossing time is given by (Gosman and Loannides, 1983):

$$t_c = -\tau_p \ln \left[ 1 - \left( \frac{L_e}{\tau_p |\vec{u}_l - \vec{u}_p|} \right) \right] \quad (6.11)$$

where the particle relaxation time is given by:

$$\tau_p = \frac{4\rho_p d_p}{3\rho_l C_D |\vec{u}_l - \vec{u}_p|} \quad (6.12)$$

### 6.2.3. Algal Biomass Growth Model

Most dynamic biological models having the ability to incorporate the effects of light gradients and light/dark exposure cycles are based on the photosynthetic unit (PSU) construct which envisions light absorbing reaction centers in microorganisms occupying various states and considers transitions between these states (Eilers and Peeters, 1993; Camacho Rubio *et al.*, 2003; García-Camacho *et al.*, 2012, Nikolaou *et al.*, 2015). The Eilers-Peeters model, as revised by Wu and Merchuk (2001), was employed here to simulate microalgal growth rates. This 3-state model considers PSUs to be in either a resting, active, or inhibited state as shown in Figure 2 (a). The kinetic expressions used to describe the evolution of the distribution of PSUs in the three states are given by (Wu and Merchuk, 2001):

$$\frac{dx_1}{dt} = -\alpha I x_1 + \gamma x_2 + \delta x_3 \quad (6.13a)$$

$$\frac{dx_2}{dt} = \alpha I x_1 - \gamma x_2 - \beta I x_2 \quad (6.13b)$$

$$x_1 + x_2 + x_3 = 1 \quad (6.14)$$

$$\mu = k\gamma x_2 - M \quad (6.15)$$

In the above equations,  $x_1$ ,  $x_2$ , and  $x_3$  represent the fractions of PSUs occupying the resting, active, and inhibited states, respectively. The instantaneous photon flux received by

microalgae is given by  $I$ . The remaining parameters  $\alpha$ ,  $\beta$ ,  $\gamma$ ,  $\delta$ , and  $k$  are in general both species and temperature-dependent. The specific growth rate is given by  $\mu$ , and  $M$  is the maintenance coefficient describing requirements for internal metabolism and allowing for negative growth in low light conditions (Papáček *et al.*, 2014). By sampling thousands of cell light history trajectories and integrating Eqs. (6.13)-(6.15), the reactor mean specific growth rate  $\bar{\mu}$  can be estimated and used to compute the instantaneous dry biomass concentration provided that the system is only limited by light and not by nutrients so that

$$\frac{dC_b}{dt} = \bar{\mu}C_b. \quad (6.16)$$

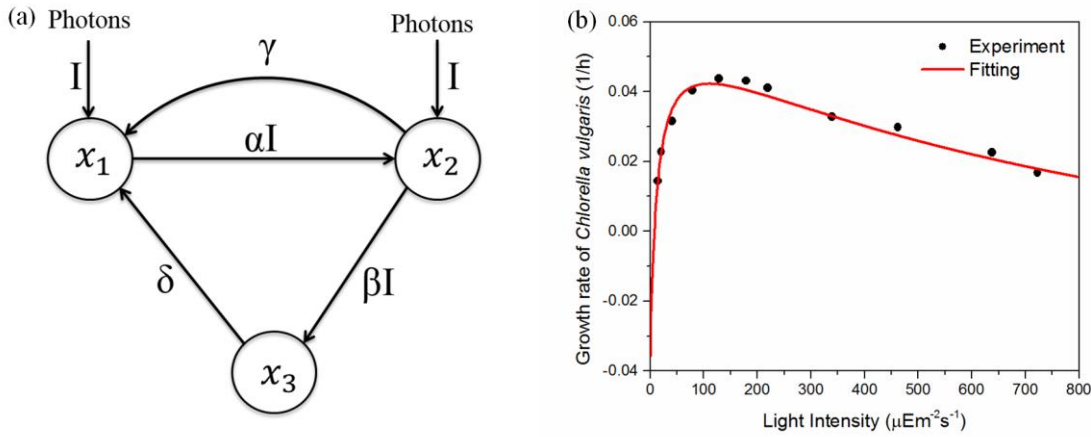


Figure 6.2. (a) Structure of the three state PSU model first proposed by Eilers and Peeters (1993). (b) Comparison of fitted specific growth rate with experimental data of Dauta *et al.* (1990).

#### 6.2.4. Radiative Transport Simulation

In previous work, Kong and Vigil (2014) developed and validated a numerical solution of the following radiative transport equation:

$$\frac{dI_\lambda(\vec{r}, \vec{s})}{ds} = (a_\lambda + \sigma_{s,\lambda})I_\lambda(\vec{r}, \vec{s}) = \frac{\sigma_{s,\lambda}}{4\pi} \int_0^{4\pi} I_\lambda(\vec{r}, \vec{s}')\Phi_\lambda(\vec{r}, \vec{s}')d\Omega' \quad (6.17)$$

In the above expression,  $I_\lambda$  is the wavelength-dependent radiance,  $\vec{r}$  is the position vector,  $\vec{s}$  is the ray direction vector,  $\vec{s}'$  is the scattering direction vector,  $s$  is the path length,  $a_\lambda$  is the wavelength-dependent absorption coefficient,  $\sigma_{s,\lambda}$  is the wavelength-dependent scattering coefficient,  $\Phi_\lambda$  is the wavelength-dependent phase function and  $\Omega'$  is the solid angle. All modeling methods and parameters used here were identical to those reported by Kong and Vigil (2014), who applied their model to the same concentric cylinder geometry. It should be noted that the model assumes (1) algal cell concentration is uniformly distributed in the annular reaction zone and (2) the effect of gas bubbles on radiation distribution can be neglected. As will be discussed in sections 6.4, gas-liquid CFD simulations provide some justification for both of these assumptions.

### 6.2.5. Model Component Coupling Method

The overall strategy (depicted in Figure 6.3) for computing biomass growth curves in photobioreactors includes performing CFD and particle tracking simulations to obtain spatial particle trajectories, computing spatial light distribution in the reactor by numerically solving Eq. (6.17), and lastly computing algal growth rate using Eqs. (6.13-6.16).

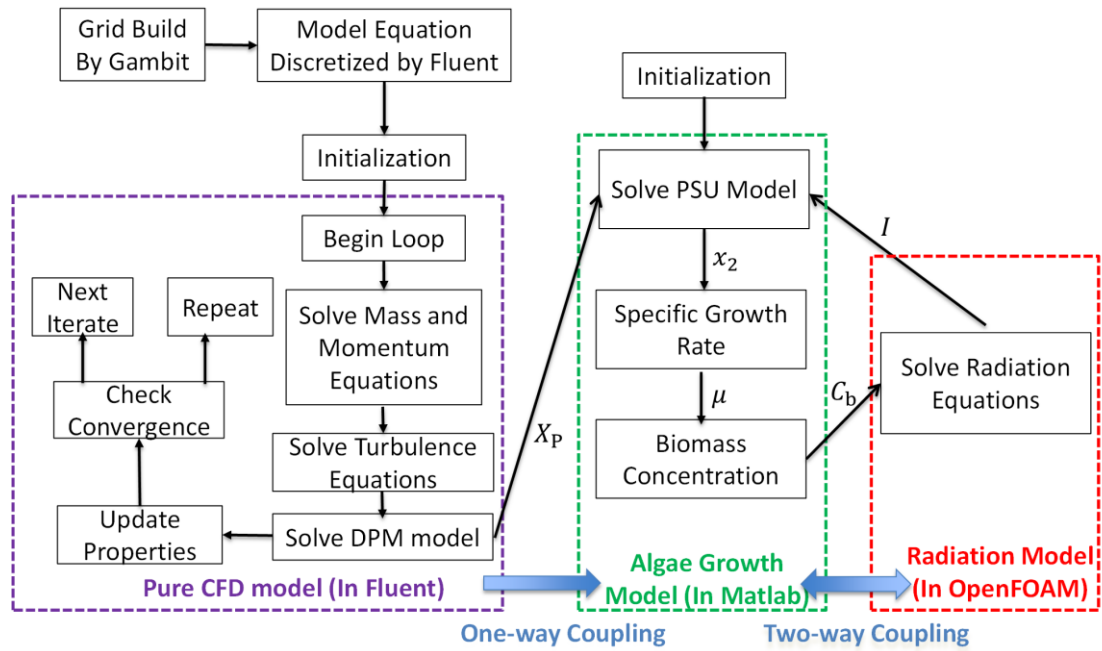


Figure 6.3. Schematic diagram of multi-timescale coupling method for Lagrangian simulation approach.

### 6.3. Computational Details

#### 6.3.1. Growth rate model parameters

The PSU model parameters that appear in Eqs. (6.13) -(6.15) are species specific, and have not previously been reported for *Chlorella vulgaris*, which is the organism used to generate experimental data for comparison with our model predictions. Consequently, experimental data obtained by Dauta *et al.* (1990), who investigated the growth rate of *Chlorella vulgaris* over a wide range of light intensities was used to fit the PSU model parameters using the method developed by Wu and Merchuk (2001). Figure 6.2 (b) shows the results of this fitting procedure and demonstrates that PSU model predictions compare favorably with experimental data for growth of *Chlorella vulgaris* at 35 °C. The fitted

parameters are as follows ( $R^2=0.9685$ ):  $\alpha = 7.253 \times 10^{-4} \text{ m}^2/(\mu\text{E})$ ,  $\beta = 1.703 \times 10^{-8} \text{ m}^2/(\mu\text{E})$ ,  $\delta = 9.968 \times 10^{-6} \text{ s}^{-1}$ ,  $\gamma = 0.009485 \text{ s}^{-1}$ ,  $k = 0.004511$ ,  $M = 9.913 \times 10^{-6} \text{ s}^{-1}$ .

### 6.3.2 Algebraic Representation of Light Distribution

Rather than generating new solutions to the computationally demanding radiative transfer equation (6.17) at each time step of the simulation, an algebraic expression to represent the photon flux was developed by fitting various trial function to numerical solutions of the general radiative transport equation (6.17) for several biomass loadings (0.25, 0.5, 1.0, 2.0, and 4.0 g/L). By finding a suitable algebraic expression in this manner, the photon flux can be accurately interpolated for any radial position and biomass concentration. After testing many functions, the following expression was found to closely approximate computed photon flux distributions in the Taylor vortex reactor:

$$I = I_o \exp \left[ (aC_b + b) \frac{r}{r_o} + c \right] \left( \frac{r}{r_o} \right)^{dC_b + e} \quad (6.18)$$

Here,  $I_o = 592.7 \mu\text{E}/\text{m}^2\cdot\text{s}$ ,  $r_o$  is the outer cylinder radius,  $C_b$  is the dry biomass concentration (g/L),  $r$  is radial position (m), and best fit ( $R^2 = 0.9981$ ) values for the parameters in Eq. (6.18) are given by  $a = -0.02431 \text{ L/g}$ ,  $b = 8.234$ ,  $c = -8.351$ ,  $d = 19.22 \text{ L/g}$ ,  $e = -9.567$ .

### 6.3.3. Taylor Vortex Photobioreactor

A schematic of the Taylor vortex photobioreactor used to culture *Chlorella vulgaris* is depicted in Figure S1. Details concerning experimental measurements can be found in Gao *et al.* (2015c). The rotating inner cylinder has a radius of 3.81 cm and the fixed transparent acrylic outer cylinder has an inner radius of 5.08 cm, resulting in a gap width of 1.27 cm. The length of the reactor is 50.8 cm and the reactor is filled to a height of  $h = 48 \text{ cm}$ , producing a

total liquid working volume of 1.70 L. The density and viscosity of the culture media are  $1036 \text{ kg/m}^3$  and  $7.22 \times 10^{-4} \text{ kg/m}\cdot\text{s}$ , respectively. The density of algal cells was taken to be identical with the culture media, and the mean cell diameter is  $5 \text{ }\mu\text{m}$ .

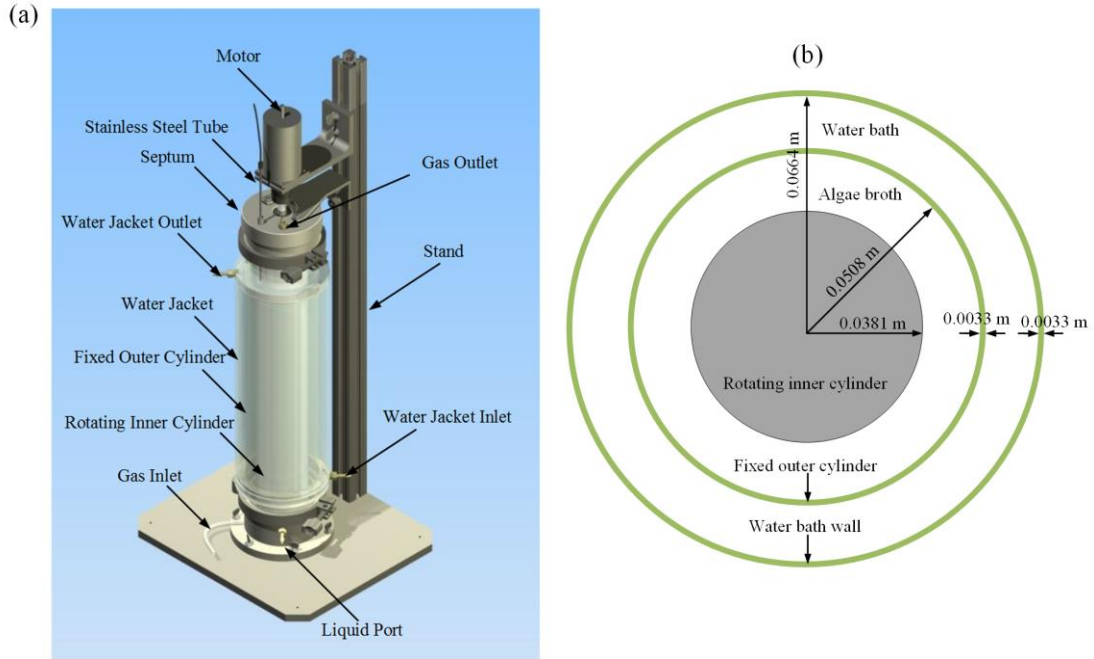


Figure 6. S1. (a) Taylor vortex bioreactor used for biomass cultivation. (b) Cross-section of the Taylor vortex bioreactor.

To carry out quasi-three-dimensional axisymmetric CFD simulations of flow in the Taylor vortex photobioreactor, a non-uniform rectangular mesh was employed to discretize the annular reaction zone. In previous work simulating mass transfer in the same reactor, three progressively finer meshes were tested and it was found that a mesh size of  $32 \times 480$  (radial  $\times$  axial grid points) is sufficient to capture the essential features of the flow (Gao *et al.*, 2015a). However, in this work the distribution of light is also important and at high biomass concentrations the photon flux drops dramatically with radial distance from the illuminated reactor surface. Hence, refinements to the hydrodynamic computational mesh

were considered to better capture the effect of steep light gradients on algal growth. Specifically, a mesh size of  $64 \times 960$  was employed, but since the resulting biomass concentration predictions using the finer mesh were nearly identical to those obtained using the  $32 \times 480$  mesh, it was decided that no further mesh refinements were necessary.

Boundary conditions used to carry out CFD calculations were as follows. For gas and liquid phases, no-slip conditions were specified at wall boundaries and the azimuthal velocity of the inner cylinder was chosen to match experimental conditions. The inlet gas flow rate was 85 mL/min, also in accordance with the experiments. Pressure outlet boundary conditions were used for all fluid phases.

The commercial finite volume CFD code, ANSYS FLUENT 14.5 (Ansys Inc., US) was used to solve the hydrodynamic equations. Transient CFD simulations were performed using an integration time step of  $5 \times 10^{-4}$  s. While typical algal growth experiments had a duration of approximately 120 hours, it is neither practical nor necessary to perform CFD simulations for that time period. Instead, fluid flow simulations were performed until fluid flow statistics reached steady values. Subsequently, particle trajectories were carried out for 10 seconds of real time.

Numerical integration of Eq. (6.16) to compute the reactor biomass concentration was performed using a time step  $\Delta t = 0.05$  s. This value is much smaller than the characteristic light/dark cycle time scale. The initial biomass concentration was set to the initial condition in the experiments (0.1 g/L), and the initial values of the fractions of the three metabolic states were estimated to be similar to those found in the subculture used to seed the reactor. This subculture was under a photon flux density of  $20 \mu\text{E}/\text{m}^2 \cdot \text{s}$ , and values for the fractions of

PSUs in each of these three states was estimated from steady-state solution of Eqs. (6.13) and (14) to be  $x_1 = 0.3874$ ,  $x_2 = 0.5924$ ,  $x_3 = 0.0202$ . Hence, very few PSUs are in the inhibited state at the start of the simulation.

## 6.4. Results and Discussion

### 6.4.1. Flow Hydrodynamics

Example contour plots for instantaneous simulated liquid phase stream function and gas volume fraction are shown in Figure 6.4 for typical Taylor vortex photobioreactor operating conditions with an inner cylinder rotation speed of 400 rpm and air flow rate of 0.05 vvm (85mL/min). It is obvious from Figure 6.4 (a) that toroidal vortices are formed in the narrow annular gap, wherein fluid circulates between the inner and outer cylinder walls. Because algal cells have a small Stokes number, they closely follow liquid phase streamlines and are rapidly and periodically shuttled between the relatively well illuminated regions near the outer cylinder and darker regions near the inner cylinder – a phenomenon that leads to improved light utilization and biomass growth rate (Miller *et al.*, 1964; Kong *et al.*, 2013).

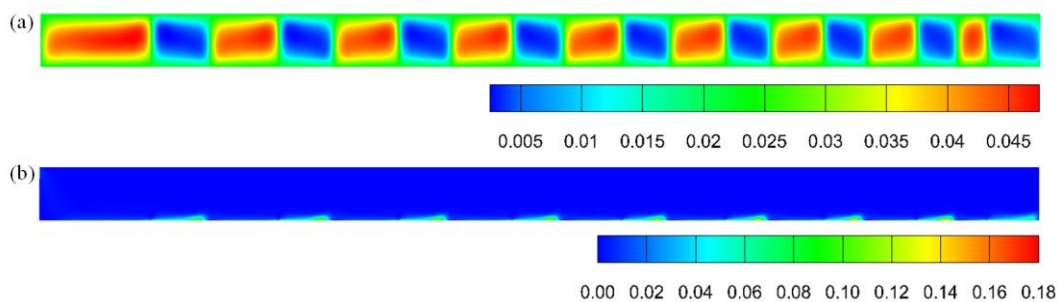


Figure 6.4. Contour plot of (a) stream function of the liquid phase (kg/s) and (b) bubble volume fraction distribution at rotational speed of 400 rpm. In each plot, the inner cylinder wall is represented by the bottom boundary and the outer cylinder wall is represented by the top boundary. In order to better show the results, the reactor length was scaled to half of the original length.

Figure 6.4 (b) clearly demonstrates that gas bubbles (confirmed visually in experiments) preferentially distribute near the dark inner cylinder wall due to centrifugal forces. This observation, in tandem with the fact that the gas volume fraction in the reactor is very low (< 2%), suggests that in this apparatus bubbles have negligible effect on radiation transport, as the small bubble volume resides in regions of the reactor where very little light is present. Hence, the assumption that the presence of gas bubbles can be neglected in the numerical solution of the radiative transport equation (6.17) is well justified.

#### 6.4.2. Particle Trajectory and Light Exposure History

Figures 6.5 (a) – (c) depict typical time series plots of algal cell radial position for different inner cylinder rotation speeds, as computed from the Lagrangian particle tracking model described previously. Increases in cylinder rotation speed produce more rapid shuttling of cells between the inner and outer cylinders by Taylor vortices as demonstrated by Figures 6.5 (d) – (f). Specifically, it can be seen that when the boundary between light and dark regions of the reactor is located at the middle of the annular gap  $(r - r_i) / (r_o - r_i) = 0.5$ , histograms of the resulting light/dark cycle frequencies have mean values of 1.1 Hz, 2.2 Hz and 3.2 Hz for 200 rpm, 400 rpm and 600 rpm, respectively. It is worth noting that these mixing-induced light/dark frequencies are significantly higher than those produced in many commonly used photobioreactors (Janssen *et al.*, 2000; Pruvost *et al.*, 2002; Huang *et al.*, 2014; Olivieri *et al.*, 2015).

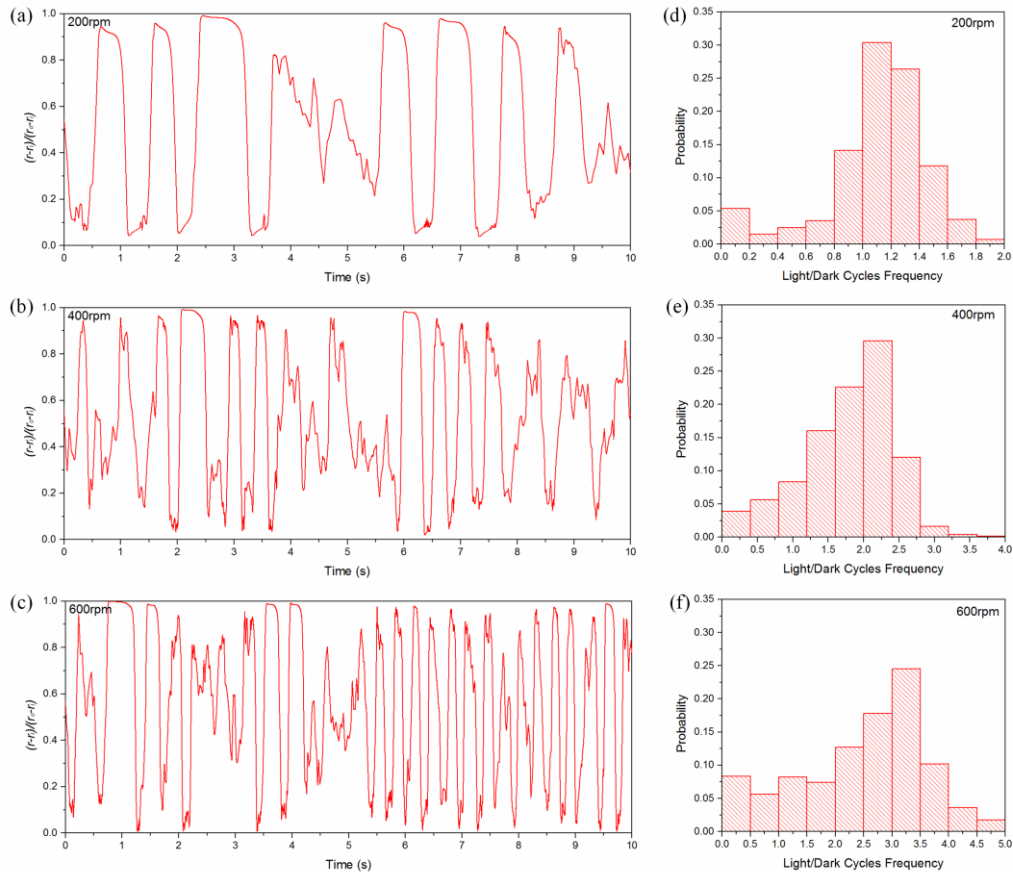


Figure 6.5. (a)-(c): Example radial position tracks for an algal cell at various reactor rotational speeds. (d)-(f): Light/dark cycle frequency at various reactor rotational speeds and for the specific condition when the light/dark boundary is located at normalized radial position  $(r - r_i) / (r_o - r_i) = 0.5$ .

Figures 6.6 (a) – (c) show the effect of biomass loading on cell light exposure for a fixed cylinder rotation speed. In the reactor geometry considered here, a low biomass concentration such as that used to produce Fig. 6.6 (a) results in relatively small variations in photon flux and no dark zone is observed. At higher biomass concentrations, e.g. 1 g/L as shown in Fig. 6.6 (b), the minimum photon flux experienced by microorganisms is nearly zero (dark zone) when cells approach the inner cylinder wall. Further increases in biomass concentration cause

the boundary between light and dark regions of the reactor to shift towards the outer cylinder wall, as is demonstrated by Fig. 6.6 (c).

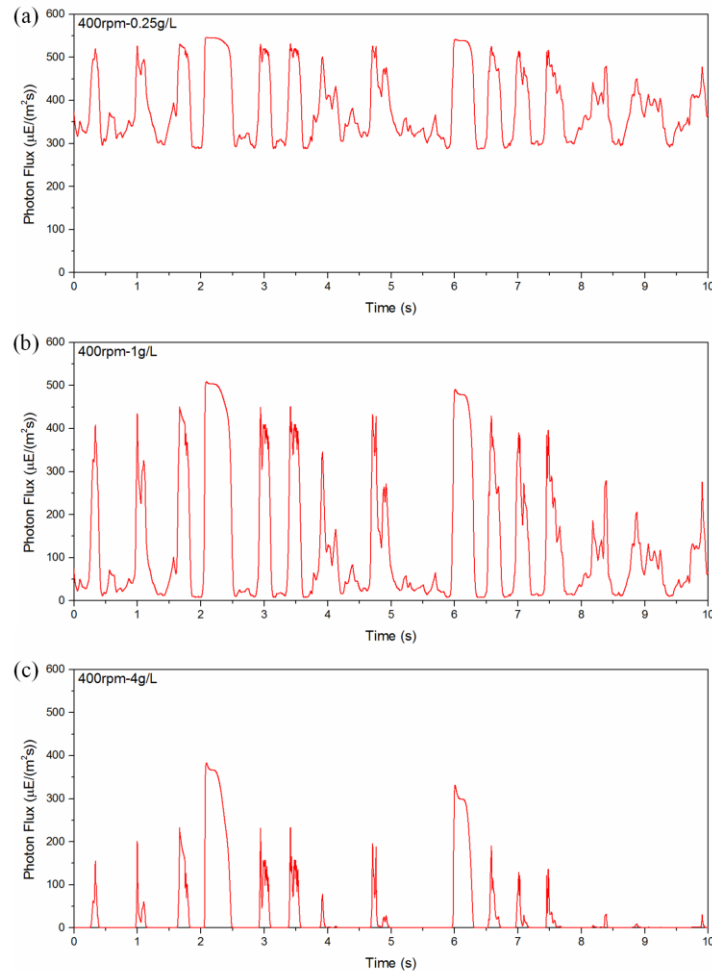


Figure 6.6. Light history of a typical algal cell at various biomass concentrations and for a fixed reactor rotational speed of 400 rpm. (a) 0.25g/L (b) 1 g/L (d) 4 g/L.

### 6.4.3. Biomass Growth Curves

Simulated Taylor vortex reactor biomass growth curves are compared with corresponding experimental data for three inner cylinder rotation speeds in Figure 6.7. The dry biomass concentration was compared instead of cell number density, as the real number of cells is several order larger than that can be tracked. The simulations correctly predict the

experimental trend of more rapid growth with increasing inner cylinder rotation speed, but in all cases biomass concentration is over-predicted by as much as 30% at longer culture times. For growth times less than approximately 60 hours, simulation predictions largely match the observed biomass concentration. As one would expect, both the simulations and the experiments show no significant effect of rotation speed on biomass growth curves when biomass concentration is sufficiently small so that no dark volume is present (Fig. 6.6 (c)).

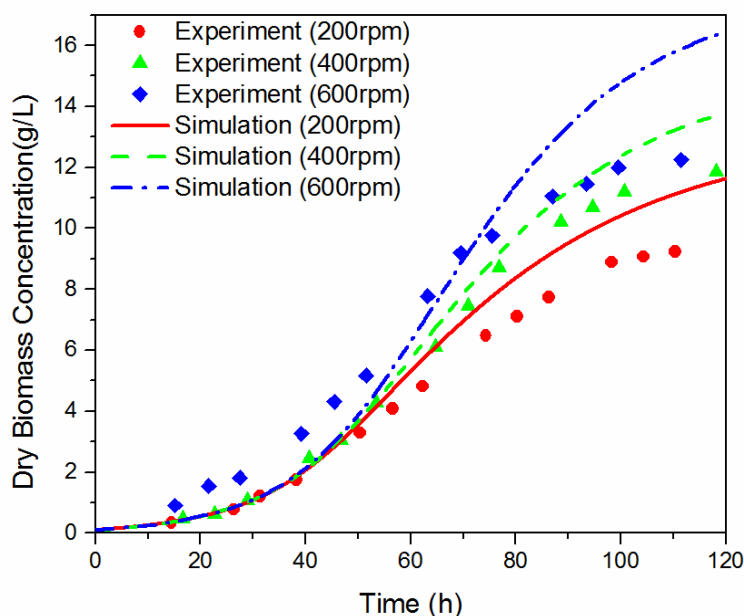


Figure 6.7. Comparison of simulated biomass growth curves (lines) with experimental data (symbols) for different reactor inner cylinder rotational speeds.

At least two causes can plausibly explain the discrepancy between experimental and simulated growth curves at long growth times. First, although biomass concentrations reach relatively high values (10-12g/L at higher rotational speeds) at long times and become light-limited, in the experiments it is possible that the batch system also becomes nutrient limited, especially in the late phase of growth when the biomass concentration is high, results in

unstable conditions in cells which influence the physiological status and photosynthetic efficiency. Strong evidence for this problem is provided by Kong *et al.* (2013), who found that after the biomass concentration approaches an asymptote at long times, the addition of urea spurs renewed growth. In contrast, no nutrient limitation is considered in the simulations as it is too complex and only happened when the biomass concentrations reach high values at long times.

The Lagrangian approach employed here suffers computational difficulties that may also contribute to discrepancies between simulation predictions and experimental measurements. Specifically, in the absence of the fluctuating eddy velocity given by Eq. (6.8), cell trajectories become highly periodic because they closely follow liquid streamlines. As a result, cells do not sample radial positions near the cylinder walls where the light intensity is very high (outer cylinder) or very low (inner cylinder). This problem becomes particularly acute at high biomass concentrations because light gradients become very steep near the outer cylinder wall, and if cells cannot closely approach the outer cylinder, then light exposure (as well as specific growth rate) will be under-predicted. Although the inclusion of eddy velocity fluctuations overcomes this problem, it leads to another difficulty. In particular, algal cells can become temporarily trapped at cylinder walls not due to any physical cause but because of the lack of submicron grid resolution required to properly model the motion of the microorganisms in the boundary layer near the wall. As a result, distortions in both the radial position-time and light history statistics are introduced. Specifically, unphysical trapping of cells on the outer cylinder wall leads to overestimation of the amount of light received by

those cells. Similarly, cells trapped on the inner cylinder wall receive less light than they would had they not become trapped.

The problem of cells lingering near reactor wall surfaces is evident in Figure 6.5 and can be quantified by computing the radial cell concentration distribution from an ensemble average of thousands of “snapshots” of radial particle positions. As can be seen in Figure 6.S2, cell concentration is uniformly distributed in the annular gap except near the cylinder walls, where there is significant enhancement of cell concentration. As a result, microorganisms spend too much time both in dark regions near the inner cylinder and bright regions near the outer cylinder. While these errors may be partially offsetting, it is clear from Figure S2 that cell concentration enhancement is greater near the outer cylinder, and as a result there may be net over-prediction of light delivery and algal growth rate.

Further insight into the reactor biomass growth curves can be gained by considering the temporal evolution of an ensemble average (1000 trajectories) for each of the three PSU states, as is shown in Figure 8. When the reactor is inoculated at the beginning of the experiment, the algae experience a sudden increase in light exposure and the fraction of PSUs in the active state increases rapidly, for example increasing from 0.59 to 0.95 in only a few seconds. The inhibited fraction of PSUs also increases, but this increase occurs over a much longer timescale reaching a maximum after approximately 20 hours at which time the biomass concentration is still much less than 1 g/L and no dark volume yet exists near the inner cylinder. The increase in the fraction of inhibited PSUs comes at the expense of active state PSUs and also leads to an increase in the resting state fraction as inhibited PSUs recover. As the biomass concentration increases with time, reactor volume near the inner

cylinder wall becomes dark (defined here as a photon flux of less than  $10 \mu\text{E}/\text{m}^2\cdot\text{s}$ , the approximate value of the photo compensation point), and consequently the fraction of PSUs in the resting state increases and the fractions of PSUs in the active and inhibited states declines as biomass growth becomes increasingly limited by light availability.

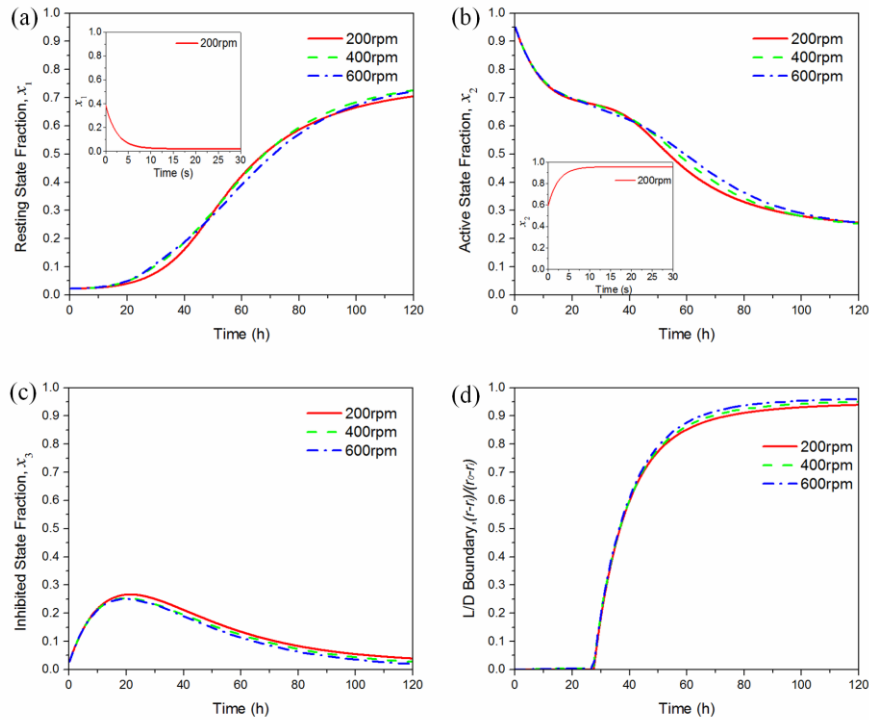


Figure 6.8. Fraction of photosynthetic units in the (a) resting, (b) active, and (c) inhibited states as a function of time. The radial position of the light/dark boundary, based upon the photocompensation point, is shown in (d) as a function of time.

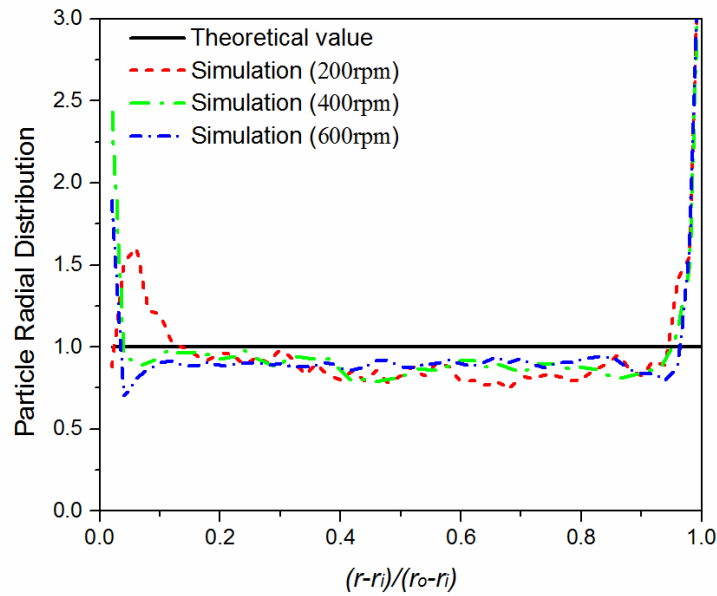


Figure 6.S2. Algal cell radial distribution function (based upon 1000 particle tracks) in the annular chamber at different inner cylinder rotation speeds.

### 6.5. Summary and Conclusions

A Lagrangian approach was used to simulate biomass growth curves in a Taylor vortex algal photobioreactor. In contrast to previous work, detailed and validated sub-models were employed to accurately predict fluid flow patterns and radiation transport in a non-trivial geometry. The resulting velocity and light distribution fields were used to generate thousands of cell light trajectories, which in turn were incorporated into a PSU model for algal growth kinetics. Direct comparison of simulation predictions with corresponding experimental data for biomass growth curves demonstrates that the computational model correctly predicts that biomass can be more rapidly produced by increasing the Taylor vortex reactor inner cylinder rotation speed. Although the simulated biomass growth curves produce reasonable

quantitative agreement with experimental data, at all cylinder rotation speeds considered the model over-predicts biomass concentration in later stages of the batch culture experiments.

Although these over-predictions may be partly explained by nutrient limitations present in the experiments but not considered in the simulations, computational limitations associated with the Lagrangian particle tracking approach also likely contributed to these discrepancies. Specifically, because microorganism cell sizes are on the order of microns, and because light gradients become very steep near the illuminated reactor surface as biomass concentration increases, accurate tracking of microorganism motion near reactor walls requires exceedingly fine spatial resolution. This is a crucial weakness of the Lagrangian particle tracking approach, and it motivates consideration of an alternative Eulerian approach wherein the algal growth model is directly coupled and integrated with the hydrodynamic model. A comparison of predictions of such an Eulerian model with both the Lagrangian model and experiments is considered in Gao et al. (2016b).

**CHAPTER 7. COMPREHENSIVE COMPUTATIONAL MODEL FOR COMBINING  
FLUID HYDRODYNAMICS, LIGHT TRANSPORT AND BIOMASS GROWTH IN A  
TAYLOR VORTEX ALGAL PHOTOBIOREACTOR: EULERIAN APPROACH**

Modified from the paper “Gao X, Kong B, Vigil RD. 2016. Comprehensive computational model for combining fluid hydrodynamics, light transport and biomass growth in a Taylor vortex algal photobioreactor: Eulerian approach. Submitted to Algal Research.”

A comprehensive Eulerian approach for integrating a three-phase CFD model, a sophisticated detailed model for radiation transport, and a transport equation for algal growth kinetics is developed and utilized to predict the performance of a Taylor vortex algal photobioreactor. Simulation predictions are compared with corresponding experimental data and with simulation predictions obtained using the more commonly employed Lagrangian particle tracking method. The simulation predictions correctly predict the experimental trend that biomass productivity increases with increased rates of mixing. However, at the high biomass loadings achievable in photobioreactors, most radiation is absorbed near illuminated reactor surfaces and it becomes increasingly important, but also more difficult, to properly resolve the thinning hydrodynamic and radiative boundary layers.

## 7.1. Introduction

Recently, computational fluid dynamics (CFD) has been used to simulate the performance of algal photobioreactors as a means of reducing design costs and improving reactor efficiency (Bitog *et al.*, 2011). Such simulations present many challenges such as formulating and solving accurate, quantitative models for the physical and biological processes that determine reactor performance, including multiphase hydrodynamics and mass transport (gas-liquid-solid flow), radiation transport, and microorganism biological function. At present, computational simulations of algal growth in photobioreactors incorporating all these factors have been limited (Luo and Al-Dahhan, 2012), in part due to the fact that the relevant phenomena are highly coupled and interact across widely separated timescales (Merchuk *et al.*, 2007).

At high biomass concentrations, light availability decays sharply with distance from irradiated surfaces in photobioreactors due to microorganism self-shading. As a result, cells may receive sufficient or even excess radiation near irradiated surfaces and insufficient or no radiation in other regions of the reactor. Hence, light delivery is usually the most important and limiting factor controlling performance of photobioreactors (Richmond, 2004). However, since fluid mixing governs the movement of cells in the reactor and thereby determines the light exposure that they experience, accurate simulation of hydrodynamics is a crucial component of any model predicting photobioreactor performance. Indeed, reactors that provide flow structures that induce coherent light-dark cycles significantly improve microalgal growth rate (Hu and Richmond, 1996; Jansen *et al.*, 2000; Kong *et al.*, 2013; Nauha and Alopaeus, 2013; Olivieri *et al.*, 2015; Huang *et al.*, 2015).

In view of the above discussion, it is evident that in addition to accurate models for fluid flow, radiation transport, and biomass growth kinetics, a computational framework for coupling models for the governing phenomena is required in order to predict photobioreactor performance (Pruvost *et al.*, 2002). The most common approach for coupling fluid mixing, radiation transport, and algal growth kinetics employs the following general algorithm: (1) independently solve the equations of motion for fluid flow and radiative transport, (2) use computed fluid flow velocity field predictions to perform Lagrangian particle tracking simulations for numerous algal cell trajectories with random starting positions, (3) use the resulting cell spatial trajectories and results from light distribution simulations to compute temporal cell light exposure histories, and (4) use the cell light exposure trajectories to compute biomass growth rate.

In our previous paper (Gao *et al.*, 2016b), we employed detailed CFD, radiation, and a photosynthetic unit (PSU) model of algal growth to carry out Lagrangian simulations for biomass accumulation in a Taylor vortex photobioreactor. A comparison of simulation predictions with experiments demonstrated reasonably good quantitative agreement for several reactor operating conditions, but biomass yield was consistently over-predicted. These errors can be attributed in part to an inherent weakness of Lagrangian particle tracking, namely the difficulty in accurately computing cell trajectories near reactor surfaces (Pruvost *et al.*, 2008; Gao *et al.*, 2016b).

Here we describe an alternative approach for coupling models for hydrodynamics, radiation transport, and algal growth kinetics that does not require Lagrangian particle tracking. Specifically, we make use of the same models for radiation transport and algal growth kinetics employed in the Lagrangian simulations. However, particle tracking is

avoided by solving a transport equation for the algal growth model within a three-phase (liquid-gas-solid) computational fluid dynamics (CFD) simulation in order to produce local predictions for algal growth rate, which in turn can be used to compute the global reactor performance. This Eulerian framework for incorporating hydrodynamics, radiation transport, and algal growth kinetics is then used to generate predictions for the performance of a Taylor vortex photobioreactor and these predictions are compared with those obtained using the Lagrangian approach and with corresponding experiments. Although the proposed Eulerian simulation method has significant advantages compared to the Lagrangian approach, it also suffers some drawbacks at high biomass loadings due to difficulties in resolving steep gradients near the reactor illuminated surface.

The remainder of the paper is organized as follows. In Section 7.2 model equations and computational methods are discussed. In Section 7.3, Eulerian simulation predictions for algal growth curves (*Chlorella vulgaris*) in a Taylor vortex photobioreactor are compared with those obtained from a Lagrangian simulation as well as with experimental data. Discussion of weaknesses of the two methods, as well as challenges associated with simulation of algal photobioreactors more generally, are presented in Sections 7.3 and 7.4.

## **7.2. Model Equations and Methods**

### **7.2.1. Three-phase Fluid Flow Model**

The multiphase flow dynamics in a Taylor-Couette bioreactor are governed by interactions among three phases including gas bubbles, liquid culture media, and microalgal cells (solid). Here, the three-phase Eulerian approach was used, which was based on a validated two-fluid Eulerian-Eulerian model for bubbly Taylor-Couette flow (Gao *et al.*,

2015b). In our previous work, the two-fluid model was validated by direct comparison of simulation predictions with velocity and phase distribution data from experiments performed by Murai *et al.* (2005), who carried out studies of a vertical semi-batch gas-liquid Taylor-Couette reactor. The multiphase flow between two vertically oriented concentric cylinders was assumed to be axisymmetric, so that the quasi-two-dimensional mass and momentum equations include an axisymmetric azimuthal velocity component:

$$\frac{\partial}{\partial t}(\alpha_k \rho_k) + \nabla \cdot (\alpha_k \rho_k \vec{u}_k) = 0 \quad (7.1)$$

$$\frac{\partial}{\partial t}(\alpha_k \rho_k \vec{u}_k) + \nabla \cdot (\alpha_k \rho_k \vec{u}_k \vec{u}_k) = -\alpha_k \nabla p + \nabla \cdot (\overline{\overline{\tau}}_k + \overline{\overline{\tau}}_k^{Re}) + \alpha_k \rho_k \vec{g} + \vec{F}_{Ik} \quad (7.2)$$

Here,  $\alpha_k$  and  $\vec{u}_k$  are the phase volume fractions and velocities for liquid ( $k = l$ ), gas ( $k = g$ ), and solid ( $k = s$ ). The phase stress and Reynolds stress tensors are represented by  $\overline{\overline{\tau}}_k$  and  $\overline{\overline{\tau}}_k^{Re}$ , respectively. Turbulence was simulated using the standard  $\mathbf{k} - \omega$  model (Wilcox, 1998), as this method has been shown to accurately predict fluid dynamics in turbulent Taylor-Couette flow (Gao *et al.*, 2015a; 2015b; 2016a).

In Taylor vortex algal photobioreactors the primary liquid growth medium is continuous whereas the low volume fraction secondary gas (< 2%) and solid phases (< 1%) are dispersed. Momentum exchange between the liquid and each dispersed phase is considered, whereas momentum exchange between the gas and solid dispersed phases is neglected. Based upon our previous work, the liquid-gas momentum exchange term,  $\vec{F}_{lg}$ , can be decomposed into five independent interphase forces including drag, lift, virtual mass, wall lubrication, and turbulent dispersion forces. The constitutive relations, model parameters, and thermal properties for the gas-liquid interactions can be found in Gao *et al.* (2015a). In view of the small size of the algal microorganism considered (~5 microns), drag is the only

non-negligible liquid-solid interfacial force, and the Schiller-Naumann (1935) drag model was used to model this interaction:

$$\vec{F}_{Ds} = -\vec{F}_{Dl} = \frac{3\rho_l}{4d_s} \alpha_s \alpha_l C_D |\vec{u}_s - \vec{u}_l| (\vec{u}_l - \vec{u}_s) \quad (7.3)$$

$$C_D = \frac{24}{\text{Re}_s} \left( 1 + 0.15 \text{Re}_s^{0.687} \right) \quad (7.4)$$

Other model parameters relevant to liquid-solid interactions are listed in Table 7.1.

Table 7.1. Liquid and solid model parameters and constants (Gao *et al.*, 2015a; 2015c)

$\rho_l$	1036 kg m <sup>-3</sup>	$\mu_l$	7.22×10 <sup>-4</sup> kg m <sup>-1</sup> s <sup>-1</sup>
$\rho_s$	1036 kg m <sup>-3</sup>	$\mu_s$	7.22×10 <sup>-4</sup> kg m <sup>-1</sup> s <sup>-1</sup>
$d_s$	5×10 <sup>-6</sup> m	$D_{s,L}$	5.5×10 <sup>-10</sup> m <sup>2</sup> s <sup>-1</sup>
$Sc_t$	0.7		

### 7.2.2. Algal Biomass Growth Model

Algal growth kinetics were simulated using the revised photosynthetic unit (PSU) growth model of Wu and Merchuk (2001) that is based upon the model first introduced by Eilers and Peeters (1993). The PSU model envisions light absorbing reaction centers in microorganisms residing in one of three states including a resting state (fraction  $x_1$ ), an active state ( $x_2$ ), and an inhibited state ( $x_3$ ). By considering possible transitions between the three states, the following equations are obtained:

$$\frac{dx_1}{dt} = -\alpha I x_1 + \gamma x_2 + \delta x_3 \quad (7.5a)$$

$$\frac{dx_2}{dt} = \alpha I x_1 - \gamma x_2 - \beta I x_2 \quad (7.5b)$$

$$x_1 + x_2 + x_3 = 1 \quad (7.5c)$$

$$\mu = k\gamma x_2 - M \quad (7.6)$$

Here  $I$  is the radiative flux,  $\mu$  is the specific growth rate, and  $M$  is a maintenance coefficient representing requirements for internal metabolism. The presence of the latter term in Eq. (7.6) provides the possibility of negative growth for situations in which the radiative flux falls below the compensation point. As reported previously, the above PSU model can be fitted to experimental data (Dauta *et al.*, 1990) for *Chlorella vulgaris*, yielding the following parameter values:  $\alpha = 7.253 \times 10^{-4} \text{ m}^2/(\mu\text{E})$ ,  $\beta = 1.703 \times 10^{-8} \text{ m}^2/(\mu\text{E})$ ,  $\delta = 9.968 \times 10^{-6} \text{ s}^{-1}$ ,  $\gamma = 0.009485 \text{ s}^{-1}$ ,  $k = 0.004511$ ,  $M = 9.913 \times 10^{-6} \text{ s}^{-1}$ .

In contrast to the Lagrangian particle tracking approach, which requires knowledge of the temporal light exposure experienced by microorganisms in order to solve Eqs. (7.5) and (7.6), in the Eulerian method the fraction of reaction centers occupying each possible state (resting, active, or inhibited) at each position in the reactor is computed. This can be achieved by including convective and diffusive transport terms in the conservation equations for  $x_1$  and  $x_2$  so that Eqs. (5a) and (5b) are replaced by the following reaction-transport equations:

$$\begin{aligned} \frac{\partial}{\partial t}(\alpha_s \rho_s x_1) + \nabla \cdot (\alpha_s \rho_s \vec{u}_s x_1) &= -\nabla \cdot (\alpha_s \rho_s D_e \nabla x_1) \\ &+ \alpha_s \rho_s (-\alpha I x_1 + \gamma x_2 + \delta x_3) \end{aligned} \quad (7.7a)$$

$$\begin{aligned} \frac{\partial}{\partial t}(\alpha_s \rho_s x_2) + \nabla \cdot (\alpha_s \rho_s \vec{u}_s x_2) &= -\nabla \cdot (\alpha_s \rho_s D_e \nabla x_2) \\ &+ \alpha_s \rho_s (\alpha I x_1 - \gamma x_2 - \beta I x_2) \end{aligned} \quad (7.7b)$$

The above expressions couple not only to the local radiative flux, but also to the solid phase velocity. Here  $D_e$  is the effective turbulent diffusivity of the solid phase (microorganisms),

and it can be expressed as

$$D_e = D_{s,L} + \frac{\mu_t}{\rho_s Sc_t} \quad (7.8)$$

where  $D_{s,L}$  is the laminar diffusivity of the solid and  $Sc_t$  is the turbulent Schmidt number. The turbulent Schmidt number is the only additional adjustable parameter introduced in the Eulerian approach, but for the reactor operating conditions considered here, predictions for biomass concentration are insensitive to the value chosen for  $Sc_t$  in the range of 0.1-1.3 (Lilly, 1973).

By solving Eqs. (5c)-(8) within a CFD code, the reactor volume averaged specific growth rate  $\bar{\mu}$  can be computed and therefore the global biomass concentration  $C_b$  can be obtained by integrating the following expression:

$$\frac{dC_b}{dt} = \bar{\mu} C_b \quad (7.9)$$

### 7.2.3. Radiation Transport Model

The distribution of light as a function of biomass loading and position in the Taylor vortex reactor was obtained by solving the general radiative transport equation using the method described by Kong and Vigil (2014) as applied to a culture of *Chlorella vulgaris*. As has been described elsewhere (Gao *et al.*, 2016b), an algebraic expression was fitted to these results, giving the following dimensional equation that can be used to interpolate the photon flux for any radial position  $r$  and biomass concentration  $C_b$ :

$$I = I_o \exp \left[ (aC_b + b) \frac{r}{r_o} + c \right] \left( \frac{r}{r_o} \right)^{dC_b + e} \quad (7.10)$$

Here,  $I_o = 592.7 \mu\text{E}/\text{m}^2 \cdot \text{s}$ ,  $r_o$  is the outer cylinder radius,  $C_b$  is the dry biomass concentration (g/L), and  $r$  is radial position (m). The fitted constants ( $R = 0.9981$ ) are  $a = -0.02431 \text{ L/g}$ ,  $b =$

8.234,  $c = -8.351$ ,  $d = 19.22$  L/g,  $e = -9.567$ . Hence, Eq. (7.10) eliminates the need to perform radiation transport simulations in parallel with CFD simulations. It should be noted that the radiation model neglects bubble light scattering, and the justification of this assumption is discussed in Section 7.3.

#### **7.2.4. Coupling of Model Components**

A schematic diagram illustrating the approach for coupling the hydrodynamic, algal growth, and radiation models is depicted in Figure 7.1. The method assumes that microalgae are uniformly distributed in the reactor (confirmed from CFD simulation results discussed later). Since even for very high biomass concentrations the volume fraction of algae in the reactor is very low (<1%), the effect of biomass concentration on hydrodynamics was neglected. As a consequence of these assumptions, only one-way coupling exists between the hydrodynamic and algal growth rate models (algal growth model depends upon the hydrodynamics). As was discussed previously, the photon flux can be accurately computed for arbitrary biomass concentration and annular radial position using Eq. (7.10). Since the algal growth model depends upon the light distribution and the light distribution in turn depends upon the biomass concentration, two-way coupling exists between radiation transport and algal growth models.

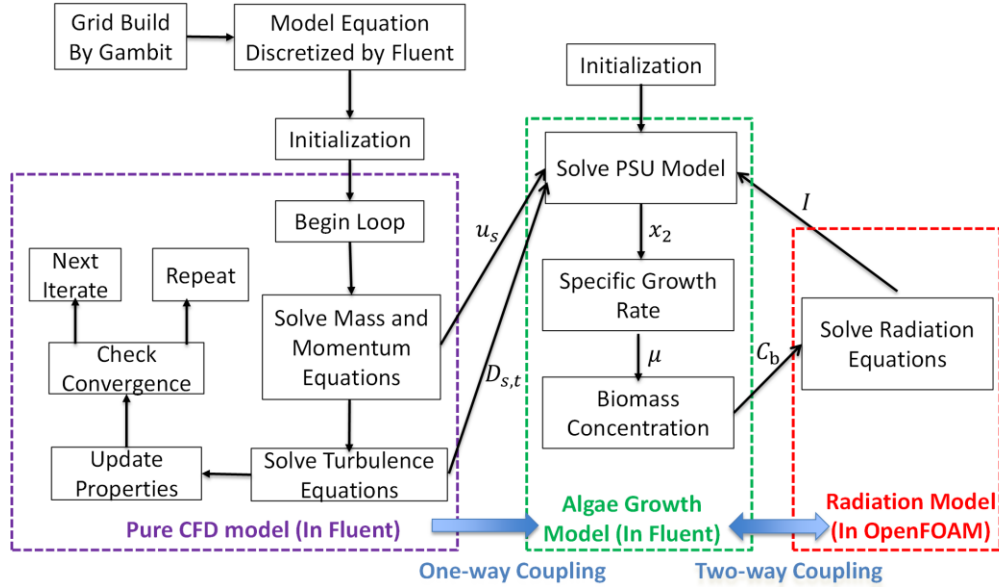


Figure 7.1. Eulerian approach for coupling hydrodynamics, radiation transport, and algal growth kinetics.

In summary, the overall approach for computing biomass accumulation in the Taylor vortex reactor includes (a) computing velocity fields and turbulent diffusion coefficient distributions for the gas-liquid-solid system, (b) using this hydrodynamic information as well as the photon flux distribution obtained from Eq. (7.10) to compute the volume averaged algal specific growth rate  $\bar{\mu}$  using Eqs. (7.5c)-(7.8), and (c) updating the reactor biomass using Eq. (7.9).

### 7.2.5. Computational Details

A schematic of the Taylor-Couette apparatus and other details relevant to *Chlorella vulgaris* growth experiments can be found in Gao *et al.* (2015b). The rotating inner cylinder has a radius of 3.81 cm and the fixed transparent outer cylinder has an inner radius of 5.08 cm, resulting in an annular gap width of 1.27 cm. The length of the reactor is 50.8 cm and the

reactor is filled to a height of  $h = 48$  cm, producing a total liquid working volume of 1.70 L.

The hydrodynamic and algal growth models were integrated using the commercial finite volume CFD software ANSYS FLUENT 14.5 (Ansys Inc., US). A non-uniform rectangular computational mesh consisting of  $64 \times 960$  (radial  $\times$  axial) nodes was employed to represent the annular chamber after carrying out a grid-independence study. No-slip boundary conditions were used for all three phases at wall boundaries. The gas velocity prescribed at the gas inlet at the bottom of the reactor was chosen to match experimental conditions (85 mL/min) and by specifying an inlet bubble volume fraction of 0.05. Pressure outlet boundary conditions were used for all fluid phases at the free surface at the top of the reactor. The azimuthal velocity of the inner cylinder was chosen to match those used in corresponding experiments, ranging from 200 to 600 RPM.

The transient CFD simulations were carried out using a time step of  $5 \times 10^{-4}$  s. The global reactor biomass was evolved using Eq. (7.9) with an initial condition of 0.1 g/L (corresponding to experiments) and an integration time step of 10 seconds, since the characteristic algal growth time scale is many orders of magnitude larger (hours or days) than the light/dark time scale (less than a second). The effect of changing the integration step size for Eq. (7.9) was explored and it was found that time steps smaller than 10 seconds result in very little change in predictions for the global biomass concentration.

## **7.3. Results and Discussion**

### **7.3.1 Flow Hydrodynamics**

Figure 7.2a shows a contour plot of the gas bubble distribution inside the annular gap. Bubbles strongly concentrate near the inner wall, consistent with our previous findings for

two-phase gas-liquid flow (Gao *et al.*, 2015b, Ramezani *et al.*, 2015). The volume-averaged global gas volume fraction for the flow conditions studied is very low ( $< 2\%$ ), and the local gas volume fraction in most parts of the reactor is less than 0.1% except at the maxima along the inner cylinder wall where values can reach 10%. However, even for relatively modest biomass loadings (e.g. 0.5 g/L), very little photosynthetic radiation is able to penetrate as far as the inner cylinder wall, and therefore the assumption that the presence of this small volume of gas bubbles can be neglected in the radiation transport model is justified. It should be noted that such a simplification is likely not applicable to other photobioreactors including bubble columns, airlift, and stirred tank reactors since gas bubbles in these systems are more uniformly distributed.

In contrast to gas bubbles, the contour plot shown in Figure 7.2b demonstrates that the simulated solid phase (algal cells) is distributed uniformly in the reactor except at locations near the inner cylinder where gas bubbles are present in relatively high concentration. Even this local depletion of algal cells is modest and can be observed only by exaggerating the color scale on the contour plot. This finding is unsurprising since algal cells have small Stokes number due to their small size ( $\sim 5 \mu\text{m}$  for *Chlorella vulgaris*) and density close to the liquid culture medium. Figure 7.2c depicts a vector plot of the solid phase (algae) velocity. It is evident that microorganisms follow Taylor vortex streamlines and are rapidly and periodically shuttled between the illuminated outer cylinder and darker regions near the inner cylinder. In view of the results discussed above, the assumption that microalgae are uniformly distributed in the reactor is justified.

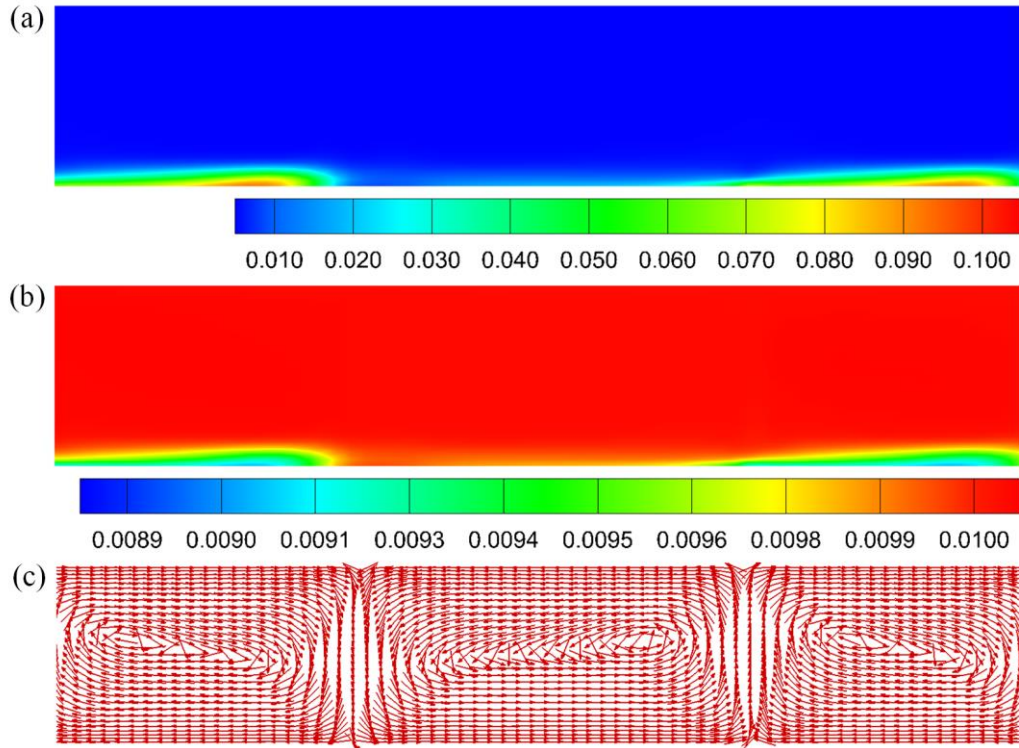


Figure 7.2. Contour plots of (a) bubble volume fraction and (b) solid volume fraction. Panel (c) depicts a solid phase (algal cells) velocity vector plot for an inner cylinder rotation speed of 400 rpm. The inner and outer cylinder walls are represented by the bottom and top boundaries, respectively.

### 7.3.2. Light Distribution

The photon flux in the annular reaction zone computed from the radiation transport model is plotted in Figure 7.3 for several biomass concentrations. It is evident that the radiation distribution is quite sensitive to biomass concentration, and it has been shown previously that light distribution in this annular geometry cannot be accurately described by the Beer-Lambert approximation for solution of the radiative transport equation (Kong and Vigil, 2014). Figure 7.3 also demonstrates that at high biomass concentrations typical of photobioreactors, the gradient in photon flux is steep near the illuminated reactor wall and

most of the reactor is comprised of “dark volume” with little radiative flux. Indeed, for biomass concentration greater than 4 g/L, more than 70% of the photobioreactor volume could be considered to exist under dark conditions.

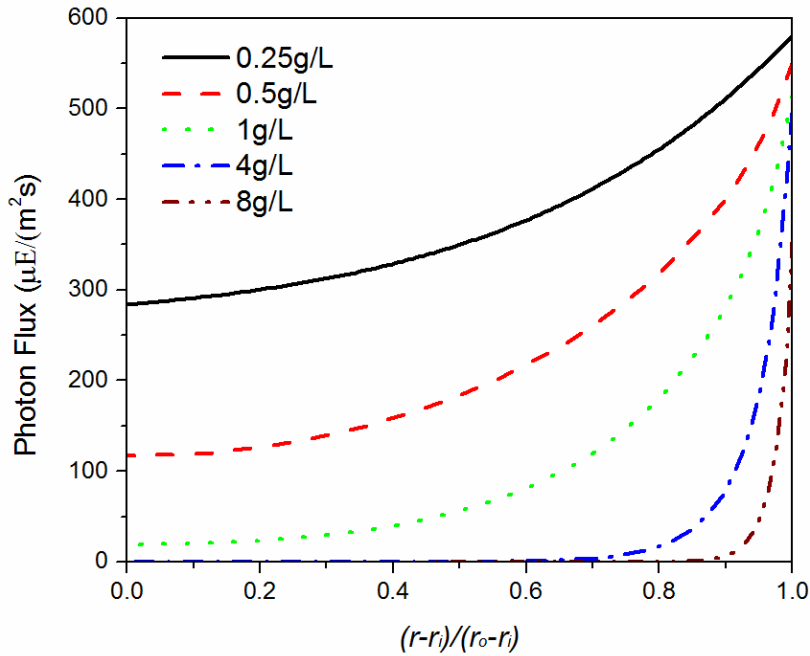


Figure 7.3. Photon flux as a function of normalized radial position and for various biomass loadings, as obtained using the method of Kong and Vigil (2014) for solving the general radiative transport equation for *C. vulgaris* in a Taylor vortex reactor.

### 7.3.3 Biomass Growth Curves

Simulation predictions and corresponding experimental data for the evolution of biomass concentration in the Taylor vortex reactor are shown in Figure 7.4a for various inner cylinder rotation speeds and mixing conditions. In all cases the biomass growth curve exhibits the well known sigmoidal shape characteristic of batch cultures. Two limiting cases are also shown, namely complete mixing and no mixing. These can be easily computed using

Eq. (7.10) and by either assuming that the PSU fractions that appear in Eq. (7.7) are independent of position (complete mixing) or that the PSU fractions are spatially dependent and no transport mechanism is operative. As expected these limiting cases bracket a wide range of possible outcomes at long culture times. At low biomass concentrations, such as those that exist immediately after inoculation, no dark volume exists, as is illustrated by Figure 7.5 (d), which shows the radial position of the compensation point ( $10 \mu\text{E}/\text{m}^2\text{-s}$  for *Chlorella vulgaris*) as a function of culture time. As a result of the lack of dark volume, the movement of cells between the outer and inner cylinders has negligible effect on biomass growth rate (i.e. for cultivation times  $< 20$  h). Indeed, simulation predictions for all mixing conditions and cylinder rotation speeds are nearly identical at low biomass concentrations. In contrast, for biomass concentrations greater than approximately 1 g/L, significant light depletion exists in the reactor and fluid mixing plays a stronger role in determining biomass growth rate, and it can be observed that higher cylinder rotation speeds lead to increased algal growth rates. Further insight into the predictions for evolution of biomass in the reactor can be obtained from temporal plots of PSU state, as shown in Figures 7.5 (a)-(c). As expected, before the reactor becomes light limited, fluid mixing has no effect on the fractions of PSUs in the three states (resting, active, or inhibited). Even for high biomass loadings when dark volume is present in the reactor, fluid mixing has only a small effect on the fraction of PSUs residing in the inhibited state. However, mixing does cause a shift in the balance between PSUs in the resting and active states at higher biomass concentrations, with the active fraction increasing as cylinder rotation speed increases. It is evident from Figs. 7.4(a), 7.5(a), and 7.5(b) that even small changes in this balance lead to significant differences in total biomass accumulation.

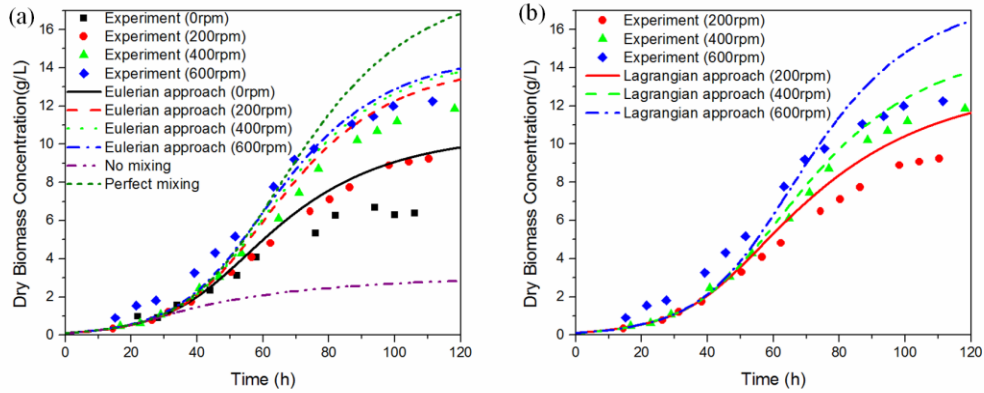


Figure 7.4. (a) Comparison of algal growth curve predictions with experiments in a Taylor vortex reactor for various mixing conditions and using the Eulerian modeling approach. (b) Comparison of algal growth curve predictions with experiments in a Taylor vortex reactor for various mixing conditions using the Lagrangian modeling approach.

### 7.3.4 Comparison of Eulerian and Lagrangian Simulations

As was mentioned in Section 7.1, two distinct approaches have been used to simulate the interplay between hydrodynamics, radiation transport, and algal growth kinetics in order to predict the performance of algal photobioreactors. The essential difference between these approaches is in the method used to compute microorganism radiation exposure. In the Lagrangian approach, trajectories of individual cells are computed in order to determine light exposure history, and an ensemble average of simulated cell trajectories is used to estimate overall reactor performance. In the Eulerian approach, transport equations for the algal concentration and PSU state are solved within the same computational grid as is used for the fluid dynamics simulation.

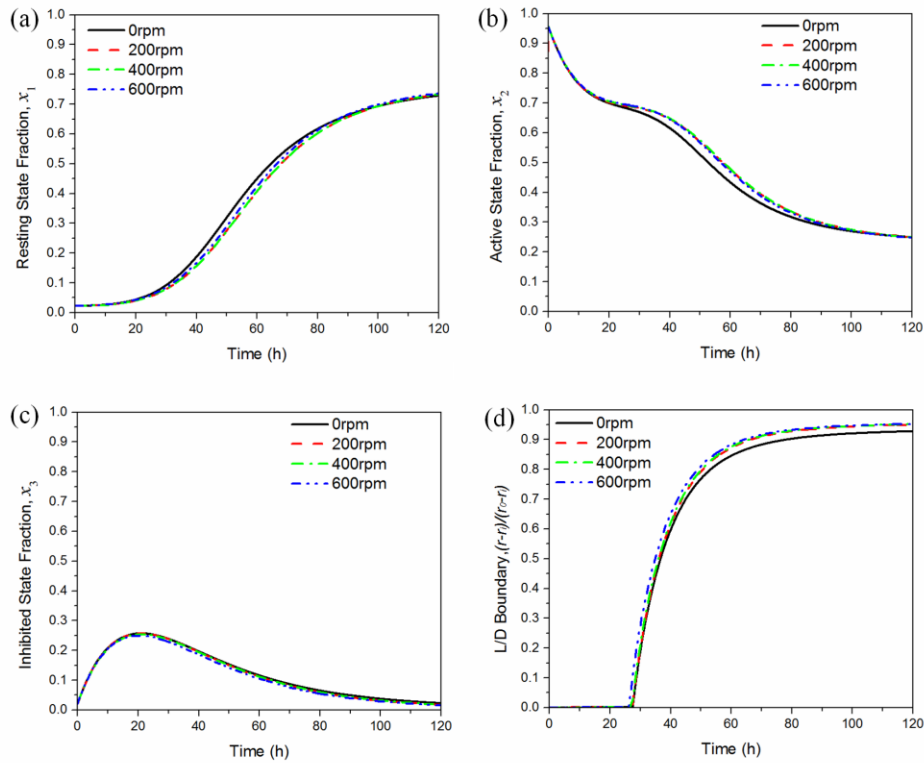


Figure 7.5. Fraction of photosynthetic units in the (a) resting, (b) active, and (c) inhibited states as a function of time. The radial position of the light/dark boundary, based upon the photocompensation point, is shown in (d).

Comparison of Figures 7.4a (Eulerian) and 7.4b (Lagrangian – results from Gao *et al.*, 2016b) demonstrates that the two approaches lead to different predictions despite the fact that they make use of the same basic assumptions and employ the same light exposure model and kinetic expressions for algal growth. The primary difference in the simulations is that the Eulerian model predicts practically uniform distribution of algal cells in the annular reaction zone, in contrast to the Lagrangian approach which suffers from trapping of cells near cylinder walls, thereby leading to overexposure of cells to radiation near the illuminated outer cylinder and under exposure near the inner cylinder (Gao *et al.*, 2016b).

Both models predict increasing biomass growth rate with increasing rotation speed, and

both models also over-predict biomass concentration at late stages of the culture experiments. These over-predictions are likely due at least in part to the fact that the kinetic growth models do not account for depletion of nutrients such as nitrogen, which is known to occur in the batch culture experiments (Kong *et al.*, 2013). A comparison of Figs. 7.4a and 7.4b also show that the Eulerian model predicts relatively little sensitivity of the biomass growth curves to cylinder rotation speeds between 200-600 RPM, in contrast to experimental measurements and predictions of the Lagrangian model. Nevertheless, the Eulerian model predictions for biomass accumulation are substantially lower than those obtained by assuming complete mixing (i.e. uniform spatial distribution of PSU fractions).

In view of the above discussion, it is apparent that mixing becomes important only for relatively high biomass concentrations such that dark volume is present. However, as biomass concentration increases, light gradients become steep near the illuminated outer cylinder wall. It is not difficult to anticipate that with continued increases in biomass concentration, the gradients in radiative flux become so steep that the thickness of the illuminated reactor volume (radiative boundary layer) can become smaller than the hydrodynamic boundary layer. Since biomass productivity depends upon microorganism light exposure, and because this exposure occurs primarily near the illuminated wall at high biomass loadings, it is essential that the velocity field be resolved in the radiative boundary layer. Resolving the hydrodynamic boundary layer at the high azimuthal Reynolds numbers considered here could in principle be achieved by employing direct numerical simulation (DNS) methods, but are impractical within a reactor-scale model. In the Eulerian simulations presented here, insufficient spatial resolution is present to account for the effects of changes in inner cylinder rotation speed (azimuthal Reynolds number) on the velocity field in the

hydrodynamic boundary layer, and therefore biomass accumulation does not exhibit strong dependence on rotation speed. In contrast, in the Lagrangian particle trapping approach microorganisms can become trapped near both the inner and outer cylinder wall leading to greater possibility for PSUs to transition to the inhibited state, thereby reducing biomass productivity. As the inner cylinder rotation speed increases, fewer Lagrangian particles become trapped and the inhibited fraction of PSU's decrease (see figure 8(c) in Gao *et al.* (2016b)).

#### 7.4. Conclusion

Batch culture of *C. vulgaris* in a Taylor vortex photobioreactor was simulated using an Eulerian method for coupling hydrodynamics, radiation transport, and biomass growth kinetics. The simulations suggest that two key approximations – namely that microalgae are uniformly distributed in the reaction volume and gas bubble congregate near the dark rotating cylinder are justified. However, at high biomass loadings most radiation is absorbed in a small volume near the illuminated outer cylinder, and as a consequence accurate prediction of reactor performance demands ever increasing resolution of the hydrodynamic boundary layer as the “radiative boundary layer” continues to shrink. This problem is not limited to the Eulerian approach – indeed the alternative Lagrangian particle tracking method must also properly account for microorganism light exposure time as cells pass through the thinning radiative boundary layer. As has been shown previously, particle tracking near solid boundaries is difficult due to trapping associated with lack of resolution of the hydrodynamic boundary layer. In summary, accurate simulation of photobioreactors remains a difficult challenge, especially for high biomass loadings that are desirable and achievable in such devices. In order to further advance the accuracy of such simulations, it appears that an

adaptive approach that incorporates progressive grid refinement for hydrodynamic and radiative transport near the illuminated reactor surface may be required.

## CHAPTER 8. SUMMARY AND FUTURE WORK

In this chapter, sub-projects done in previous chapters are summarized, and works can be performed are proposed in future work.

### 8.1. Summary

The objective of the project is to develop a comprehensive model coupling fluid hydrodynamics, radiation transport, and algae growth rate model to model the biomass growth in a Taylor vortex reactor. All involved sub-models were developed and validated first, then two different coupling methods were proposed and compared.

In chapter 1, the motivation of this work was introduced. Then the challenges in photobioreactors simulation were briefly discussed and plan of work was made.

In chapter 2, review studies for mathematical models of hydrodynamics, mass transfer, radiation transport, microalgae growth model and their coupling within the photobioreactors were summarized. It is found that there is still a need for significant contributions in developing and validation reliable sub-models and coupling method for photobioreactor performance simulation to reduce cost and increase efficiency in large-scale biomass production.

In chapter 3, in order to quantitatively describe the hydrodynamics of two-phase Taylor-Couette flow, a rigorous two-fluid computational fluid dynamics (CFD) model was developed and validated. Bubble effects on Taylor-Couette flow patterns and structures in the weakly Taylor vortex flow regime were numerically investigated by quasi-2D and 3D

simulation and compared with experimental data available in the literature. We found that the radial non-uniformity in the gas phase volume fraction is mainly determined by the balance between the pressure gradient force, the wall lubrication force, and the turbulent dispersion force, whereas the virtual mass and lift forces have negligible effect on the spatial distribution of bubbles. We also found that gas velocity strongly influences the wavelength of Taylor vortices, in contrast to the azimuthal Reynolds number, which has little effect in the range  $Re = 600-3900$ .

In chapter 4, an adaptive oxygen mass transfer model was developed and validated in Taylor-Couette bioreactor. The mass transfer model is based on the Higbie theory but automatically adapts to the local hydrodynamic environment by computing exposure time using either the penetration theory or eddy cell model based upon the turbulence dissipation rate. This adaptive approach was shown to provide much more accurate predictions for the volumetric mass transfer coefficient than does either model used alone.

In chapter 5, in order to answer the question that promoted biomass growth is due to enhanced mass transfer or light/dark cycles, an algae culture experiment was conducted in Taylor-Couette photobioreactor. By comparing the characteristic time scale for mixing, mass transfer and biomass growth, it is found that fluid flow patterns in these systems accelerate growth through improved light delivery to microorganisms rather than by improved delivery of carbon dioxide. The analysis presented here provides a guide for deconvoluting the effects of mixing, mass transfer, and light delivery for other PBR designs as well, and such information could be useful for optimizing PBR design and operation.

In chapter 6, a Lagrangian approach was used to simulate biomass growth curves in a Taylor vortex algal photobioreactor. Direct comparison of simulation predictions with

corresponding experimental data for biomass growth curves demonstrates that the computational model correctly predicts that biomass can be more rapidly produced by increasing the Taylor vortex reactor inner cylinder rotation speed. Although the over-predictions of biomass concentration in the later stages may be partly explained by nutrient limitations present in the experiments but not considered in the simulations, computational limitations associated with the Lagrangian particle tracking approach also likely contributed to these discrepancies.

In chapter 7, a comprehensive Eulerian approach for integrating a three-phase fluid flow model, a detailed model for radiation transport, and a transport equation for algal growth kinetics were developed and integrated in order to predict the performance of a Taylor vortex algal photobioreactor. Simulation predictions were compared with corresponding experimental data and with simulation predictions obtained using the more commonly used Lagrangian particle tracking method. The simulation predictions correctly predict the experimental trend that biomass productivity increases with increased rates of mixing. The chief advantage of the Eulerian approach is that it eliminates the need to perform thousands of particle tracking simulations required by the Lagrangian approach. Such findings may be of immediate interest to process engineers seeking to simulate, optimize, or scale up PBRs.

In chapter 8, important results and opportunities in comprehensive photobioreactors simulations were summarized.

## **8.2. Opportunities**

Designing and optimizing photobioreactors still remain big challenges and a successfully scaled up PBRs for large-scale microalgae production are still very limited. Comprehensive mathematical modeling has proved to be an effective technique for solving

these limitations and challenges, while only a few factors can be considered as they are highly coupled. Thus, a more comprehensive PBRs model for algal biomass is needed that can incorporate information from hydrodynamics, cell light history, CO<sub>2</sub> and O<sub>2</sub> mass transfer, nutrient concentration, etc. The challenges and opportunities are summarized as follows.

First, in the multiphase CFD simulation, the bubble is always assumed to be spherical. While in the real PBRs, the bubbles have a variety of shapes and diameters, and even aggregate to form irregularly shaped bubble swarms. This largely increases the complexity to model the hydrodynamics accurately. Developing and validating reliable interphase force models is needed. In terms of the turbulence model, the general  $k-\varepsilon$  or  $k-\omega$  models are widely used, while it should be noted that bubbles can affect the characteristic of turbulent liquid flow and produce extra turbulence, which is called bubble-induced turbulence (BIT). The BIT theory remains developed and should be considered in future simulation.

Second, for the mass transfer simulation, the penetration theory model is known to underpredict mass transfer for highly turbulent flows, while the eddy cell model is known to underpredict mass transfer for weakly turbulent flows. The adaptive mass transfer model proposed by Gao et al. (2015a) combines the strength of the existing penetration and eddy cell models, but it also inherits weaknesses of the two models. It is found that the adaptive model performs very well in the weakly and highly turbulent flow regimes, but not in moderately turbulent flow conditions when compared with our experimental data. At present, there is not any mass transfer model that provides accurate predictions across the whole range of flow regimes. Hence, a more accurate and more general gas-liquid mass transfer

model should be developed. This can be achieved by bubble-resolved DNS simulation to understand the underlying mechanics.

Third, radiation transport models mainly consider the effect of cells on light attenuation, while the presence of bubbles is usually not considered. A new radiation transport model that can account for the scattering of light by bubbles, and how this effect depends upon bubble volume fraction, size and shape should be developed and validated by carrying out light measurement experiments.

Fourth, a more advanced microalgae growth rate model should be developed. The photoacclimation should be considered in the growth rate model. Photoacclimation is a process whereby microalgae adapt to a particular light intensity by adjusting chlorophyll content and pigment composition, which will largely affect the photosynthetic rate. Also, temperature effect should be integrated into the growth rate model, an aspect that is particularly relevant for outdoor cultivation where large temperature variations occur frequently. What's more, mass limitations of critical nutrients such as nitrogen impact algal growth rate should also be considered.

Fifth, the method for coupling multidisciplinary and multiscale coupling is still insufficient. The Lagrangian approach is commonly used by tracking the algae cell trajectory. While only thousands of particles are simulated due to high computational cost, which is not enough to reach a statistically reliable results. Gao et al. (2016c) proposed an Eulerian approach model, which can couple the algae growth rate model with the CFD model directly and requires less computational resources. While this method is only applied in the Taylor-Couette reactor at present. Thus, the Eulerian approach model should be used to study and optimized more general types of algae PBR, like flat panel reactor, airlift reactor.

## NOTATION

$C_D$  = drag coefficient, dimensionless

$d_b$  = Sauter mean diameter of bubble, m

$d_s$  = diameter of algae cell, m

$F$  = inter-phase forces,  $\text{kg m}^{-2} \text{s}^{-2}$

$g$  = gravitational acceleration,  $\text{m s}^{-2}$

$L$  = cylinder height, m

$p$  = pressure, Pa

$r$  = cylinder radius, m

$u$  = velocity,  $\text{m s}^{-1}$

$x_1$  = mass fraction of resting state, dimensionless

$x_2$  = mass fraction of active state, dimensionless

$x_3$  = mass fraction of inhibitive state, dimensionless

**Greek letters**

$\alpha$  = volume fraction

$\varepsilon$  = turbulent dissipation rate,  $\text{m}^2 \text{s}^{-3}$

$\mu_t$  = turbulent viscosity, Pa s

$\rho$  = density,  $\text{kg m}^{-3}$

$\tau$  = phase stress tensor,  $\text{N m}^{-2}$

$\overline{\tau}^{\text{Re}}$  = phase Reynolds stress tensor,  $\text{N m}^{-2}$

**Subscripts**

b = bubble

l = liquid

g = gas

p = particle

## REFERENCES

- Acién Fernández FG, García Camacho F, Sánchez Pérez JA, Fernández Sevilla JM, Molina Grima E. 1998. Modeling of biomass productivity in tubular photobioreactors for microalgal cultures: effects of dilution rate, tube diameter, and solar irradiance. *Biotechnol Bioeng* 58(6):605–16.
- Acién Fernández FG, García Camacho F, Sánchez Pérez JA, Fernández Sevilla JM, Molina Grima E. 1997. A model for light distribution and average solar irradiance inside outdoor tubular photobioreactors for microalgal mass culture. *Biotechnol Bioeng* 55: 701–704.
- Alves SS, Vasconcelos JM, Orvalho SP. 2006. Mass transfer to clean bubbles at low turbulent energy dissipation. *Chem Eng Sci* 61 (4): 1334–1337.
- Andereck CD, Liu S, Swinney HL. 1986. Flow regimes in a circular Couette system with independently rotating cylinders. *J Fluid Mech* 164: 155–183.
- Antal SP, Lahey RT, Flaherty JE. 1991. Analysis of phase distribution in fully developed laminar bubbly two-phase flow. *Int J Multiphase Flow* 17: 635–652.
- Atkhen K, Fontaine J, Wesfreid JE. 2000. Highly turbulent Couette-Taylor bubbly flow patterns. *J Fluid Mech* 422: 55-68.
- Baier G, Graham MD, Lightfoot EN. 2000. Mass transport in a novel two-fluid vortex extractor. *AIChE J* 46: 2395–2407.
- Baier G, Graham MD. 2000. Two-fluid Taylor–Couette flow: experiments and linear theory for immiscible liquids between corotating cylinders with countercurrent axial flow. *Phys Fluids* 12: 294–303.
- Baier G, Graham MD. 2000. Two-fluid Taylor–Couette flow: experiments and linear theory for immiscible liquids between corotating cylinders. *Phys Fluids* 10: 3045–3055.
- Baier G, Grateful TM, Graham MD, Lightfoot EN. 1999. Prediction of mass transfer in spatially periodic systems. *Chem Eng Sci* 54: 343–356.
- Bari GS, Suess TN, Anderson GA, Gent SP. 2014. Predicting hydrodynamic and heat transfer effects of sparger geometry and placement within a column photobioreactor using computational fluid dynamics. *J Fuel Cell Sci Technol* 11: 031010-1.
- Bari GS, Suess TN, Anderson GA, Gent SP. 2015. Hydrodynamic and heat transfer effects of varying sparger spacing within a column photobioreactor using computational fluid dynamics. *J Fuel Cell Sci Technol* 12(1): 011004.
- Béchet Q, Shilton A, Guieysse B. 2013. Modeling the effects of light and temperature on algae growth: state of the art and critical assessment for productivity prediction during outdoor cultivation. *Biotechnol Adv* 31: 1648–1663.
- Behzadi A, Issa R, Rusche H. 2004. Modelling of dispersed bubble and droplet flow at high phase fractions. *Chem Eng Sci* 59 (4): 759–770.

- Benson BC, Rusch KA. 2006. Investigation of the light dynamics and their impact on algal growth rate in a hydraulically integrated serial turbidostat algal reactor (HISTAR). *Aquacult Eng* 35:122–134.
- Berberoglu H, Yin J, Pilon L. 2007. Light transfer in bubble sparged photobioreactors for H<sub>2</sub> production and CO<sub>2</sub> mitigation. *Int J Hydrog Energy* 32: 2273–2285.
- Bernardi A, Perin G, Sforza E, Galvanin F, Morosinotto T, Bezzo F. 2014. An identifiable state model to describe light intensity influence on microalgae growth. *Ind Eng Chem Res* 53: 6738–6749.
- Bernstein GJ, Grosvenor DE, Lenc JF, Levitz NM. 1973. A high-capacity annular centrifugal contactor. *Nucl Technol* 20: 200-202.
- Bitog JP, Lee IB, Kim KS, Hwang HS, Hong SW, Seo IH, Kwon KS, Mostafa E. 2011. Application of computational fluid dynamics for modeling and designing photobioreactors for microalgae production; a review. *Comput Electron Agric* 76:131–147
- Bitog JP, Lee IB, Oh HM, Hong SW, Seo IH, Kwon KS. 2014. Optimised hydrodynamic parameters for the design of photobioreactors using computational fluid dynamics and experimental validation. *Biosyst Eng* 122: 42–61.
- Bosma R, van Zessen E, Reith JH, Tramper J, Wijffels RH. 2007. Prediction of volumetric productivity of an outdoor photobioreactor. *Biotechnol Bioeng* 97(5):1108–1120.
- Buffo A, Marchisio DL. 2014. Modeling and simulation of turbulent polydisperse gas–liquid systems via the generalized population balance equation, *Rev Chem Eng* 30 (1): 73–126.
- Burin MJ, Schartman E, Ji, H. 2010. Local measurements of turbulent angular momentum transport in circular Couette flow. *Exp Fluids* 48: 763–769.
- Camacho Rubio F, Garcia Camacho F, Fernandez Sevilla, JM, Christi Y, Molina Grima E. 2003. A mechanistic model of photosynthesis in microalgae. *Biotechnol Bioeng* 81, 459–473.
- Campero RJ, Vigil RD. 1997. Axial dispersion during low Reynolds number Taylor–Couette flow: intra-vortex mixing effects. *Chem Eng Sci* 52: 3303–3310.
- Campero RJ, Vigil RD. 1999. Flow patterns in liquid–liquid Taylor–Couette–Poiseuille flow. *Ind Eng Chem Res* 38: 1094–1098.
- Carvalho M G, Farias T, Fontes P. 1991. Predicting Radiative Heat Transfer in Absorbing, Emitting, and Scattering Media Using the Discrete Transfer Method. In Fiveland WA et al., editor *Fundamentals of Radiation Heat Transfer*. 160. ASME HTD. 17–26.
- Ceccio SL. 2010. Friction drag reduction of external flows with bubble and gas injection. *Annu Rev Fluid Mech* 42: 183-203.
- Chen Z, Jiang Z, Zhang X, Zhang J. 2016. Numerical and experimental study on the CO<sub>2</sub> gas–liquid mass transfer in flat-plate airlift photobioreactor with different baffles. *Biochem Eng J* 106(15):129–138
- Cheng P. 1964. Two-Dimensional Radiating Gas Flow by a Moment Method. *AIAA J* 2: 1662–1664.
- Cheng W, Huang J, Chen J. 2016. Computational fluid dynamics simulation of mixing characteristics and light regime in tubular photobioreactors with novel static mixers. *J Chem Technol Biotechnol* 91: 327-335.

- Chisti MY. 1989. *Airlift Bioreactors*. Elsevier Applied Science, London.
- Chouippe A, Climent E, Legendre D, Gabillet C. 2014. Numerical simulation of bubble dispersion in turbulent Taylor–Couette flow. *Phys Fluids* 26 (4): 043304.
- Chui EH, Raithby GD. 1993. Computation of Radiant Heat Transfer on a Non-Orthogonal Mesh Using the Finite-Volume Method. *Numerical Heat Transfer, Part B*. 23: 269–288.
- Climent E, Simonnet M, Magnaudet J. 2007. Preferential accumulation of bubbles in Couette–Taylor flow patterns. *Phys Fluids* 19: 083301.
- Cockx A, Do-Quang Z, Audic J, Line A, Roustan M. 2001. Global and local mass transfer coefficients in waste water treatment process by computational fluid dynamics. *Chem Eng Process* 40 (2): 187–194.
- Coles D. 1965. Transition in circular Couette flow *J Fluid Mech* 21 (03): 385–425.
- Colombet D, Legendre D, Cockx A, Guiraud P, Risso F, Daniel C, Galinat S. 2011. Experimental study of mass transfer in a dense bubble swarm. *Chem Eng Sci* 66 (14): 3432–3440.
- Cornet JF, Dussap CG, Gros JB. 1994. Conversion of radiant light energy in photobioreactors. *AIChE J* 40(6):1055–1066.
- Cornet JF, Dussap CG, Gros JB. 1995. A simplified monodimensional approach formodeling coupling between radiant light transfer and growth kinetics in photobioreactors. *Chem Eng Sci* 50(9):1489–1500.
- Cornet JF, Dussap CG, Gros JB. 1998. Kinetics and energetics of photosynthetic micro-organisms in photobioreactors: Application to *Spirulina* growth. *Adv Biochem Eng/Biotechnol* 59:155–224.
- Csogör Z, Herrenbauer M, Schmidt K, Posten C. 2001. Light distribution in a novel photobioreactor-modelling for optimization. *J Appl Phycol* 13: 325–333.
- Dauta A, Devaux J, Piquemal F, Boumnic L. 1990. Growth rate of four freshwater algae in relation to light and temperature. *Hydrobiologia* 207:221–226.
- Deckwer WD, Burckhart R, Zoll G. 1974. Mixing and mass transfer in tall bubble columns. *Chem Eng Sci* 29 (11): 2177–2188.
- Degen J, Uebele A, Retze A, Schmid-Staiger U, Trosch W. 2001. A novel airlift photobioreactor with baffles for improved light utilization through the flashing light effect. *J Biotechnol* 92: 89–94.
- Delafosse A, Calvo S, Collignon ML, Delvigne F, Crine M, Thonart P, Toye D. 2014. CFD-based compartment model for description of mixing in bioreactors. *Chem Eng Sci* 106: 76–85.
- Djeridi H, Fave JF, Billard JY, Fruman DH. 1999. Bubble capture and migration in Couette–Taylor flow. *Exp Fluids* 26: 233–239.
- Djéridi H, Gabillet C, Billard JY. 2004. Two-phase Couette-Taylor flow: Arrangement of the dispersed phase and effects on the flow structures. *Phys Fluids* 16: 128-139.
- Dłuska E, Wronski S, Hubacz R. 2001. Mass transfer in gas–liquid Couette–Taylor flow reactor. *Chem Eng Sci* 56 (3): 1131–1136.
- Dłuska E, Wronski S, Ryszczyk T. 2004. Interfacial area in gas–liquid Couette–Taylor flow reactor. *Exp Therm Fluid Sci* 28 (5): 467–472.
- Doran PM. 1993. *Design of reactors for plant cells and organs*. Springer-Verlag, Berlin.

- Drew DA, Lahey RT. (Eds.). 1993. *Particulate Two-phase Flow*, Butterworth-Heinemann, Boston, MA, 509–566.
- Duran JE, Taghipour F, Mohseni M. 2010. Irradiance modeling in annular photoreactors using the finite-volume method. *J Photochem Photobiol A: Chem* 215 (1), 81–89.
- Eilers PHC, Peeters JCH. 1988. A model for the relationship between light intensity and the rate of photosynthesis in phytoplankton. *Ecol Model.* 42: 199–215.
- Eilers PHC, Peeters JCH. 1993. Dynamic behavior of a model for photosynthesis and photoinhibition. *Ecol Model*, 69: 113–133.
- Fluent, Theory Guide, 2011. ANSYS FLUENT 12.
- Fokoua G, Gabillet C, Colin C. 2013. Experimental study of bubble-drag interaction in a Taylor–Couette flow, in: 8th International Conference on Multiphase Flow ICMF, Jeju Island, Korea.
- Gao X, Kong B, Ramezani M, Olsen MG, Vigil RD. 2015a. An adaptive model for gas-liquid mass transfer in a Taylor vortex reactor. *Int J Heat Mass Transfer* 91: 433-446.
- Gao X, Kong B, Vigil RD. 2015b. CFD investigation of bubble effects on Taylor-Couette flow patterns in the weakly turbulent vortex regime. *Chem Eng J* 270: 508-518.
- Gao X, Kong B, Vigil RD. 2015c. Characteristic time scales of mixing, mass transfer and biomass growth in a Taylor vortex algal photobioreactor. *Bioresour Technol* 198: 283-291.
- Gao X, Kong B, Vigil RD. 2016a. CFD investigation of bubbly turbulent Taylor-Couette flow. *Chin J Chem Eng.* 24, 719-727.
- Gao X, Kong B, Vigil RD. 2016b. Comprehensive computational model for combining fluid hydrodynamics, light transport and algae growth in a Taylor vortex reactor: Lagrangian approach. Submitted to *Bioresour Technol*.
- Gao X, Kong B, Vigil RD. 2016c. Comprehensive computational model for combining fluid hydrodynamics, light transport and algae growth in a Taylor vortex reactor: Eulerian approach. Submitted to *Algal Research*.
- Gao X, Wang LJ, Wu C, Cheng YW, Li X. 2013. Novel bubble–emulsion hydrodynamic model for gas–solid bubbling fluidized beds. *Ind Eng Chem Res* 52 (31): 10835–10844.
- Garcia-Ochoa F, Gomez E. 1998. Mass transfer coefficient in stirred tank reactors for xanthan gum solutions. *Biochem Eng J* 1 (1): 1–10.
- Garcia-Camacho F, Sanchez-Miron A, Molina-Grima E, Camacho-Rubio F, Merchuck J. 2012. A mechanistic model of photosynthesis in microalgae including photoacclimation dynamics. *J Theor Biol* 304: 1–15.
- Garcia-Ochoa F, Gomez E. 2004. Theoretical prediction of gas–liquid mass transfer coefficient, specific area and hold-up in sparged stirred tanks. *Chem Eng Sci* 59 (12): 2489–2501.
- Garcia-Ochoa F, Gomez E. 2005. Prediction of gas-liquid mass transfer coefficient in sparged stirred tank bioreactors. *Biotechnol Bioeng* 92 (6): 761–772.
- Garcia-Ochoa F, Gomez E. 2009. Bioreactor scale-up and oxygen transfer rate in microbial processes: an overview. *Biotechnol Adv* 27: 153–176.

- Gavrilescu M, Roman RV. 1996. Mixing times in an external-loop airlift bioreactor with static mixers. *Acta Biotechnol* 16: 145–153.
- Gerdes C, Suess T, Anderson G, Gent S. 2014. Investigation of Hydrodynamics and Heat Transfer Effects due to Light Guides in a Column Photobioreactor. *J Fuel Cell Sci Technol* 11: 041002.
- Gómez-Pérez CA, Espinosa J, Montenegro Ruiz LC, van Boxtela AJB. 2015. CFD simulation for reduced energy costs in tubular photobioreactors using wall turbulence promoters. *Algal Res* 12: 1–9.
- Gosman A D, Ioannides E. 1983. Aspects of computer simulation of liquid-fuelled combustors. *J Energy* 7 (6): 482–490.
- Gourich B, Vial C, El Azher N, Souلامي MB, Ziyad M. 2006. Improvement of oxygen mass transfer estimation from oxygen concentration measurements in bubble column reactors. *Chem Eng Sci* 61 (18): 6218–6222.
- Griffith R. 1960. Mass transfer from drops and bubbles. *Chem Eng Sci* 12 (3): 198–213.
- Grobbelaar JU. 1990. Modeling algal productivity in large outdoor cultures and waste treatment systems. *Biomass* 21: 297–314.
- Grobbelaar JU. 1994. Turbulence in mass algal cultures and the role of light-dark fluctuations. *J Appl Phycol*. 6: 331–335.
- Han BP, Virtanen M, Koponen J, Straškraba M. 2000. Effect of photoinhibition on algal photosynthesis: a dynamic model. *J Plankton Res* 22(5):865–85.
- Han BP. 2002. A mechanistic model of algal photoinhibition induced by photodamage to Photosystem-II. *J Theor Biol* 214:519–27.
- Han P, Bartels DM. 1996. Temperature dependence of oxygen diffusion in H<sub>2</sub>O and D<sub>2</sub>O. *J Phys Chem* 100: 5597–5602.
- Han, BP. 2001. Photosynthesis-irradiance response at physiological level: A mechanistic model. *J Theor Biol* 148: 121–127.
- Haut B, Amor HB, Coulon L, Jacquet A, Halloin V. 2003. Hydrodynamics and mass transfer in a Couette–Taylor bioreactor for the culture of animal cells. *Chem Eng Sci* 58 (3): 777–784.
- Higbie R. 1935. The rate of absorption of a pure gas into still liquid during short periods of exposure, *Trans Am Inst Chem Eng* 31: 365.
- Hreiz R, Sialve B, Morchain J, Escudié R, Steyer JP, Guiraud P. 2014. Experimental and numerical investigation of hydrodynamics in raceway reactors used for algaculture. *Chem Eng J* 250: 230–239.
- Hu Q, Richmond A. 1996. Productivity and photosynthetic efficiency of *Spirulina platensis* as affected by light intensity, algal density and rate of mixing in a flat plate photobioreactor. *J Appl Phycol* 8: 139–145.
- Huang J, Feng F, Wan M, Ying J, Li Y, Qu X, Pan H, Shen G, Li W. 2015b. Improving performance of flat-plate photobioreactors by installation of novel internal mixers optimized with computational fluid dynamics. *Bioresour Technol* 182: 151–159.

- Huang J, Kang S, Wan M, Li Y, Qu X, Feng F, Wang J, Wang W, Shen G, Li W. 2015a. Numerical and experimental study on the performance of flat-plate photobioreactors with different inner structures for microalgae cultivation. *J Appl Phycol* 27:49–58.
- Huang J, Li Y, Wan M, Yan Y, Feng F, Qu X, Wang J, Shen G, Li W, Fan J Wang W. 2014. Novel flat-plate photobioreactors for microalgae cultivation with special mixers to promote mixing along the light gradient. *Bioresour Technol* 159: 8–16.
- Huang J, Qu X, Wan M, Ying J, Li Y, Zhu F, Wang J, Shen G, Chen J, Li W. 2015c. Investigation on the performance of raceway ponds with internal structures by the means of CFD simulations and experiments. *Algal Research* 10: 64–71.
- Huang Q, Liu T, Yang J, Yao L, Gao L. 2011. Evaluation of radiative transfer using the finite volume method in cylindrical photoreactors. *Chem Eng Sci* 66 (17): 3930–3940.
- Huang Q, Yang C, Yu G, Mao ZS. 2010. CFD simulation of hydrodynamics and mass transfer in an internal airlift loop reactor using a steady two-fluid model. *Chem Eng Sci* 65(20): 5527-5536.
- Janssen M, de Bresser L, Baijens T, Tramper J, Mur LR, Snel JFH, Wijffels RH. 2000. Scale-up aspects of photobioreactors: Effects of mixing-induced light/dark cycles. *J Appl Phycol* 12:225–237.
- Janssen M, Tramper J, Mur LR, Wijffels RH. 2003. Enclosed outdoor photobioreactors: Light regime, photosynthetic efficiency, scale-up, and future prospects. *Biotechnol Bioeng* 81: 193–210.
- Janssen M. 2016. *Microalgal Photosynthesis and Growth in Mass Culture*. Advances in Chemical Engineering, Academic Press.
- Jeon YC, Cho CW, Yun YS. 2005. Measurement of microalgal photosynthetic activity depending on light intensity and quality. *Biochem Eng J* 27:127–31.
- Joseph D, Nguyen K, Beavers G. 1984. Non-uniqueness and stability of the configuration of flow of immiscible fluids with different viscosities. *J Fluid Mech* 141: 319–345.
- Joseph DD, Preziosi L. 1987. Stability of rigid motions and coating films in bicomponent flows of immiscible liquids. *J Fluid Mech* 185: 323-329.
- Joseph DD, Singh P, Chen K. 1990. Couette Flows, Rollers, Emulsions, Tall Taylor Cells, Phase Separation and Inversion, and a Chaotic Bubble in Taylor-Couette Flow of Two Immiscible Liquids, Nonlinear Evolution of Spatio-Temporal Structures in Dissipative Continuous Systems, NATO ASI Series, 225: 169-189.
- Kadam B, Joshi J, Koganti S, Patil R. 2008. Hydrodynamic and mass transfer characteristics of annular centrifugal extractors. *Chem Eng Res Des* 86 (3): 233–244.
- Kawase Y, Halard B, Moo-Young M. 1987. Theoretical prediction of volumetric mass transfer coefficients in bubble columns for Newtonian and non-Newtonian fluids. *Chem Eng Sci* 42 (7): 1609-1617.
- Kawase Y, Hashiguchi N. 1996. Gas-liquid mass transfer in external-loop airlift columns with newtonian and non-newtonian fluids, *Chem Eng J Biochem Eng J* 62 (1): 35-42.
- Kliphuis AM, de Winter L, Vejrazka C, Martens DE, Janssen M, Wijffels RH. 2010. Photosynthetic efficiency of *Chlorella sorokiniana* in a turbulently mixed short light-path photobioreactor. *Biotechnol Prog* 26 (3): 687–696.

- Kong B, Shanks JV, Vigil RD. 2013. Enhanced algal growth rate in a Taylor vortex reactor. *Biotechnol Bioeng* 110 (8): 2140–2149.
- Kong B, Vigil RD. 2013. Light-limited continuous culture of *Chlorella vulgaris* in a Taylor vortex reactor. *Environ Prog Sustainable Energy* 32 (4): 884–890.
- Kong B, Vigil RD. 2014. Simulation of photosynthetically active radiation distribution in algal photobioreactors using a multidimensional spectral radiation model. *Bioresour Technol* 158:141–148.
- Kraakman NJR, Rocha-Rios J, van Loosdrecht MCM. 2011. Review of mass transfer aspects for biological gas treatment. *Appl. Microbiol Biotechnol* 91: 873–886.
- Krishnamoorthy G, Klosterman R, Shallbetter D. 2014. A Radiative Transfer Modeling Methodology in Gas-Liquid Multiphase Flow Simulations. *J Eng* 2314-4904.
- Kroon BMA, Thoms S. 2006. From electron to biomass: a mechanistic model to describe phytoplankton photosynthesis and steady-state growth rates. *J Phycol* 42: 593–609.
- Krujatz F, Illing R, Krautwer T, Liao J, Helbig K, Goy K, Opitz J, Cuniberti G, Bley T, Weber J. 2015. Light-field-characterization in a continuous hydrogen-producing photobioreactor by optical simulation and computational fluid dynamics. *Biotech Bioeng* 112: 2439-2449.
- Kumar K, Das D. 2012. Growth characteristics of *Chlorella sorokiniana* in airlift and bubble column photobioreactors. *Bioresour Technol* 116: 307–313.
- Lamont JC, Scott D. 1970. An eddy cell model of mass transfer into the surface of a turbulent liquid. *AIChE J* 16 (4): 513–519.
- Lee HY, Erickson LE, Yang SS. 1987. Kinetics and bioenergetics of light-limited photoautotrophic growth of *Spirulina platensis*. *Biotechnol Bioeng* 29:832–43.
- Li Q, Zhao X, Cheng K, Du W, Liu D. 2013. Simulation and experimentation on the gas holdup characteristics of a novel oscillating airlift loop reactor. *J Chem Technol Biotechnol* 88: 704–710.
- Liao Q, Li L, Chen R, Zhu X. 2014. A novel photobioreactor generating the light/dark cycle to improve microalgae cultivation. *Bioresour Technol* 161: 186–191.
- Lilly GP. 1973. Effect of particle size on particle eddy diffusivity. *Ind Eng Chem Fundam* 12(3):26-275.
- Linek V, Kordač M, Fujasová M, Moucha T. 2004. Gas–liquid mass transfer coefficient in stirred tanks interpreted through models of idealized eddy structure of turbulence in the bubble vicinity. *Chem Eng and Proc: Proc Intensif* 43:1511–1517.
- Lochiel A, Calderbank P. 1964. Mass transfer in the continuous phase around axisymmetric bodies of revolution. *Chem Eng Sci* 19 (7): 471–484.
- Luo HP, Al-Dahhan MH. 2004. Analyzing and modeling of photobioreactors by combining first principles of physiology and hydrodynamics. *Biot and Bioeng* 85(4): 382–393.
- Luo HP, Al-Dahhan MH. 2011. CFD simulations for local flow dynamics in a draft tube airlift bioreactor. *Chem Eng Sci* 66(5):907–923.
- Luo HP, Al-Dahhan MH. 2012. Airlift column photobioreactors for *Porphyridium* sp. culturing: Part II. Verification of dynamic growth rate model for reactor performance evaluation. *Biotechnol Bioeng* 109(4): 942–949.

- Markl H, Mather M. 1985. Mixing and aeration of shallow open ponds. *Arch. Hydrobiol Beih* 20: 85–93.
- Marshall HL, Geider RJ, Flynn KJ. 2000. A mechanistic model of photoinhibition. *New Phytol* 145: 347–359.
- Marshall JS, Huang Y. 2010. Simulation of light-limited algae growth in homogeneous turbulence. *Chem Eng Sci* 65:3865–3875.
- Marshall JS, Sala K. 2011. A stochastic lagrangian approach for simulating the effect of turbulent mixing on algae growth rate in a photobioreactor. *Chem Eng Sci* 66: 384–392.
- Maryami R, Farahat S, Javad poor M, Shafiei Mayam MH. 2014. Bubbly drag reduction in a vertical Couette–Taylor system with superimposed axial flow. *Fluid Dyn Res* 46: 055504.
- Massart A, Mirisola A, Lupant D. 2014. Experimental characterization and numerical simulation of the hydrodynamics in an airlift photobioreactor for microalgae culture. *Algal Res* 6: 210–217.
- Mehel A, Gabillet C, Djeridi H. 2006. Bubble effect on the structures of weakly turbulent Couette–Taylor flow. *J Fluids Eng* 128: 819–831.
- Mehel A, Gabillet C, Djeridi H. 2007. Analysis of the flow pattern modifications in a bubbly Couette–Taylor flow. *Phys Fluids* 19: 118101.
- Meng C, Huang J, Ye C. 2015. Comparing the performances of circular ponds with different impellers by CFD simulation and microalgae culture experiments. *Bioprocess Biosyst Eng* 38:1347–1363
- Merchuk JC, Garcia-Garcia Camacho F, Molina-Grima E. 2007. Photobioreactor design and fluid dynamics. *Chem Biochem Eng Q* 21(4): 345–355.
- Merchuk JC, Ronen M, Giris S, Arad S, 1998. Light/dark cycles in the growth of the red microalga *Porphyridium Sp.* *Biotechnol Bioeng* 59: 705–713.
- Miller R, Tsuchiya H, Fredrickson A, Brown A. 1964. Hydromechanical method to increase efficiency of algal photosynthesis. *Ind Eng Chem Process Des* 3: 134–143.
- Miron AS, Garcia M-CC, Camacho FG, Grima EM, Chisti Y. 2002. Growth and biochemical characterization of microalgal biomass produced in bubble column and airlift photobioreactors: studies in fed-batch culture. *Enzyme Microb Technol* 31: 1015–1023.
- Mirón AS, Gómez AC, Camacho FG, Grima EM, Chisti Y. 1999. Comparative evaluation of compact photobioreactors for large-scale monoculture of microalgae. *J Biotechnol* 70: 249–270
- Moberg AK, Ellem GK, Jameson GJ, Herbertson JG. 2012. Simulated cell trajectories in a stratified gas -liquid flow tubular photobioreactor. *J Appl Phycol* 24: 357–363.
- Monahan SM, Fox RO. 2007. Effect of model formulation on flow-regime predictions for bubble columns. *AICHE J* 53 (1): 9–18.
- Mortuza SM, Gent SP, Kommareddy A, Anderson GA. 2012. Investigation of bubble and fluid flow patterns within a column photobioreactor. *J Fuel Cell Sci Technol* 9: 031006.
- Morweiser M, Kruse O, Hankamer B, Posten C. 2010. Developments and perspectives of photobioreactors for biofuel production. *Appl Microbio Biotechnol* 87: 1291–1301.

- Muller-Feuga A, Le Guédes R, Pruvost J. 2003. Benefits and limitations of modeling for optimization of *Porphyridium cruentum* cultures in an annular photobioreactor. *J Biotech* 103:153–163.
- Murai Y, Oiwa H, Takeda Y. 2005. Bubble behavior in a vertical Taylor-Couette flow. *J Phys Conf Ser* 14: 143-156.
- Murai Y, Oiwa H, Takeda Y. 2008. Frictional drag reduction in bubbly Couette–Taylor flow. *Phys Fluids* 20: 034101.
- Muroyama K, Imai K, Oka Y, Hayashi J. 2013. Mass transfer properties in a bubble column associated with micro-bubble dispersions. *Chem Eng Sci* 100: 464–473.
- Nauha EK, Alopaeus V. 2013. Modeling method for combining fluid dynamics and algal growth in a bubble column photobioreactor. *Chem Eng J* 229:559–568.
- Nauha EK, Alopaeus V. 2015. Modeling outdoors algal cultivation with compartmental approach. *Chem Eng J* 259: 945–960.
- Nikolaou A, Bernardi A, Meneghesso A, Bezzo F, Morosinotto T, and Chachuat B. 2015. A model of chlorophyll fluorescence in microalgae integrating photoproduction, photoinhibition and photoregulation. *J Biotech*, 194:91-99.
- Nikolaou A, Hartmann P, Sciandra A, Chachuat B, Bernard O. 2016. Dynamic coupling of photoacclimation and photoinhibition in a model of microalgae growth. *J Theor Biol* 390: 61–72.
- Ogbonna JC, Yada H, Tanaka H. 1995. Light-supply coefficient: a new engineering parameter for photobioreactor design. *J Ferment Bioeng* 80(4):369–76.
- Olivieri G, Gargiulo L, Lettieri P, Mazzei L, Salatino P, Marzocchella. 2015. Photobioreactors for microalgal cultures: A lagrangian model coupling hydrodynamics and kinetics. *Biotechnol Progress* 31(5):1259-1272.
- Ozbek B, Gayik S. 2001. The studies on the oxygen mass transfer coefficient in a bioreactor, *Process Biochem* 36 (8): 729–741.
- Pahlow M, Oschlies A. 2009. Chain model of phytoplankton P, N and light colimitation. *Mar Ecol Prog Ser* 376: 69–83.
- Papáček Š, Štumbauer V, Štys D, Petera K, Matonoha C. 2011. Growth impact of hydrodynamic dispersion in a couette-taylor bioreactor. *Mathematical and Computer Modelling* 54:1791–1795.
- Papáček Š, Štys D, Dolínek P, Petera K. 2007. Multicompartmen/CFD modelling of transport and reaction processes in Couette–Taylor photobioreactor. *Appl Comp Mech* 1: 577–586.
- Papáček Š, Jablonský J, Petera K, Reháč B, Matonoha C. 2014. Modeling and Optimization of Microalgae Growth in Photobioreactors: A Multidisciplinary Problem. *ISCS 2014: Interdisciplinary Symposium on Complex Systems*, 277-286.
- Papadakis I, Kotzabasis K, Lika K. 2012. Modeling the dynamic modulation of the light energy in photosynthetic algae. *J Theor Biol* 300: 254–264.
- Park S, Li Y. 2015. Integration of Biological Kinetics and Computational Fluid Dynamics to Model the Growth of *Nannochloropsis salina* in an Open Channel Raceway. *Biotech Bioeng* 112: 923-933.
- Patankar SV. 1980. *Numerical Heat Transfer and Fluid Flow*, Hemisphere Publishing Corporation.

- Pottier L, Pruvost J, Deremetz J, Cornet JF, Legrand J, Dussap CG. 2005. A fully predictive model for one-dimensional light attenuation by *Chlamydomonas reinhardtii* in a torus reactor. *Biotechnol Bioeng* 91 (5): 569-582.
- Prussi M, Buffi M, Casini D, Chiamonti D, Martelli F, Carnevale M, R. Tredici M, Rodolfi L. 2014. Experimental and numerical investigations of mixing in raceway ponds for algae cultivation. *Biomass Bioenergy* 67: 390–400.
- Pruvost J, Cornet JF, Legrand J. 2008. Hydrodynamics influence on light conversion in photobioreactors: An energetically consistent analysis. *Chem Eng Sci* 63(14):3679–3694.
- Pruvost J, Legrand J, Legentilhomme P, Mueller-Fuega A. 2002a. Simulation of microalgae growth in limiting light conditions: flow effect. *AIChE J* 48:1109-1120.
- Pruvost J, Legrand J, Legentilhomme P, Mueller-Fuega A. 2002b. Lagrangian trajectory model for turbulent swirling flow in an annular cell: Comparison with residence time distribution measurements. *Chem Eng Sci* 57:1205-1215.
- Pruvost J, Legrand J, Legentilhomme P, Rosant JM. 2004. Numerical investigation of bend and torus flows. Part II. Flow simulation in torus reactor. *Chem Eng Sci* 59 (16): 3359–3370.
- Pruvost J, Pottier L, Legrand J. 2006. Numerical investigation of hydrodynamic and mixing conditions in a torus photobioreactor. *Chem Eng Sci* 61:4476–4489.
- Qiao J, Lew CMJ, Karthikeyan A, Wang CH. 2014. Production of pex protein from qm7 cells cultured in polymer scaffolds in a Taylor–Couette bioreactor *Biochem Eng J* 88: 179–187.
- Racina A, Liu Z, Kind M. 2010. Mixing in Taylor–Couette flow. In: Bockhorn H, Mewes D, Peukert W, Warnecke H-J. (Eds.), *Micro and Macro Mixing: Analysis, Simulation and Numerical Calculation*. Springer-Verlag, Berlin, pp.125–139.
- Ramezani M, Kong B, Gao X, Olsen MG, Vigil RD. 2015. Experimental measurement of oxygen mass transfer and bubble size distribution in an air water multiphase Taylor-Couette vortex bioreactor, *Chem Eng J* 279: 286- 296.
- Renardy Y, Joseph DD. 1985. Couette flow of two fluids between concentric cylinders. *J Fluid Mech* 150: 381–394.
- Richmond A. 2004. Principles for attaining maximal microalgal productivity in photobioreactors: an overview. *Hydrobiologia* 512: 33–37.
- Roghair I, Annaland MVS, Kuipers HJAM. 2013. Drag force and clustering in bubble swarms. *AIChE J* 59 (5): 1791–1800.
- Rorrer GL, Mullikin RK. 1999. Modeling and simulation of a tubular recycle photobioreactor for macroalgal cell suspension cultures. *Chem Eng Sci* 54:3153–3162.
- Ross O, Geider R. 2009. New cell based model of photosynthesis and photoacclimation: Accumulation and mobilisation of energy reserves in phytoplankton. *Mar Ecol: Prog Ser* 383: 53–71.
- Sander R. 2015. Compilation of Henry’s law constants (version 4.0) for water as solvent. *Atmos Chem Phys* 15: 4399–4981.
- Sathe MJ, Deshmukh SS, Joshi JB, Koganti SB. 2009. Computational fluid dynamics simulation and experimental investigation: study of two-phase liquid- liquid flow in a vertical Taylor–Couette contactor. *Ind Eng Chem Res* 49 (1): 14–28.

- Sato T, Yamada D, Hirabayashi S. 2010. Development of virtual photobioreactor for microalgae culture considering turbulent flow and flashing light effect. *Energ Convers Manage* 51:1196–1201.
- Sato Y, Sekoguchi K. 1975. Liquid velocity distribution in two-phase bubble flow. *Int J Multiphase Flow* 2 (1): 79–95.
- Schiller L, Naumann Z. 1935. A Drag Coefficient. Correlation. *Z Ver Deutsch Ing* 77:318.
- Shiomi Y, Kutruna H, Akagawa K, Ozawa M. 1993. Two-phase flow in an annulus with a rotating inner cylinder (flow pattern in bubbly flow region). *Nucl Eng Des* 141: 27–34.
- Shiomi Y, Nakanishi S, Kutsuna H. 2000. CFD calculation for two-phase flow in concentric annulus with rotating inner cylinder, PHOENICS Users Conference Proceedings, Phoenix.
- Siegel R, Howell JR. 1992. *Thermal Radiation Heat Transfer*. Hemisphere Publishing Corporation, Washington DC.
- Simonnet M, Gentric C, Olmos E, Midoux N. 2007. Experimental determination of the drag coefficient in a swarm of bubbles. *Chem Eng Sci* 62 (3): 858–866.
- Smith JD, Neto AA, Cremaschi S, Crunkleton DW. 2013. CFD-based optimization of a flooded bed algae bioreactor. *Ind Eng Chem Res* 52: 7181–7188
- Sobczuk TM, Camacho FG, Grima EM, Chisti Y. 2006. Effects of agitation on the microalgae *Phaeodactylum tricornutum* and *Porphyridium cruentum*. *Bioprocess Biosyst Eng* 28(4): 243–250.
- Soman A, Shatri Y. 2015. Optimization of novel photobioreactor design using computational fluid dynamics. *Appl Energy* 140: 246–255.
- Sorg R, Tanzeglock T, Soos M, Morbidelli M, Perilleux A, Solacroup T, Broly H. 2011. Minimizing hydrodynamic stress in mammalian cell culture through the lobed Taylor–Couette bioreactor. *Biotechnol J* 6 (12): 1504–1515.
- Spolaore P, Joannis-Cassan C, Duran E, Isambert A. 2006. Commercial applications of microalgae. *J Biosci Bioeng* 101(2): 87–96.
- Su ZF, Kang RJ, Shi SY, Cong W, Cai ZL. 2010. Study on the destabilization mixing in the flat plate photobioreactor by means of CFD. *Biomass Bioenergy* 34:1879–1884.
- Sugiyama K, Calzavarini E, Lohse D. 2008. Microbubble drag reduction in Taylor– Couette flow in the wavy vortex regime. *J Fluid Mech* 608: 21–41.
- Suh IS, Lee SB. 2003. A light distribution model for an internally radiating photobioreactor. *Biotechnol Bioeng* 82(2):180–189.
- Tabib MV, Roy SA, Joshi JB. 2008. CFD Simulation of Bubble Column—An Analysis of Interphase Forces and Turbulence Models. *Chem Eng J* 139(3): 589–614.
- Takache H, Pruvost J, Marec H. 2015. Investigation of light/dark cycles effects on the photosynthetic growth of *Chlamydomonas reinhardtii* in conditions representative of photobioreactor cultivation. *Algal Res. Biomass Biofuels Bioprod.* 8: 192–204.
- Talvy S, Cockx A, Line A. 2007. Modeling hydrodynamics of gas–liquid airlift reactor. *AIChE J* 53: 335–353.

- Tamimi A, Rinker EB, Sandall OC. 1994. Diffusion coefficients for hydrogen sulfide, carbon dioxide, and nitrous-oxide in water over the temperature-range 293–368 K *J Chem Eng Data* 39: 330–332.
- Thomas WH, Gibson CH. 1990. Effects of small-scale turbulence on microalgae. *J Appl Phycol.* 2: 71–77.
- Tomiyama A, Kataoka I, Zun I, Sakaguchi T. 1998. Drag coefficients of single bubbles under normal and micro gravity conditions. *JSME Int J Ser B* 41 (2): 472–479.
- Ugwu CU, Ogbonna JC, Tanaka H. 2005. Light/dark cyclic movement of algal culture (*Synechocystis aquatilis*) in outdoor inclined tubular photobioreactor equipped with static mixers for efficient production of biomass. *Biotechnol Lett* 27: 75–78.
- van den Berg TH, Luther S, Lathrop DP, Lohse D. 2005. Drag reduction in bubbly Taylor-Couette turbulence. *Phys Rev Lett* 94: 044501.
- van den Berg TH, van Gils DPM, Lathrop DP, Lohse D. 2007. Bubbly turbulent drag reduction is a boundary layer effect. *Phys Rev Lett* 98: 084501.
- van Gils DP, Huisman SG, Bruggert GW, Sun C, Lohse D. 2011. Torque scaling in turbulent Taylor-Couette flow with co-and counterrotating cylinders. *Phys Rev Lett* 106 (2): 024502.
- van Gils DPM, Guzman DN, Sun C, Lohse D. 2013. The importance of bubble deformability for strong drag reduction in bubbly turbulent Taylor-Couette flow. *J Fluid Mech* 722: 317–347.
- Vedantam S, Joshi JB, Koganti SB. 2006. Three dimensional CFD simulation of stratified two-fluid Taylor–Couette flow. *Can J Chem Eng* 84: 279–288.
- Vedantam S, Joshi JB. 2006. Annular centrifugal extractors: a review. *Chem Eng Res Des* 84: 522–542.
- Wang L, Olsen MG, Vigil RD. 2005. Reappearance of azimuthal waves in turbulent Taylor–Couette flow at large aspect ratio. *Chem Eng Sci* 60 (20): 5555–5568.
- Wang L, Vigil RD, Fox RO. 2005. CFD simulation of shear-induced aggregation and breakage in turbulent Taylor–Couette flow. *J Colloid Inter Sci* 285: 167–178.
- Wang LL, Tao Y, Mao XZ. 2014. A novel flat plate algal bioreactor with horizontal baffles: structural optimization and cultivation performance. *Bioresour Technol* 164: 20–27.
- Wang T, Wang J. 2007. Numerical simulations of gas-liquid mass transfer in bubble columns with a CFD-PBM coupled model, *Chem Eng Sci* 62 (24): 7107–7118.
- Watamura Y, Takeda W, Murai Y. 2013. Intensified and attenuated waves in a microbubble Taylor–Couette flow. *Phys Fluids* 25: 054107.
- Wijffels RH, Barbosa MJ. 2010. An outlook on microalgal biofuels. *Science* 329:796–799.
- Wilcox DC. 1998. *Turbulence Modeling for CFD*. DCW Industries, Inc. La Canada, California.
- Wronski S, Dłuska E, Hubacz R, Molga E. 1999. Mass transfer in gas–liquid Couette–Taylor flow in membrane reactor. *Chem Eng Sci* 54 (13): 2963–2967.
- Wu LB, Li Z, Song YZ. 2009. Numerical Investigation of Flow Characteristics and Irradiance History in a Novel Photobioreactor. *Afr J Biotechnol* 8: 4672–4679.
- Wu X, Merchuck JC. 2001. A model integrating fluid dynamics in photosynthesis and photoinhibition processes. *Chem Eng Sci* 56: 3527–3538.

- Wu X, Merchuk JC. 2002. Simulation of algae growth in a bench scale bubble column. *Biotechnol Bioeng* 80: 156–168.
- Wu X, Merchuk JC. 2004. Simulation of algae growth in a bench-scale internal loop airlift reactor. *Chem Eng Sci* 59: 2912–2999.
- Xu L, Liu R, Wang F, Liu C. 2012. Development of a draft-tube airlift bioreactor for *Botryococcus braunii* with an optimized inner structure using computational fluid dynamics. *Bioresour Technol* 119: 300–305.
- Yeoh, GH., Tu, JY. 2010. *Computational Techniques for Multiphase Flows - Basics and Applications*. Butterworth-Heinemann, Elsevier Science and Technology.
- Yoshida K, Tasaka Y, Murai Y, Takeda Y. 2009. Mode transition in bubbly Taylor– Couette flow measured by PTV. *J Phys: Conf Ser* 147: 012013.
- Yun YS, Park JM. 2003. Kinetic modeling of the light-dependent photosynthetic activity of the green microalga *Chlorella vulgaris*. *Biotechnol Bioeng* 83(3):303–11.
- Zeng F, Huang J, Meng C, Zhu F, Chen J, Li Y. 2016. Investigation on novel raceway pond with inclined paddle wheels through simulation and microalgae culture experiments. *Bioprocess Biosyst Eng* 39:169–180.
- Zhang D, Dechatiwongse P, Hellgardt K. 2015. Modelling light transmission, cyanobacterial growth kinetics and fluid dynamics in a laboratory scale multiphase photo-bioreactor for biological hydrogen production. *Algal Res* 8(0): 99–107.
- Zhang D, Deen NG, Kuipers JAM. 2006. Numerical Simulation of the Dynamic Flow Behavior in a Bubble Column: A Study of Closures for Turbulence and Interface Forces. *Chem Eng Sci* 61(23): 7593–7608.
- Zhang QH, Wu X, Xue SZ, Wang ZH, Yan CH, Cong W. 2013. Hydrodynamic characteristics and microalgae cultivation in a novel flat-plate photobioreactor. *Biotechnol Prog* 29: 127–134.
- Zhang QH, Xue S, Yan C, Wu X, Wen S, Cong W. 2015. Installation of flow deflectors and wing baffles to reduce dead zone and enhance flashing light effect in an open raceway pond. *Bioresour Technol* 198: 150–156.
- Zhang T. 2013. Dynamics of fluid and light intensity in mechanically stirred photobioreactor. *J Biotechnol* 168:107–116.
- Zhu XH, Arifin DY, Khoo BH, Hua J, Wang CH. 2010. Study of cell seeding on porous poly (d, l-lactic-co-glycolic acid) sponge and growth in a Couette-Taylor bioreactor. *Chem Eng Sci* 65 (6): 2108–2117.
- Zhu XY, Campero RJ, Vigil RD. 2000. Axial mass transport in liquid-liquid Taylor-Couette-Poiseuille flow. *Chem Eng Sci* 55: 5078-5087.
- Zhu XY, Vigil RD. 2001. Banded liquid–liquid Taylor–Couette–Poiseuille flow. *AIChE J* 47 (9): 1932–1940.